Title

Variational Gaussian-Based Methods in Quantum Statistical Mechanics: Development and Applications to Molecules, Clusters, and Condensed Phase Systems

Permalink

https://escholarship.org/uc/item/7cx4k94k

Author

Brown, Sandra E.

Publication Date

2016

Peer reviewed|Thesis/dissertation

UNIVERSITY OF CALIFORNIA,
IRVINE

Variational Gaussian-Based Methods in Quantum Statistical Mechanics:
Development and Applications to Molecules, Clusters, and Condensed Phase
Systems

DISSERTATION

submitted in partial satisfaction of the requirements
for the degree of

DOCTOR OF PHILOSOPHY

in Chemistry

by

Sandra E. Brown

Dissertation Committee:
Professor Vladimir Mandelshtam, Chair
Professor Craig Martens
Professor Filipp Furche

2016

DEDICATION

Dedicated to my dad.

TABLE OF CONTENTS

LIST OF FIGURES

LIST OF TABLES

ACKNOWLEDGEMENTS

CURRICULUM VITAE

Sandra E. Brown

Education

Ph.D. in Chemistry, August 2016
University of California, Irvine
Advisor: Vladimir A. Mandelshtam

Theoretical chemistry; quantum statistical mechanics; method development with applications to vibrational spectroscopy and free energy calculations of molecules, liquids, and clusters.

Bachelor of Science in Applied Mathematics and Biochemistry, June 2010
University of California, Los Angeles
Departmental Honors, Department of Chemistry and Biochemistry

Research Experience

Graduate Student Researcher, July 2011 - August 2016
Department of Chemistry, University of California, Irvine
Principal Investigator: Vladimir A. Mandelshtam, mandelsh@uci.edu

Method development and implementation for computing thermodynamic properties of quantum mechanical systems; evaluation of the efficiency and robustness of theoretical models by conducting numerical tests and applying them to systems of interest; applications to quantum liquids and clusters

Undergraduate Researcher, June 2008 - October 2009
Department of Chemistry and Biochemistry, University of California, Los Angeles
Principal Investigator: Christina A. Bauer, cbauer@whittier.edu

Synthesized highly fluorescent silica nanoparticles by polyamine catalysis; characterized particles and determined effects of various experimental parameters on particle size, shape, dispersity, porosity, and fluorescence properties using various experimental techniques, including UV-Vis spectroscopy, fluorescence spectroscopy, thermogravimetric analysis, nitrogen adsorption/desorption analysis, and electron microscopy

Publications

SEB and Vladimir A. Mandelshtam. Self-consistent phonons: An accurate and practical method to account for anharmonic effects in equilibrium properties of general classical or quantum many-body systems. *Chemical Physics*, 2016. Available online: http://dx.doi.org/10.1016/j.chemphys.2016.06.008.

Joel D. Mallory, **SEB**, and Vladimir A. Mandelshtam. Assessing the Performance of the Diffusion Monte Carlo Method As Applied to the Water Monomer, Dimer, and Hexamer. *The Journal of Physical Chemistry A*, 119(24):65046515, 2015

SEB, Ionuţ Georgescu, and Vladimir A. Mandelshtam. Self-consistent phonons revisited. II. A general and efficient method for computing free energies and vibrational spectra of molecules and clusters. *The Journal of Chemical Physics*, 138(4):044317, 2013

Ionuţ Georgescu, **SEB**, and Vladimir A. Mandelshtam. Mapping the phase diagram for neon to a quantum Lennard-Jones fluid using Gibbs ensemble simulations. *The Journal of Chemical Physics*, 138(13):134502, 2013

Presentations

SEB "Self-consistent phonons: An efficient approach for computing thermodynamic and dynamic properties of general classical or quantum many-body systems." Poster presentation, Southern California Theoretical Chemistry Symposium; La Jolla, CA, June 2016.

SEB "Self-consistent phonons with quasi-Monte Carlo: An efficient approach for computing thermodynamic and dynamic properties of high-dimensional systems." Oral presentation, Pacifichem 2015, Honolulu, Hawaii, December 2015.

SEB "Self-consistent phonons made practical: Going beyond the harmonic approximation with quasi-Monte Carlo." Oral presentation, University of California, Irvine Molecular Dynamics Seminar; Irvine, CA, March 2015.

SEB, Ionuţ Georgescu, Vladimir A. Mandelshtam. "Gibbs ensemble simulation of liquid-vapor equilibrium in quantum neon." Poster presentation, Quantum Molecular Dynamics: A Conference in Honor of William H. Miller, Berkeley, California, January

10, 2012.

SEB, Christina A. Bauer, Sarah H. Tolbert. "Synthesis of Highly Fluorescent Silica Nanoparticles by Polyamine Catalysis." Poster presentation, University of California, Los Angeles Twelfth Annual Science Poster Day, Los Angeles, CA, May 2009.

Teaching

Course Instructor at University of California, Irvine, Fall Quarter 2015
  ⋄ Chemistry 1A: General Chemistry

Teaching Assistant at University of California, Irvine, September 2011 - June 2016
  ⋄ Chemistry H2A, 1B, 1C: General Chemistry
  ⋄ Chemistry 231A: Fundamentals of Quantum Mechanics
  ⋄ Chemistry 231B: Applications of Quantum Mechanics
  ⋄ Chemistry 232B: Advanced Topics in Statistical Mechanics
  ⋄ Chemistry 237: Mathematical Methods in Chemistry
  ⋄ Chemistry 248: Electrochemistry

Awards

  ⋄ UCI Department of Chemistry Michael Zach Award for "Most Promising Future Faculty", June 2016.
  ⋄ UCI Regents' Dissertation Fellowship, Winter 2016.

Workshops

Telluride School on Theoretical Chemistry, Telluride Science Research Center. Telluride, CO, July 2013.

Computer Skills

Fortran, C/C++, Unix, MATLAB, Mathematica

Languages

English, Spanish

ABSTRACT OF THE DISSERTATION

Variational Gaussian-Based Methods in Quantum Statistical Mechanics:

Development and Applications to Molecules, Clusters, and Condensed Phase

Systems

by

Sandra E. Brown

Doctor of Philosophy in Chemistry

University of California at Irvine, 2016

Professor Vladimir Mandelshtam, Chair

The projects comprising my thesis lie in the area of quantum statistical mechanics, and are in line with the Mandelshtam group's broad goals of developing new approaches for computing thermodynamic and dynamic properties of classical and quantum many-body systems, improving existing methods, and demonstrating their utility and efficiency on systems of chemical interest. My research has been particularly involved with the implementation and ongoing development of variational approaches which exploit the tractability of Gaussian functions and their well-known properties. In this thesis I describe what I believe to be my most important research accomplishments.

In my first project, I combined the variational Gaussian wavepacket (VGW) approximation with Gibbs ensemble Monte Carlo to compute the equation of state for a quantum Lennard-Jones liquid as a function of temperature and quantum-character, providing data which enables one to describe a large variety of real liquids that could

be mapped to a Lennard-Jones model. After performing Lennard-Jones parameter optimization for neon, the results were found to be in excellent agreement with experimental data. With this work we demonstrated the efficiency of VGW, and highlighted its advantages over path integral-based approaches.

My subsequent projects have been based on the implementation, ongoing development, and evaluation of the self-consistent phonons (SCP) method. Based on the Gibbs-Bogoliubov inequality, SCP yields an effective, temperature-dependent harmonic Hamiltonian which minimizes the Helmholtz free energy. In the SCP framework, the best approximation for the effective temperature-dependent harmonic Hamiltonian is obtained by solving iteratively a system of coupled nonlinear equations in a self-consistent fashion. While the method itself is not new, I succeeded in reducing the overall computational cost of the method by several orders of magnitude by incorporating quasi-Monte Carlo integration in place of standard Monte Carlo integration, thereby making it practical for general many-body quantum systems. The newfound utility of this method has been demonstrated by computing a wide array of properties, such as vibrational frequencies and free energies, for polycyclic aromatic hydrocarbons, Lennard-Jones clusters, and water clusters.

Chapter 1

Context and Broad Goals of the Field

In the interest of placing the work to be discussed in subsequent chapters in its proper context, we take time to very briefly review the "big picture" and touch on a few of the major themes driving the fields of theoretical chemistry and molecular simulation.

1.1   The many-body problem: Challenges of scale, scaling, and coupling

The overarching goal of statistical mechanics is to bridge the gap between the microscopic and the macroscopic, that is, to understand how macroscopic properties and phenomena arise from the fundamental physical laws governing the behavior and

interactions of the individual microscopic particles comprising them. This can be achieved very rarely analytically, leaving approximate approaches and computer simulations as the only possible means for achieving this goal. Coupling, i.e., the presence of cross-terms in the Hamiltonian, results in problems for which analytical solutions do not exist. Moreover, the scale of the problem, both spatially and temporally, prevent us from studying most systems at the desired level of resolution. The magnitude of the problem is so large that it cannot and will not be overcome by advances in computer science (e.g., Moore's law), barring some cataclysmic, breakthrough event in computer science. Finally, the exponential scaling of most numerical methods used in molecular simulations prevents the most accurate approaches from being used for systems containing more than a few atoms.

1.2 The Born-Oppenheimer approximation and the potential energy surface

Consider an N-atom system at equilibrium whose behavior is governed by the (time-independent) Schrödinger equation,

$$\hat{H}\psi(\mathbf{R}, \mathbf{r}) = E\psi(\mathbf{R}, \mathbf{r}) \, ,$$

where $\mathbf{R}$ are the nuclear coordinates, $\mathbf{r}$ are the electronic coordinates, and E is the total energy of the system. For this system consisting of N nuclei having masses M_N

and n electrons having masses m_e, the Hamiltonian $\hat{H}$ is given by

$$\hat{H} = \hat{T}_{\text{nuc}}(\mathbf{R}) + \hat{T}_{\text{elec}}(\mathbf{r}) + \hat{V}_{\text{nuc}}(\mathbf{R}) + \hat{V}_{\text{elec}}(\mathbf{r}) + \hat{V}_{\text{nuc, elec}}(\mathbf{R}, \mathbf{r})$$

$$= -\sum_{I=1}^{N} \frac{\hbar^2}{2M_I} \nabla_I^2 - \sum_{i=1}^{n} \frac{\hbar^2}{2m_e} \nabla_i^2 + \frac{1}{4\pi\varepsilon_0} \left[\sum_{I<J} \frac{Z_I Z_J}{|\mathbf{R}_I - \mathbf{R}_J|} + \sum_{i<j} \frac{e^2}{|\mathbf{r}_i - \mathbf{r}_j|} - \sum_{i,I} \frac{eZ_I}{|\mathbf{R}_I - \mathbf{r}_i|} \right] ,$$

$$(1.1)$$

where R_{IJ} is the distance between nuclei I and J, r_{ij} is the distance between electrons i and j, and r_{iI} is the distance between electron i and nucleus I. The first course of action for tackling the problem is to attempt to express the Hamiltonian in a separable form, i.e., as a sum of functions of independent coordinates, so that it can be solved by separation of variables. In trivial cases, this can be achieved exactly simply through an appropriate coordinate transformation, which will depend on the symmetry of the problem (e.g., transforming from cartesian coordinates to spherical coordinates recasts the Hamiltonian for the hydrogen atom in a separable form). In the vast majority of cases the Hamiltonian can only be approximately treated as separable. The most common such approximation is likely the well-known Born-Oppenheimer approximation, in which the terms which couple the nuclear and electronic degrees of freedom are neglected. The Hamiltonian is then approximated as a sum of independent nuclear and electronic contributions, so that the approximate Schrödinger equation can be solved by separation of variables. Applying the Born-Oppenheimer approximation leaves us with the "nuclear dynamics problem",

$$[\hat{T}_{\text{nuc}}(\mathbf{R}) + V(\mathbf{R})]\psi_n(\mathbf{R}) = E\psi(\mathbf{R}) ,$$

giving rise to the notion of a potential energy surface $V(\mathbf{R})$, an effective potential for the nuclei which depends only on the nuclear coordinates. Equilibrium thermodynamic properties can often be expressed in terms of the properties of the individual minima of the PES (via ensemble averages), and dynamical properties on how the minima are connected to one another. The Born-Oppenheimer approximation breaks down when potential energy surfaces corresponding to different electronic states of the system interfere with one another (e.g., surface crossings, conical intersections). However, the methods discussed in this thesis are not intended to be applied to such nonadiabatic systems, and we will not concern ourselves with these cases.

1.3 Normal mode analysis, or the standard harmonic approximation

For the general case when cross-terms are present in the nuclear Hamiltonian, the simplest approach to approximating the solution to the nuclear Schrödinger equation is to apply the standard harmonic approximation, or normal mode analysis. Using the second-order Taylor series expansion of the potential about a local minimum, we construct an orthonormal coordinate system from the eigenvectors of the (mass-scaled) Hessian. In other words, from the orthogonal matrix which diagonalizes the (real, symmetric) Hessian, we obtain an orthogonal transformation (i.e., a linear, norm-preserving transformation) for the system coordinates. Transforming from cartesian to normal mode coordinates allows the Hamiltonian to be expressed as a sum of one-

dimensional harmonic Hamiltonians. The harmonic approximation yields analytic expressions for thermodynamic properties of interest, and is a standard component of molecular dynamics and electronic structure packages. However, because it is built entirely upon a single point of the PES, the local minimum about which the Taylor series is constructed, this approach is very limited. As the equilibrium distribution of configurations to be sampled within the given basin of attraction of the PES becomes more diffuse (i.e., at higher temperature, or for systems with greater quantum character), the standard harmonic approximation becomes less suitable for describing the system.

1.3.1   Abuse of the standard harmonic approximation

The rampant use of empirical *scaling factors* has emerged in a crude attempt to address the inherent limitations of the harmonic approximation without resorting to more complicated and expensive methods that naturally incorporate anharmonic effects. In this scenario the harmonic approximation is used to compute some thermodynamic, dynamic, or structural properties of interest, such as vibrational frequencies or free energies, and the data is subsequently massaged (scaled or shifted) in an attempt to account for anharmonic effects. The appropriate scaling factors must be determined for each particular system, generally using unjustified empirical procedures. As an example, we can consider the work of Temelso and Shields [1], in which scaling factors for several thermodynamic properties of water clusters were determined from second-order vibrational perturbation theory applied to second-order

Møller-Plesset perturbation theory potential energy surfaces. In attempting to determine scaling factors for vibrational frequencies of water clusters, the authors found it necessary to neglect a significant portion of their data. A total of five different water cluster isomers out of the sixteen under consideration were found to exhibit at least one "anomalous" anharmonic frequency. The anomalous frequencies were neglected from the determination of the scaling factors on the basis that they were "outliers", and the authors then present distinct scaling factors for the intermolecular, bending, and stretching modes of water clusters. This example demonstrates, among other things, that anharmonic effects can manifest in nontrivial and unpredictable ways, and that attempting to reduce these effects to a single scalar for a given type of mode (stretch, bend, intermolecular) is not sound. The scaling factors determined in Ref. 1 are clearly not transferable, and are not even able to produce the "anomalous" anharmonic frequencies found in their own sixteen-cluster training set.

1.4 Exploring the landscape

There are a number of challenges associated with exploring the potential energy surface, especially when the landscape is characterized by rugged terrain punctuated with deep wells and steep barriers. The ergodic theorem promises that time-averages (from molecular dynamics simulations) and configuration space averages (from Monte Carlo simulations) will both converge to the true average in the limit of infinite time or infinite number of sampled configurations. In practice, this cannot be fully realized due to finite simulation time, especially in cases where transition probabilities from

one state to another are very small (e.g., when attempting to scale large potential energy barriers), leading to "broken ergodicity". This can be addressed in large part using replica exchange or parallel tempering, but even these approaches are known to be inadequate in many instances, and can still give way to an apparent convergence of the simulation results (see, for example, Ref. [2]). Adequate sampling for quantum systems is especially difficult, due to delocalization. Finally, we are faced again with the scale of the problem in that the number of local minima generally increases exponentially with system size.

The fundamental challenge that the work in this thesis aims to address is the accurate description of the equilibrium distribution of the quantum many-body system. No exact method exists for computing quantum dynamics of condensed phases for anything but the simplest of systems. Among the variety of quantum dynamics methods which have been developed so far, any single method (or class of methods) is either approximate (inaccurate) or strictly limited in its applications (e.g., has poor numerical scaling with the system size) or both. Indeed, all suffer from significant, and in some instances crippling, limitations. For example, the exact-in-principle basis set methods scale exponentially with system size, and the real-time quantum dynamics methods based on path integrals are prohibitively expensive for systems containing more than a few degrees of freedom, due to the well-known numerical sign problem. Several other methods are restricted to the calculation of ground-state properties, e.g., diffusion Monte Carlo [3,4] and the path integral ground state method [5]. Imaginary-time path integral Monte Carlo is routinely used to treat quantum many-body systems, but is limited to calculations of equilibrium properties at finite tem-

peratures. Two popular *ad hoc* quantum dynamics methods based on path integrals, centroid molecular dynamics [6] and ring-polymer molecular dynamics [7,8] are known to produce unphysical artifacts, making them a poor choice in many instances. Perturbation theory for a many-body system is often unreliable and complicated, both numerically and in determining whether it is even suitable for the system at hand. At the other extreme, the harmonic approximation is unique in its ability to provide an essentially complete description of a quantum many-body system with a given potential energy for a large class of systems and properties, without requiring explicit simulation. However, this comes at the price of working with a method which lacks a reliable and practical procedure to either assess its accuracy or improve it in a systematic fashion by including anharmonic corrections. Noteworthy attempts to improve upon the harmonic approximation include a perturbative approach [9] that strives to incorporate anharmonic effects by working with temperature-dependent frequencies. While this method does capture some anharmonic effects, it is also limited in some aspects, such as its ability to account for structural changes (such as cluster expansion) due to thermal fluctuations.

1.5 Why Gaussians?

There are a number of practical reasons for constructing approximate methods in equilibrium statistical physics based on the normal distribution. The primary reasons are that the fundamental properties of the system can be determined analytically from this distribution, and the harmonic/quadratic potential is a good approximation

to the physical potential close to the minimum. The ability to transform a general multivariate normal distribution to a standard normal distribution, and express the multivariate probability density function as a product of the marginal densities leads to separability of the Hamiltonian. In addition, this property makes sampling the distribution using inverse transform sampling practical, which is of particular importance for our implementation of the self-consistent phonons method using quasi-Monte Carlo integration (see Section 4.2). Finally, an important aspect from the perspective of numerical cost and stability is the ability to express expectation values of derivatives in terms of expectation values of lower-order derivatives, or of the function itself, by exploiting the symmetry of the normal distribution (see Sections 3.2 and 8.1.1).

In addition to these practical concerns, the normal distribution possesses many interesting and noteworthy qualities which account for its ubiquity in many fields. For example, the central limit theorem tells us that the mean of a collection of independent, identically distributed random variables having finite mean and variance converges uniformly to the normal distribution in the limit of a large number of random variables. In other words, the normal distribution is an "attractor" distribution, or "stable" distribution. The fundamental postulate of equal *a priori* probabilities in statistical mechanics, that in the absence of any information/constraints, each microstate of the system is equally probable, can be seen as a particular case of the principle of maximum entropy, which states that the distribution which best represents the available information without making any spurious assumptions is that which has the greatest entropy. In the same way that the uniform distribution is the maximum entropy distribution in the absence of any information, the normal

distribution is the maximum entropy distribution subject to the constraints of a particular mean and variance, making it the "best choice" for modeling a distribution for which only these properties are known. In other words, in the context of variational principles, the Gaussian distribution is a natural choice for a trial distribution.

Chapter 2

Combining Gibbs Ensemble Monte Carlo with the Variational Gaussian Wavepacket Method for Computing the Equation of State of a Quantum Liquid

Neon, as well as many other uncharged species which interact primarily by van der Waals interactions, is typically modeled using the Lennard-Jones (LJ) potential, $u_{\mathrm{LJ}}(r) = 4\epsilon[(\sigma/r)^{12} - (\sigma/r)^6]$. The r^{-6} term describes the attractive van der Waals interactions (and gives the true behavior of the induced-dipole-induced-dipole interactions), while the r^{-12} term describes the short-range repulsions due to elec-

tron cloud distortions and overlap. Arguably the most commonly used parameters, $\varepsilon = 35.60\,\mathrm{K}$ and $\sigma = 2.749\,\text{Å}$ were determined from the experimental second virial coefficient [10,11]. Consequently, this model is expected to describe low density states more accurately. Similarly, other empirically derived parameter sets based on limited thermodynamic data are best suited for the phase from which the data was obtained. For this reason, one generally finds that any simple pair potential, such as the LJ potential, is unable to accurately reproduce the complete phase diagram of neon, i.e., both the solid-liquid and liquid-vapor coexistence curves [12].

Moreover, neon has long been known to deviate from the principle of corresponding states, which is well adhered to by other van der Waals fluids such as argon, krypton, xenon, and methane, due to quantum effects [13]. In spite of its deviant behavior, neon can still be expected to be well-described by the LJ potential, provided that its quantum nature is properly addressed. Any classical species modeled by the LJ potential will possess the same properties in reduced units, but we can introduce quantum behavior for particles of mass m to a LJ fluid by way of the de Boer parameter, $\Lambda := \hbar/\sigma\sqrt{m\varepsilon}$ ($\Lambda \approx 0.095$ for neon) [14]. The de Boer parameter can be invoked when using other potentials, as well, in which case ε would correspond to the strength of the potential, and σ to its range.

Here we parametrize the LJ potential for neon by constructing a theoretical prediction for the equation of state of a general quantum LJ fluid, and mapping it to the experimental equation of state for neon. The compilation of data computed over a broad range of temperatures and de Boer parameters is expected to provide a more accurate and consistent fit than parameters based on a single thermodynamic data

point, e.g., the second virial coefficient. Of course, this approach is not limited to neon, and can be used to determine the optimum LJ parameters for any van der Waals fluid. We demonstrate that Gibbs ensemble Monte Carlo coupled with the variational Gaussian wavepacket (VGW) approximation provides an efficient and accurate way to fit the equation of state for a general quantum LJ fluid to the experimental equation of state for a particular chemical species. Constructions of the equation of state of quantum neon have already been attempted using the path integral Monte Carlo combined with the Gibbs ensemble (GE-PIMC) [15], and using thermodynamic integration (TI-PIMC) [12]. We compare our best fit for the experimental equation of state for neon with these results.

This chapter can be viewed as a synopsis of our paper [16].

2.1 Methods

2.1.1 Gibbs Ensemble Monte Carlo

One of the main challenges in simulating phase coexistence for a bulk system is the presence of an interface, and the large portion of particles which comprise it. As Frenkel and Smit note, for systems of 125, 64,000, and 1,000,000 particles arranged in a cubic box, the fraction of particles belonging to the interface is 78%, 14%, and 6%, respectively. Thus, large systems are generally needed in order to prevent surface effects from influencing bulk properties when simulating phase-coexistence directly. Indirect approaches are also rather computationally intensive, as they entail comput-

ing some thermodynamic variable of the two phases independently, and determining where their temperatures, pressures, and chemical potentials are equal [17]. The Gibbs ensemble, developed by Panagiotopoulos in the 1980's [18, 19], allows one to model phase equilibria without an interface, thereby making it possible to work with smaller systems and directly compute phase coexistence properties from a single simulation. In this method two simulation boxes with periodic boundary conditions are used to simulate the two phases, with the temperature T, total volume V, and total number of particles N of the composite system kept constant. The conditions for phase equilibrium, namely, equal temperature, pressure, and chemical potential, are met via three types of Monte Carlo moves: particle displacements within each phase ensure thermal equilibrium, coupled volume displacements ensure mechanical equilibrium, and particle transfers ensure chemical equilibrium. In some sense, the Gibbs ensemble can be thought of as a combination of the canonical, isobaric-isothermal, and grand canonical ensembles. It has been shown to be equivalent to the canonical ensemble in the thermodynamic limit [20].

The partition function for the quantum Gibbs ensemble can be expressed in terms of the canonical partition function $Q = \mathrm{Tr}\left(e^{-\beta \hat{H}}\right)$:

$$\Omega_{\mathrm{Gibbs}}(N, V, T) = \sum_{N_1=0}^{N} \int_0^V \frac{1}{V} \mathrm{Tr}\left(e^{-\beta \hat{H}_1}\right) \mathrm{Tr}\left(e^{-\beta \hat{H}_2}\right) dV_1 , \qquad (2.1)$$

where N_i, $V_i = L_i^3$, and $\hat{H}_i$ $(i = 1, 2)$ are the number of particles, volume, and Hamiltonian for box i. This can in turn be expressed as a function of the quantum densities, ρ_1 and ρ_2, which will be estimated using the variational Gaussian wavepacket (VGW)

14

approximation:

$$\Omega_{\text{Gibbs}}(N, V, T) = \sum_{N_1=0}^{N} \int_0^V \frac{1}{V} \frac{(V_1)^{N_1}(V - V_1)^{N-N_1}}{N_1!(N - N_1)!} dV_1 \cdot \int_0^{L_2} \int_0^{L_1} \rho_1(\mathbf{x}_1)\rho_2(\mathbf{x}_2) d\mathbf{x}_1 d\mathbf{x}_2 \ .$$

(2.2)

2.1.2 The variational Gaussian wavepacket approximation

The VGW approximation was developed as an alternative to the path integral formalism. The principal advantage of the VGW approximation over path integrals is that for a system of N particles, VGW operates in the un-inflated $3N$-dimensional configuration space, while ring polymers increase the dimensionality by a factor of L, the number of beads comprising each ring polymer. In the context of GEMC, VGW allows for single particles to be transferred between boxes rather than cumbersome ring polymers, thereby requiring fewer attempted particle transfers in order to achieve the desired transfer rate. VGW is exact for harmonic systems and in the high-temperature limit.

Consider a quantum N-body system with Hamiltonian

$$\hat{H} = -\frac{\hbar^2}{2} \nabla^T \mathbf{M}^{-1} \nabla + V(\mathbf{r}) \ ,$$

where $\mathbf{M} \in \mathbb{R}^{3N \times 3N}$ is the (diagonal) mass matrix, $\mathbf{r} \in \mathbb{R}^{3N}$ the particle coordinates, and $V(\mathbf{r}) \in \mathbb{R}$ the potential energy surface for the system. The role of VGW is to estimate the equilibrium density matrix, $\rho(\mathbf{x}, \mathbf{x}'; \beta) = \langle \mathbf{x} \mid e^{-\beta \hat{H}} \mid \mathbf{x}' \rangle$ for such a system.

The solutions to the "imaginary-time" Schrödinger equation

$$\frac{\partial}{\partial \tau} \mid \mathbf{x}; \tau \rangle = -\hat{H} \mid \mathbf{x}; \tau \rangle \ .$$

are given by the imaginary-time-dependent wavepacket

$$| \mathbf{x}; \tau \rangle := e^{-\tau \hat{H}} | \mathbf{x}_0 \rangle ,$$

where τ is the imaginary time. We approximate these wavepackets by Gaussians having center $\mathbf{x} \in \mathbb{R}^{3N}$, covariance matrix $\mathbf{G} \in \mathbb{R}^{3N \times 3N}$, and scaling factor $\gamma \in \mathbb{R}$:

$$\langle \mathbf{r} \mid \mathbf{x} \rangle \approx (2\pi)^{\frac{3N}{2}} ||\mathbf{G}||^{-\frac{1}{2}} \exp \left\{ -\frac{1}{2}(\mathbf{r} - \mathbf{x})^T \mathbf{G}^{-1}(\mathbf{r} - \mathbf{x}) + \gamma \right\} . \qquad (2.3)$$

This in turn enables us to represent the diagonal elements of the density matrix analytically by

$$\rho(\mathbf{x}; \beta) = \frac{e^{2\gamma_{\beta/2}}}{(4\pi)^{3N/2}||\mathbf{G}_{\beta/2}||^{1/2}} . \qquad (2.4)$$

The parameters $\mathbf{x} = \mathbf{x}(\tau)$, $\mathbf{G} = \mathbf{G}(\tau)$, and $\gamma = \gamma(\tau)$ are then propagated in imaginary time subject to the time-dependent variational principle [21], which implies the following equations of motion for the Gaussian parameters:

$$\frac{d}{d\tau}\mathbf{x} = -\mathbf{G}\langle \nabla U \rangle \qquad (2.5a)$$

$$\frac{d}{d\tau}\mathbf{G} = -\mathbf{G}\langle \nabla \nabla^T U \rangle \mathbf{G} + \Lambda^2 \qquad (2.5b)$$

$$\frac{d}{d\tau}\gamma = -\frac{1}{4}\mathrm{Tr}\left(\langle \nabla \nabla^T U \rangle \mathbf{G}\right) - \langle U \rangle . \qquad (2.5c)$$

2.2   Results

Gibbs ensemble MC simulations were carried out for two different system sizes, $N = 1024$ and $N = 2048$, over a range of Λ and temperatures. VGW was used to compute the diagonal elements of the density matrix, $\rho(\mathbf{x}) = \langle \mathbf{x} \mid \mathbf{x} \rangle$, in Eq. 2.2.

The acceptance rate for particle displacements was kept between 20% and 40%, and the number of attempted particle transfers N_{transfer} was adjusted so that the number of accepted particle transfers was no more than 2% of the accepted particle displacements. Anywhere from 60,000 to 150,000 MC cycles were carried out for each Λ and T, with each cycle consisting of N attempted particle displacements, a single attempted volume displacement, and N_{transfer} attempted particle transfers. Longer simulations were required at higher temperature, i.e., closer to the critical point, where finite-size effects are more prominent [22, 23]. The initial densities $\rho_1 = N_1/V_1$ and $\rho_2 = N_2/V_2$ were determined using preliminary runs and chosen to maintain $\langle N_1 \rangle \approx \langle N_2 \rangle$.

Histograms for the box densities sampled near the critical point are given in Fig. 2.1 for quantum parameters $\Lambda = 0.080$ and $\Lambda = 0.095$. (Note that the critical temperature for neon is $T_c = 44.5$ K from experiment, or approximately 1.25ε [24].) We see that the finite-size effects are negligible for $T = 1.20\varepsilon$, indicated by the isolated, well-defined peaks centered at the same densities for both $N = 1024$ and $N = 2048$. Closer to the critical point, however, we see the peaks for the smaller system fade into one another for both values of Λ, a consequence of the two boxes switching identity during the simulation. Doubling the system size is able to resolve the peaks for $\Lambda = 0.080$, but not for $\Lambda = 0.095$. We find that finite-size effects are significant only very near the critical point, in agreement with references [17] and [25]. The equilibrium vapor-liquid densities $\langle \rho_g \rangle$ and $\langle \rho_l \rangle$, are shown in Fig. 2.2.

For each Λ, the critical temperature was determined by critical scaling with $\beta = 0.3262$ [25, 26],

$$\rho_l - \rho_g \sim (T_c - T)^\beta \ ,$$

17

and the critical density by the law of rectilinear diameters [17, 27],

$$\frac{\rho_l + \rho_g}{2} = \rho_c + A_\Lambda (T - T_c) \ .$$

From this, the full phase diagram for each lambda was constructed using

$$(\rho_l - \rho_g)^{1/\beta} \sim a_\Lambda T + b_\Lambda \ .$$

When complete phase separation could not be achieved, the simulation was omitted from the construction of the full phase diagram, namely, for $(T, \Lambda) = (1.275\varepsilon, 0.065)$ and $(1.25\varepsilon, 0.095)$.

All four fit parameters, a_Λ, b_Λ, A_Λ, and ρ_c, were found to exhibit a linear dependence on Λ [16], making it possible to interpolate a parametric family of curves for $\Lambda \in [0.065, 0.11]$:

$$\rho_g = \rho_c(\Lambda) + A_\Lambda (T - T_c) - \frac{1}{2}(a_\Lambda T + b_\Lambda)^\beta$$
$$\rho_l = \rho_c(\Lambda) + A_\Lambda (T - T_c) + \frac{1}{2}(a_\Lambda T + b_\Lambda)^\beta \ .$$

The calculated values for a_Λ, b_Λ, A_Λ, ρ_c, and T_c for $\Lambda = 0.65$, 0.08, 0.095 and 0.11 are given in Ref. 16. Finally, the member of this parametric family which best approximates the experimental phase diagram for neon (in the least squares sense) was obtained, yielding $\Lambda = 0.094$, $\varepsilon = 35.68\,\mathrm{K}$, and $\sigma = 2.7616\,\mathrm{\AA}$ as the LJ parameters of best fit. Figure 2.3 compares our results [16] with those of TI-PIMC [12] and GE-PIMC [15] simulations, as well as the experimental data from NIST [24].
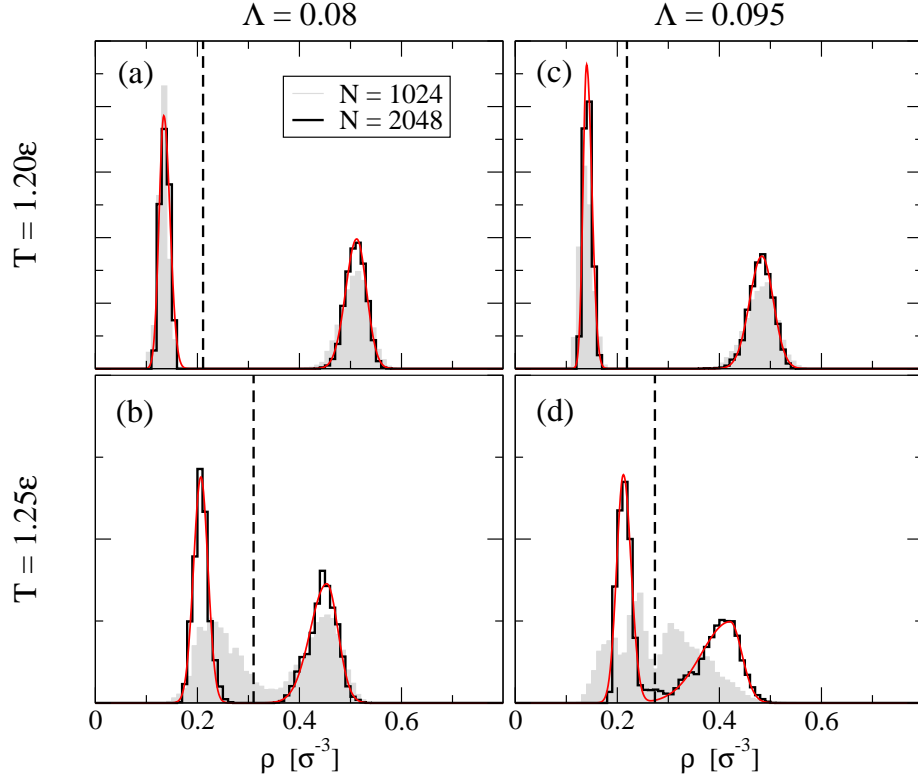
Figure 2.1: Histograms for the sampled box densities, ρ_g and ρ_l, at temperatures $T = 1.20\varepsilon$ (top row) and $T = 1.25\varepsilon$ (bottom row), for de Boer parameters $\Lambda = 0.08$ (left column) and $\Lambda = 0.095$ (right column). Grey fill corresponds to the system of $N = 1024$ particles, and black lines to the system of $N = 2048$ particles. Red lines give the asymmetrical Gaussian fit for the $N = 2048$ results, and the vertical dashed lines give the overall system density, $\rho = N/V = (N_1 + N_2)/(V_1 + V_2)$.
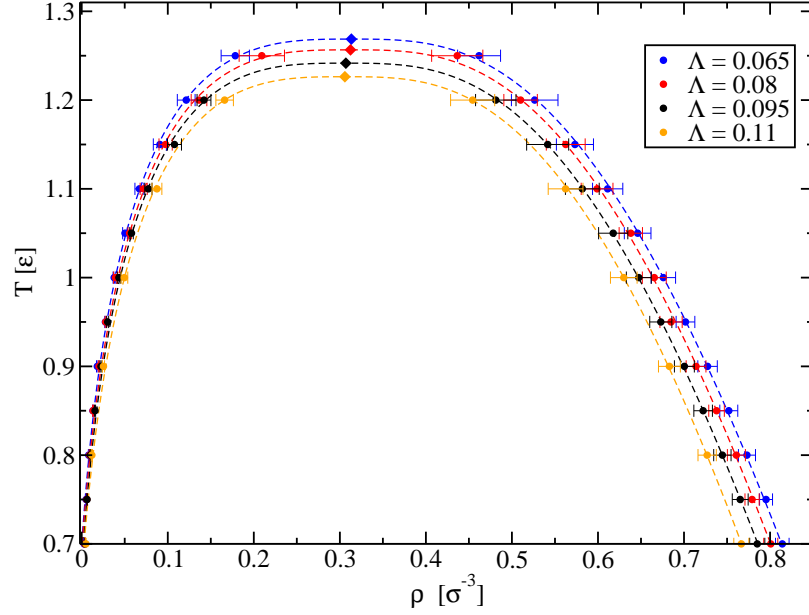
Figure 2.2: Vapor-liquid coexistence curves for various values of de Boer quantum parameter, Λ, computed using GEMC coupled with VGW. The dashed lines are fits for the simulation results obtained using critical scaling and the law of rectilinear diameters [17, 26].
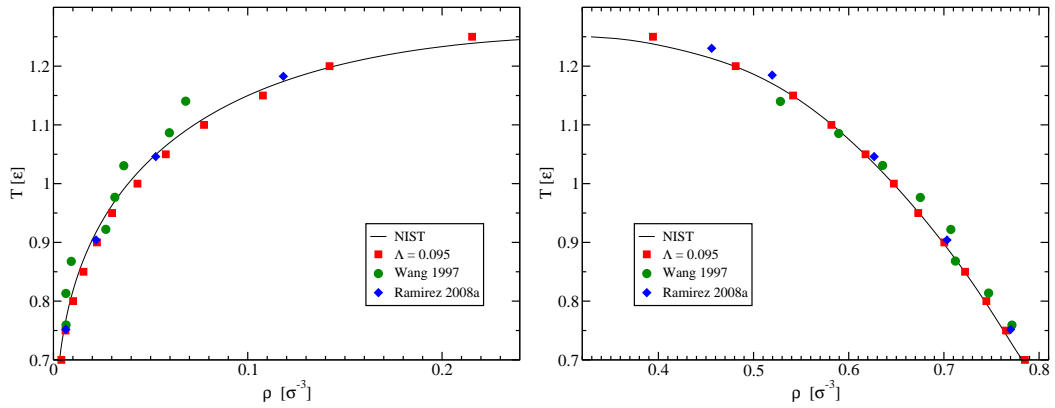
Figure 2.3: Comparison of GEMC-VGW [16], GE-PIMC [15], and TI-PIMC [12] results. Experimental results [24] have been scaled to reduced units using the optimal ε and σ determined by GEMC-VGW, and are given by the solid line.

2.3 Closing remarks

By combining the VGW and GEMC methods, we computed the liquid-vapor coexistence curve for a quantum LJ system as a function of the de Boer parameter. Using this data, we were able to map the experimental data for neon liquid-gas equilibrium to that of the general LJ quantum liquid, and determine the LJ parameters which most accurately reproduce the experimental data over the temperature range $0.7\varepsilon \leq T \leq 1.2\varepsilon$. The efficiency of the VGW method made it possible to consider large systems, significantly reducing the finite-size effects which usually hamper GEMC simulations and leading to a better description of the region near the critical point. Note, however, that at temperatures even closer to the critical point, improving upon the results presented here would still require significantly larger systems.

Chapter 3

The Self-Consistent Phonons

Method

Originally developed in the 1960's by solid state physicists, and rediscovered at least once [28], the self-consistent phonons (SCP) method establishes a consistent numerical framework in which a general, classical or quantum, N-body system at thermal equilibrium is approximated by an effective harmonic system [29,30]. The "best" effective harmonic Hamiltonian is chosen variationally by minimizing the Helmholtz free energy of the system with respect to the center and Hessian of the effective harmonic potential energy surface (PES). The effective harmonic PES is different from the second-order Taylor series expansion of the physical PES, with the anharmonicity of the system manifested in its temperature-dependence. By construction, the method would appear to be ideally suited for a direct estimate of the free energy, however the situation is more complicated than one might expect, as discussed in Chapter 7. Interest in SCP in the context of finite systems has emerged only re-

cently. In Ref. 31, SCP was used to compute the fundamental frequencies of aromatic hydrocarbons, and in Refs. 32 and 33, for computing the ground states of very large Lennard-Jones clusters. Given its inherently approximate nature, an assessment of the accuracy of the method is vitally important, yet surprisingly lacking. To this end, an assessment of the accuracy of the method for computing structural properties of Lennard-Jones clusters is discussed in Chapter 6, and in Ref. 34. In addition to thermodynamic and structural properties, one can exploit the reference harmonic system even further and also try to estimate dynamical properties which depend only on a single minimum of the PES. As an example, Ref. 31 uses SCP to compute infrared spectra of some polycyclic aromatic hydrocarbon molecules, which, at least for the high-frequency modes, display the correct frequency shifts caused by either quantum or thermal effects. Additional examples will be seen in Chapter 8, where vibrational frequencies and spectra for various water clusters are computed using SCP. For the determination of properties which depend on multiple minima, SCP can be applied to each basin of attraction separately, with the contribution of each minimum weighted accordingly. This is effectively the harmonic superposition approach [35] with the SCP approximation replacing the standard harmonic approximation.

3.1   Derivation of the method

Consider a quantum system of N particles described by the Hamiltonian

$$\hat{H} = -\frac{\hbar^2}{2}\nabla^T\mathbf{M}^{-1}\nabla + V(\mathbf{r}) \, , \tag{3.1}$$

where $\mathbf{M} \in \mathbb{R}^{3N \times 3N}$ is the (diagonal) mass matrix, $\mathbf{r} \in \mathbb{R}^{3N}$ the particle coordinates, and $V(\mathbf{r}) \in \mathbb{R}$ the PES of the system. Then supposing that the system lies in a (local) minimum at temperature T, we can approximate the true Hamiltonian about this minimum by a harmonic, temperature-dependent Hamiltonian,

$$\hat{H}_h := -\frac{\hbar^2}{2}\nabla^T \mathbf{M}^{-1}\nabla + \frac{1}{2}(\mathbf{r} - \mathbf{q})^T \mathbf{K}(\mathbf{r} - \mathbf{q}) + V_{\text{min}}. \tag{3.2}$$

Here $\mathbf{K}$ is the Hessian, $\mathbf{q}$ the center, and V_{min} the minimum of the harmonic potential. Then for an operator $\hat{A}$, the ensemble average with respect to $\hat{H}_h$ is given by

$$\langle \hat{A} \rangle_h = \frac{\text{Tr}\left(e^{-\beta \hat{H}_h}\hat{A}\right)}{Q_h}, \tag{3.3}$$

where $Q_h(N, V, T) = \text{Tr}\left(e^{-\beta \hat{H}_h}\right)$ is the canonical partition function of the harmonic system. Note that the canonical partition function of the physical system, $Q(N, V, T) = \text{Tr}\left(e^{-\beta \hat{H}}\right)$ can be expressed exactly as the product of the harmonic partition function Q_h and an expectation value with respect to the harmonic reference system:

$$\begin{aligned} Q &= \text{Tr}\left(e^{-\beta \hat{H}}\right) \\ &= \frac{\text{Tr}\left(e^{-\beta \hat{H}_h}e^{-\beta(\hat{H} - \hat{H}_h)}\right)}{Q_h}Q_h \\ &= \left\langle e^{-\beta(\hat{H} - \hat{H}_h)}\right\rangle_h Q_h . \end{aligned} \tag{3.4}$$

It can be shown as a particular instance of Jensen's inequality (see Appendix A) that for any $\mathbf{x}$

$$\langle e^{\mathbf{x}} \rangle \leq e^{\langle \mathbf{x} \rangle} \tag{3.5}$$

so that

$$Q = \left\langle e^{-\beta(\hat{H} - \hat{H}_h)}\right\rangle Q_h \leq e^{\langle -\beta(\hat{H} - \hat{H}_h)\rangle}Q_h . \tag{3.6}$$

Recalling that the Helmholtz free energy is given by

$$F = -k_{\mathrm{B}} T \log Q \;, \tag{3.7}$$

the Gibbs-Bogoliubov variational principle follows directly:

$$F \leq \langle \mathbf{H} - \mathbf{H}_h \rangle_h + F_h = \langle V(\mathbf{q}) \rangle_h - \langle V_h(\mathbf{q}) \rangle_h + F_h =: F_{\mathrm{trial}} \;. \tag{3.8}$$

Accordingly, we aim to minimize the trial Helmholtz free energy, F_{trial}, with respect to the parameters of the harmonic Hamiltonian, namely, the center $\mathbf{q}$ and Hessian $\mathbf{K}$:

$$\frac{\partial F_{\mathrm{trial}}}{\partial \mathbf{q}} = 0 \tag{3.9a}$$

$$\frac{\partial F_{\mathrm{trial}}}{\partial \mathbf{K}} = \mathbf{0} \;. \tag{3.9b}$$

The canonical partition function for a system of $3N$ quantum harmonic oscillators is

$$Q_h = e^{-\beta V_h} \frac{2N}{\mathcal{N}} \left\| 2 \sinh \left(\frac{\hbar \beta}{2} \tilde{\mathbf{K}}^{1/2} \right) \right\| \;, \tag{3.10}$$

where $\mathcal{N}$ is the order of the point group and $2N!/\mathcal{N}$ is the number of permutational isomers. The Helmholtz free energy of this harmonic system is

$$F_h = -k_{\mathrm{B}} T \log Q_h = k_{\mathrm{B}} T \log \left\| 2 \sinh \left(\frac{\hbar \beta}{2} \tilde{\mathbf{K}}^{1/2} \right) \right\| \;. \tag{3.11}$$

In order to avoid a lengthy and tedious application of the chain rule, we introduce a third variational parameter $\mathbf{D}$, the displacement-displacement correlation matrix,

$$
\begin{aligned}
\mathbf{D} &= \langle (\mathbf{r} - \mathbf{q})(\mathbf{r} - \mathbf{q}) \rangle_h \\
&= \frac{1}{Q_h} \mathrm{Tr} \left((\mathbf{r} - \mathbf{q})(\mathbf{r} - \mathbf{q})^{\mathrm{T}} e^{-\beta \hat{H}_h} \right) \\
&= \mathbf{M}^{-1/2} d(\tilde{\mathbf{K}}^{1/2}) \mathbf{M}^{-1/2} \;,
\end{aligned}
\tag{3.12}
$$

where $\tilde{\mathbf{K}} := \mathbf{M}^{-1/2}\mathbf{K}\mathbf{M}^{-1/2}$ is the mass-scaled Hessian, and the auxiliary function d is defined by

$$d(\omega) := \frac{\hbar}{2\omega}\coth\left(\frac{\hbar\beta\omega}{2}\right) . \tag{3.13}$$

With the introduction of $\mathbf{D}$, the ensemble averages with respect to the reference harmonic system can be expressed as

$$\langle f(\hat{\mathbf{r}})\rangle_h := \mathrm{Tr}\left(f(\hat{\mathbf{r}})e^{-\beta\hat{H}_h}\right)$$
$$= ||2\pi\mathbf{D}||^{-1/2}\int f(\mathbf{x})e^{-\frac{1}{2}(\mathbf{x}-\mathbf{q})^{\mathrm{T}}\mathbf{D}^{-1}(\mathbf{x}-\mathbf{q})}d\mathbf{x} . \tag{3.14}$$

In other words, $\mathbf{D}$ is the covariance matrix for the multivariate normal distribution of coordinates of the harmonic reference system.

The upper bound for the Helmholtz free energy of the system when using the harmonic reference is then

$$F \le F_{\text{trial}} := F_h + \langle V\rangle_h - \langle V_h\rangle_h$$
$$= k_{\text{B}}T\log\left|\left|2\sinh\left(\frac{\hbar\beta}{2}\tilde{\mathbf{K}}^{1/2}\right)\right|\right| \tag{3.15}$$
$$+ \langle V_h\rangle_h - k_{\text{B}}T\,\mathrm{Tr}(\mathbf{K}\mathbf{D}) .$$

Differentiating with respect to our variational parameters $\mathbf{q}$, $\mathbf{K}$, and $\mathbf{D}$, we find that F_{trial} attains its minimum when

$$\frac{\partial\langle V\rangle_h}{\partial\mathbf{q}} = -\langle\nabla V\rangle_h = 0 \tag{3.16a}$$

$$\frac{\partial F_{\text{trial}}}{\partial\mathbf{K}} = \frac{\partial F_h}{\partial\mathbf{K}} - \frac{1}{2}\mathbf{D} = 0 \tag{3.16b}$$

$$\frac{\partial F_{\text{trial}}}{\partial\mathbf{D}} = \frac{1}{2}\langle\nabla\nabla^{\mathrm{T}}V\rangle_h - \frac{1}{2}\mathbf{K} = 0 . \tag{3.16c}$$

Note that although we have treated $\mathbf{D}$ and $\mathbf{K}$ as independent parameters to simplify the differentiation, their dependence on one another is enforced by Eq. 3.16b. From

26

Eqs. 3.16a and 3.16c, we find that minimizing the trial Helmholtz free energy with respect to $\mathbf{q}$ and $\mathbf{K}$ leads to a system of coupled nonlinear equations

$$\langle \nabla V \rangle_h = 0 \tag{3.17a}$$

$$\langle \nabla \nabla^{\mathrm{T}} V \rangle_h = \mathbf{K} \ . \tag{3.17b}$$

which we will refer to simply as the *SCP equations*.

Equivalently, we can formulate the SCP method beginning from the more general concept of the Kullback-Leibler divergence, which provides a measure of the difference between two probability distributions. For probability distributions $\mathcal{P}_0$ and $\mathcal{P}$, the Kullback-Leibler divergence D from $\mathcal{P}$ to $\mathcal{P}_0$ is defined as

$$D(\mathcal{P}_0||\mathcal{P}) = \left\langle \log \frac{\mathcal{P}_0}{\mathcal{P}} \right\rangle_0 \ ,$$

where $\langle \cdot \rangle_0$ denotes that the expectation value is taken with respect to the distribution $\mathcal{P}_0$. In particular, for two discrete distributions having probability mass functions p and p_0 whose outcomes are indexed by k, i.e., with $\mathcal{P}(\mathbf{X} = \mathbf{x}_k) = p_k$ and $\mathcal{P}_0(\mathbf{X} = \mathbf{x}_k) = p_{0k}$, (discrete random variable $\mathbf{X}$)

$$D(p_0||p) = \sum_k p_{0k} \log \frac{p_{0k}}{p_k} \ .$$

This quantity is defined only under the condition of absolute continuity, i.e., only when p_0 is absolutely continuous with respect to p, i.e., only if $p_{0k} = 0$ whenever $p_k = 0$. In the case of two continuous distributions having probability density functions f and f_0 on their support $\mathcal{D}$, (continuous random variable $\mathbf{X}$),

$$D(f_0||f) = \int_{\mathcal{D}} f_0(\mathbf{x}) \log \frac{f_0(\mathbf{x})}{f(\mathbf{x})} \, d\mathbf{x} \ .$$

By applying Jensen's inequality to the logarithm function, it can be shown (see Appendix A) that $D(\mathcal{P}_0||\mathcal{P}) \geq 0$ for any $\mathcal{P}_0$ and $\mathcal{P}$ (also known as Gibbs' inequality), with equality holding if and only if $\mathcal{P}_0 \equiv \mathcal{P}$ i.e., when $\mathcal{P}_0(\mathbf{q})$ is identically $\mathcal{P}(\mathbf{q})$. Note also that the Kullback-Leibler divergence is not symmetric, i.e., $D(\mathcal{P}_0||\mathcal{P}) \neq D(\mathcal{P}||\mathcal{P}_0)$, and does not satisfy the triangle inequality. In other words, it does not meet the definition of a metric, but can be considered a *premetric*.

The reader is likely to have noticed the resemblance between the Kullback-Leibler divergence and the general expression for the entropy $\mathcal{H}$ of a distribution:

$$
\begin{aligned}
\mathcal{H} &:= \sum_k p_k \log p_k \quad \text{(discrete distribution)} \\
\mathcal{H} &:= \int f(\mathbf{x}) \log f(\mathbf{x}) \, d\mathbf{x} \quad \text{(continuous distribution)} .
\end{aligned}
\tag{3.18}
$$

The Kullback-Leibler divergence, also referred to as the relative entropy, differs from the entropy by a so-called *cross entropy* term:

$$
\begin{aligned}
D(\mathcal{P}_0||\mathcal{P}) &= \left\langle \log \frac{\mathcal{P}_0}{\mathcal{P}} \right\rangle_0 = \sum_k \mathcal{P}_{0k} \log \frac{\mathcal{P}_{0k}}{\mathcal{P}_k} \\
&= \sum_k \mathcal{P}_{0k} \log \mathcal{P}_{0k} - \sum_k \mathcal{P}_{0k} \log \mathcal{P}_k = \underbrace{H(\mathcal{P}_0)}_{\text{entropy}} - \underbrace{H(\mathcal{P}_0, \mathcal{P})}_{\text{cross entropy}} .
\end{aligned}
\tag{3.19}
$$

Given the completely general nature of Eq. 3.19 (not to mention the broad class of functions that Jensen's inequality applies to), it should come as no surprise that approaches based on maximization of the entropy or minimization of the cross entropy (or Kullback-Leibler divergence) can be applied to a variety of optimization problems [36]. A notable example from chemical physics is the use of relative entropy minimization as the basis for constructing a coarse-grained potential which optimally represents a particular all-atom model [37, 38].

Consider in particular the canonical/Boltzmann distribution $\mathcal{P}$ for a classical system of N particles with Hamiltonian H governed by the potential $V(\mathbf{q})$, and suppose that we wish to approximate this distribution by a distribution $\mathcal{P}_0$ with Hamiltonian H_0 and governed by the potential $V_0(\mathbf{r})$,

$$P_0(\mathbf{r}) = \frac{e^{-\beta H_0(\mathbf{r},\mathbf{p})}}{Q_0} = \frac{e^{-\beta V_0(\mathbf{r})}}{Z_0}$$

$$P(\mathbf{r}) = \frac{e^{-\beta H(\mathbf{r},\mathbf{p})}}{Q} = \frac{e^{-\beta V(\mathbf{r})}}{Z} \; ,$$

where Q_0 and Q are the canonical partition functions, and Z_0 and Z are the configurational partition functions. Then

$$D(\mathcal{P}_0||\mathcal{P}) := \left\langle \log \frac{\mathcal{P}_0}{\mathcal{P}} \right\rangle_0 = \log \left(\frac{Z}{Z_0} \right) + \langle \beta[V(\mathbf{r}) - V_0(\mathbf{r})] \rangle_0 \; . \qquad (3.20)$$

Recalling again that the Helmholtz free energy is given by $F = -\frac{1}{\beta} \log Q$, we arrive once more to the Gibbs-Bogoliubov inequality

$$F + D(\mathcal{P}_0||\mathcal{P}) = F_0 + \langle V(\mathbf{r}) \rangle_0 - \langle V_0(\mathbf{r}) \rangle_0 \geq F \; , \qquad (3.21)$$

only now we see clearly that the difference between the trial Helmholtz free energy $F_{\text{trial}} := F_0 + \langle V(\mathbf{r}) \rangle_0 - \langle V_0(\mathbf{r}) \rangle_0$ and the true Helmholtz free energy of the system F is $D(\mathcal{P}_0||\mathcal{P})$. Clearly, minimizing the quantity $F_0 + \langle V(\mathbf{r}) \rangle_0 - \langle V_0(\mathbf{r}) \rangle_0$ is equivalent to minimizing the Kullback-Leibler divergence from the distribution of the actual system to the distribution of the reference/model system.

At this point a particular form for the reference/model potential V_0 must be proposed, and we return to our harmonic form for V_0, corresponding to a (multivariate) normal distribution, which is a natural choice for a variety of reasons (see Section 1.5).

For the special case of a classical system described by the Hamiltonian,

$$H_h(\mathbf{r}, \mathbf{p}) = \frac{1}{2}\mathbf{p}^\mathrm{T}\mathbf{M}^{-1}\mathbf{p} + \frac{1}{2}(\mathbf{r} - \mathbf{q})^\mathrm{T}\mathbf{K}(\mathbf{r} - \mathbf{q}) \,, \tag{3.22}$$

one can proceed in a completely analogous fashion, beginning with the canonical partition function Q_h for a collection of $3N$ classical harmonic oscillators

$$\begin{aligned} Q_h &= \int e^{-\beta H_h(\mathbf{r}, \mathbf{p})} d\mathbf{r}\, d\mathbf{p} \\ &= \int e^{\frac{1}{2}\beta \mathbf{p}^\mathrm{T}\mathbf{M}^{-1}\mathbf{p} + \frac{1}{2}\beta(\mathbf{r} - \mathbf{q})^\mathrm{T}\mathbf{K}(\mathbf{r} - \mathbf{q})} d\mathbf{r}\, d\mathbf{p} \\ &= (2\pi k_\mathrm{B}T)^{3N} ||\tilde{\mathbf{K}}||^{-1/2} \,. \end{aligned} \tag{3.23}$$

The Helmholtz free energy is then given by

$$\begin{aligned} F_h &= 3N k_\mathrm{B}T \log(2\pi k_\mathrm{B}T) + k_\mathrm{B}T \log ||\tilde{\mathbf{K}}|| \\ &= 3N k_\mathrm{B}T \log(2\pi k_\mathrm{B}T) + k_\mathrm{B}T \sum_{k=1}^{3N} \log \omega_k \,. \end{aligned} \tag{3.24}$$

Of course,

$$\begin{aligned} \langle V_h(\mathbf{r})\rangle_h &= (2\pi k_\mathrm{B}T)^{-3N/2} ||\tilde{\mathbf{K}}||^{1/2} \int \frac{1}{2}(\mathbf{r} - \mathbf{q})^\mathrm{T}\mathbf{K}(\mathbf{r} - \mathbf{q})\, e^{-\frac{1}{2}\beta(\mathbf{r} - \mathbf{q})^\mathrm{T}\mathbf{K}(\mathbf{r} - \mathbf{q})}\, d\mathbf{r} \\ &= \frac{3N}{2} k_\mathrm{B}T \,, \end{aligned} \tag{3.25}$$

which is just a particular instance of the equipartition theorem, and

$$\langle V(\mathbf{r})\rangle_h = (2\pi k_\mathrm{B}T)^{-3N/2} ||\tilde{\mathbf{K}}||^{1/2} \int V(\mathbf{r})\, e^{-\frac{1}{2}\beta(\mathbf{r} - \mathbf{q})^\mathrm{T}\mathbf{K}(\mathbf{r} - \mathbf{q})}\, d\mathbf{r} \,. \tag{3.26}$$

Taken all together, we have

$$\begin{aligned} F \le F_\mathrm{trial} &:= F_h + \langle V\rangle_h - \langle V_h\rangle_h \\ &= 3N k_\mathrm{B}T \log(2\pi k_\mathrm{B}T) + k_\mathrm{B}T \log ||\tilde{\mathbf{K}}|| \\ &\quad + \langle V_h\rangle_h - \frac{3N}{2} k_\mathrm{B}T \,. \end{aligned} \tag{3.27}$$

As before, minimizing F_{trial} with respect to the parameters of the harmonic Hamiltonian leads to

$$\langle \nabla V \rangle_h = 0$$

$$\langle \nabla \nabla^{\mathrm{T}} V \rangle_h = \mathbf{K} \ .$$

Of course, working through the classical case in this manner is redundant, as it can be arrived at simply by considering the classical ($\hbar \to 0$) limit of the more general quantum expressions.

3.2   Solving the SCP equations

Returning to the SCP equations,

$$\langle \nabla V \rangle_h = 0$$

$$\langle \nabla \nabla^{\mathrm{T}} V \rangle_h = \mathbf{K} \ ,$$

we note that this is a system of coupled nonlinear equations, which is amenable to an iterative solution until self-consistency is reached, hence the method's name. This can be carried out by way of a Newton-Raphson-type approach. Beginning with initial configuration $\mathbf{q}$ and Hessian $\mathbf{K}$, the subsequent $\mathbf{q}$, $\mathbf{K}$, and $\mathbf{D}$ are given by

$$\mathbf{D}^{(\text{next})} = \mathbf{M}^{-1/2} d \left(\tilde{\mathbf{K}}^{1/2} \right) \mathbf{M}^{-1/2} \tag{3.30a}$$

$$\mathbf{K}^{(\text{next})} = \langle \nabla \nabla^{\mathrm{T}} V \rangle_h \tag{3.30b}$$

$$\mathbf{q}^{(\text{next})} = \mathbf{q} - \mathbf{K}^{-1} \langle \nabla V \rangle_h \ . \tag{3.30c}$$

Eq. 3.30c has the effect of driving the simulation toward the apparent solution at each iteration at a faster rate along the slow degrees of freedom, and at a slower rate along the fast degrees of freedom. Highly anharmonic vibrational modes can lead to a Hessian matrix which is ill-conditioned, so that the error in the product $\mathbf{K}^{-1} \langle \nabla V \rangle_h$ will be significantly greater than the error in $\langle V \rangle_h$, leading to instability in the iterative procedure via Eq. 3.30c. As an example, the low-frequency, intermolecular modes of water clusters are potentially problematic for this particular approach. To circumvent this problem, one can instead introduce a parameter $\tau > 0$ in place of $\mathbf{K}^{-1}$, whose value can be determined empirically such that the stability of the method is maintained without sacrificing too much in the way of the rate of convergence:

$$\mathbf{q}^{(\text{next})} = \mathbf{q} - \tau \langle \nabla V \rangle_h \ . \tag{3.31}$$

Another variant intermediate to Eq. 3.30c and 3.31 makes use of the fact that even when $\mathbf{K}$ has a very high condition number, the condition number of $\mathbf{D}$ will still be significantly smaller (a reflection of Eq. 3.12). In this case, using $\tau \mathbf{D}$ in place of either τ or $\mathbf{K}^{-1}$ alone provides the best rate of convergence of the method while avoiding the instability caused by a very ill-conditioned Hessian:

$$\mathbf{q}^{(\text{next})} = \mathbf{q} - \tau \mathbf{D} \langle \nabla V \rangle_h \ . \tag{3.32}$$

In either case, a value of τ which is too large will cause the algorithm to become unstable and diverge, while a value of τ which is too small will result in an unnecessary decrease in the rate of convergence. Although we have not encountered any numerical problems with the implementation of Eq. 3.32, they have the potential to arise if (after projecting out the rotational/translation subspace) $\mathbf{K}$ is highly ill-conditioned,

in which case an additional regularization may be required to maintain the stability of the approach.

3.2.1 Projecting out the Eckart subspace

For an isolated molecule or cluster at thermal equilibrium the Hamiltonian must exhibit translational and rotational invariance (a consequence of Noether's theorem and the conservation of linear and angular momentum) [39]. As a result, the solution of the SCP equations, Eqs. 3.17 corresponds to a singular Hessian matrix with six zero-eigenfrequencies ω_k. (Of course, for the special case of a linear molecule, only five zero-eigenvalues are observed, while a bulk system does not exhibit rotational invariance.) According to Eqs. 3.12 and 3.13, those in turn correspond to infinite eigenvalues d_k of matrix $\tilde{\mathbf{D}}$. Away from equilibrium, coupling of the rotational and vibrational degrees of freedom causes only the three translational eigenfrequencies to be always zero, while the three rotational eigenfrequencies become zero only when the stationarity condition, $\langle \nabla V \rangle_h = 0$, is satisfied exactly. One way to circumvent the problem is to exclude the six-dimensional translational/rotational subspace as follows.

The translational subspace is formed by the following three basis vectors

$$
\begin{aligned}
\mathbf{e}_1 &= (1,0,0,\ldots,1,0,0)^{\mathrm{T}} \\
\mathbf{e}_2 &= (0,1,0,\ldots,0,1,0)^{\mathrm{T}} \\
\mathbf{e}_3 &= (0,0,1,\ldots,0,0,1)^{\mathrm{T}},
\end{aligned}
\tag{3.33}
$$

and the rotational subspace by

$$\mathbf{e}_4 \;=\; (0, z_{1,\alpha}, -y_{1,\alpha}, \ldots, 0, z_{N,\alpha}, -y_{N,\alpha})^{\mathrm{T}} \tag{3.34}$$

$$\mathbf{e}_5 \;=\; (-z_{1,\alpha}, 0, x_{1,\alpha}, \ldots, -z_{N,\alpha}, 0, x_{N,\alpha})^{\mathrm{T}}$$

$$\mathbf{e}_6 \;=\; (y_{1,\alpha}, -x_{1,\alpha}, 0, \ldots, y_{N,\alpha}, -x_{N,\alpha}, 0)^{\mathrm{T}}.$$

The corresponding mass-scaled vectors are

$$\tilde{\mathbf{e}}_k = \mathbf{M}^{1/2} \mathbf{e}_k \quad (k = 1, ..., 6). \tag{3.35}$$

These vectors are then orthonormalized using the Gramm-Schmidt procedure to form

a new set, which for simplicity we also define by $\{\tilde{\mathbf{e}}_k\}$. Next, we define the projector

onto the mass-scaled translational/rotational subspace

$$\mathbf{Q} := \sum_{k=1}^{6} \tilde{\mathbf{e}}_k \tilde{\mathbf{e}}_k^{\mathrm{T}}, \tag{3.36}$$

and the projector onto the complementary (Eckart) subspace

$$\mathbf{P} := \mathbf{I} - \mathbf{Q}. \tag{3.37}$$

Consequently, the eigendecomposition of $\tilde{\mathbf{K}}$ (Eq. 3.38) is replaced by the eigendecom-

position of $\mathbf{P}\tilde{\mathbf{K}}\mathbf{P}$, which is a singular matrix with exactly six zero-eigenvalues:

$$\mathbf{P}\tilde{\mathbf{K}}\mathbf{P} = \tilde{\mathbf{U}} \operatorname{diag}(\omega_k^2)\tilde{\mathbf{U}}^{\mathrm{T}}. \tag{3.38}$$

In order to carry out the iterative procedure

$$\mathbf{D}^{(\text{next})} = \mathbf{M}^{-1/2} d\left(\tilde{\mathbf{K}}^{1/2}\right) \mathbf{M}^{-1/2} \tag{3.39a}$$

$$\mathbf{K}^{(\text{next})} = \left\langle \nabla\nabla^{\mathrm{T}} V \right\rangle_h \tag{3.39b}$$

$$\mathbf{q}^{(\text{next})} = \mathbf{q} - \tau \mathbf{D} \left\langle \nabla V \right\rangle_h , \tag{3.39c}$$

it is necessary to evaluate $\tilde{\mathbf{K}}^{-1}$, $\tilde{\mathbf{D}}^{-1}$, etc. Being functions of one another, the matrices $\tilde{\mathbf{D}}$ and $\tilde{\mathbf{K}}$ can be diagonalized simultaneously,

$$\tilde{\mathbf{K}} = \tilde{\mathbf{U}} \operatorname{diag}(\omega_k^2) \tilde{\mathbf{U}}^{\mathrm{T}} \tag{3.40}$$

$$\tilde{\mathbf{D}} = \tilde{\mathbf{U}} \operatorname{diag}(d_k) \tilde{\mathbf{U}}^{\mathrm{T}} , \tag{3.41}$$

with $d_k := d(\omega_k)$ and $\tilde{\mathbf{U}}\tilde{\mathbf{U}}^{\mathrm{T}} = \mathbf{I}$ (the matrices are real symmetric). The matrices in question are then formed by

$$\tilde{\mathbf{D}}^{1/2} = \sum_{k=1}^{3N-6} (d_k)^{1/2} \tilde{\mathbf{U}}_k \tilde{\mathbf{U}}_k^{\mathrm{T}} \tag{3.42a}$$

$$\tilde{\mathbf{D}}^{-1} = \sum_{k=1}^{3N-6} (d_k)^{-1} \tilde{\mathbf{U}}_k \tilde{\mathbf{U}}_k^{\mathrm{T}} \tag{3.42b}$$

$$\tilde{\mathbf{K}}^{-1} = \sum_{k=1}^{3N-6} (\omega_k)^{-2} \tilde{\mathbf{U}}_k \tilde{\mathbf{U}}_k^{\mathrm{T}} , \tag{3.42c}$$

where the sums are evaluated over the $(3N - 6)$ nonzero eigenvalues ω_k and the integral in Eq. 3.14 is effectively computed over the corresponding $(3N - 6)$-dimensional subspace (the Eckart subspace). The evaluation of these integrals will be discussed in detail in Chapter 5.

Chapter 4

Quasi-Monte Carlo Integration

Prior to introducing our dramatically improved implementation of the self-consistent phonons method (Chapter 5), we take some time to discuss the numerical integration and random variate transformation methods upon which this breakthrough primarily rests.

4.1 Low-discrepancy sequences and quasi-Monte Carlo

Standard Monte Carlo integration employs random or pseudorandom numbers to approximate the integral

$$\int f(\xi)d\xi \approx \frac{1}{N} \sum_{n=1}^{N} f(x_n) \, ,$$

achieving a convergence rate of $O(N^{-1/2})$. Although it is very robust, its performance is limited by the clustering of points and the presence of holes over the domain of

integration. Quasi-Monte Carlo, by contrast, uses deterministic *low-discrepancy*, or

quasirandom sequences whose points are correlated so as to prevent clustering and

provide better uniformity over the domain of integration. The behavior of the two

types of sequences is illustrated in Fig. 4.1. For a d-dimensional integral, quasi-Monte

Carlo integration achieves a convergence rate of $O((\log N)^d N^{-1})$, although empirical

results have found convergence rates of $O(N^{-1})$ for certain types of integrands [40].

A quantitative measure of the uniformity of a sequence is given by its discrepancy.

Consider a d-dimensional sequence $\{\mathbf{x}_n\}$ on the unit cube $[0,1]^d$. Let $J(\mathbf{a}, \mathbf{b}) =$

$\Pi_{i=1}^d [a_i, b_i)$ denote the rectangular interval with antipodal vertices $\mathbf{a}$ and $\mathbf{b}$, $\mathrm{Vol}(J)$

denote the volume of such an interval, and $E^* = \{J(\mathbf{0}, \mathbf{b}) : J \subset [0,1]^d\}$ denote the

set of all such subintervals of $[0,1]^d$ having one vertex at the origin. Then the star

discrepancy D_N^* of the sequence is defined by taking the L^∞ norm of $\frac{|\{x_i \in J\}|}{N} - \mathrm{Vol}(J)$

over E^*, i.e.,

$$D_N^*(x_1, \ldots, x_N) = \sup_{J \in E^*} \left| \frac{|\{x_i \in J\}|}{N} - \mathrm{Vol}(J) \right| .$$

Other definitions for discrepancy can be given by using different norms and sets of

subintervals [41].

An infinite sequence $\{\mathbf{x}_n\}$ is said to be uniformly distributed if

$$\lim_{N \to \infty} D_N^*(\mathbf{x}_1, \ldots, \mathbf{x}_N) = 0 .$$

A d-dimensional sequence is typically considered to be a low-discrepancy sequence if

its discrepancy is bounded as

$$D_N \leq c \frac{(\log N)^d}{N}$$

for all N, where c is some constant independent of N. Such sequences are believed
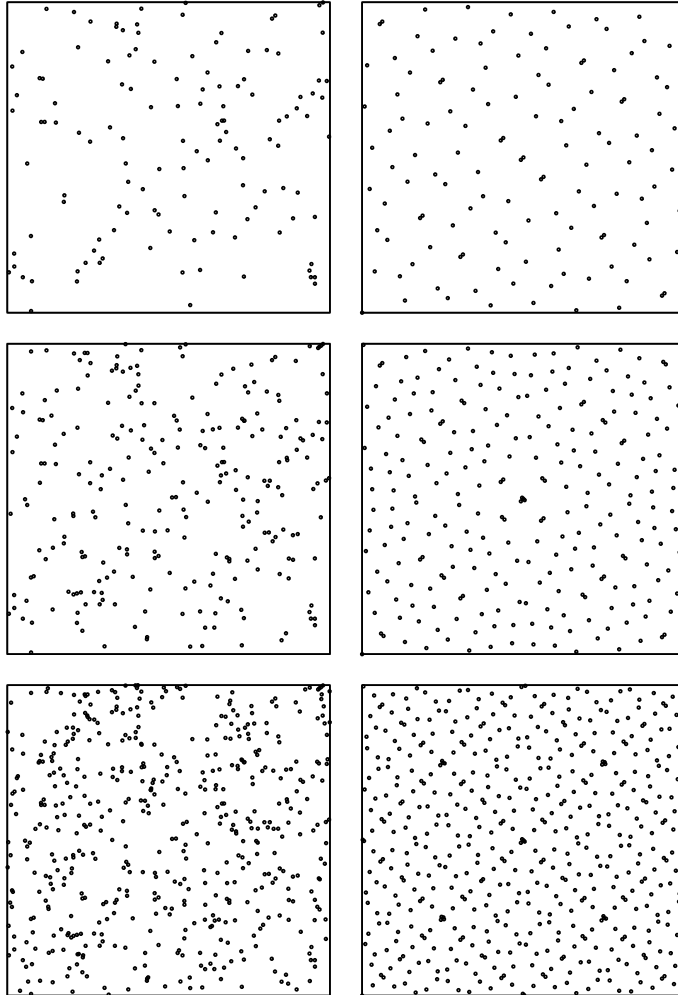
Figure 4.1: A comparison of two-dimensional pseudorandom (left) and Sobol sequences (right) on $[0, 1]^2$, composed of the first 128, 256, and 512 points, respectively. The pseudorandom points have a tendency to clump, while successive points in the Sobol sequence fill in holes as they are added.

to have the best possible order of discrepancy, though this has only been proven in the one- and two-dimensional cases. The expectation value of the discrepancy of a random sequence is bounded by $O((\log \log N)^{1/2} N^{-1})$ from the law of iterated logarithms [42, 43].

The Koksma-Hlawka inequality serves as a basis for error analysis when using quasi-Monte Carlo integration. It states that if a function f has bounded variation $V_{\text{HK}}(f)$ on $[0,1]^d$ in the sense of Hardy and Krause, then for *any* finite sequence $\{\mathbf{x}_1, \ldots, \mathbf{x}_N\} \in [0,1]^d$, we have

$$\left| \frac{1}{N} \sum_{n=1}^{N} f(\mathbf{x}_n) - \int_{[0,1]^d} f(\xi) d\xi \right| \leq V_{\text{HK}}(f) D_N^*.$$

Provided that the indicated partial derivatives are continuous on $[0,1]^d$, the Hardy-Krause total variation of a function f is given by

$$V_{\text{HK}}(f) = \sum_{k=1}^{d} \sum_{1 \leq i_1 < \cdots < i_k \leq d} V_{\text{HK}}^{(k)}(f; i_1, \ldots, i_k) \,,$$

where

$$V_{\text{HK}}^{(d)}(f) = \int_0^1 \cdots \int_0^1 \left| \frac{\partial^d f}{\partial \xi_1 \cdots \partial \xi_d} \right| d\xi_1 \cdots d\xi_d \,.$$

Several well-known low-discrepancy sequences exist, including the Halton [44], Sobol [45, 46], Faure [47], and Niederreiter sequences [48]. Sobol sequences have shown superior performance in comparison studies [43, 49]. The construction of a Sobol sequence, or of each component of a d-dimensional Sobol sequence, is based on a primitive polynomial over the Galois field $GF(2) = \{0, 1\}$, i.e., a polynomial of the form

$$P = x^q + a_{q-1} x^{q-1} + \ldots + a_1 x + 1$$

whose coefficients a_i are 0 or 1. Beginning with (somewhat) arbitrary $m_1, \ldots, m_q$ odd such that $m_i < 2^i$, a sequence of integers $\{m_k\}$ is recursively defined by

$$m_k = 2a_1 m_{k-1} \oplus 2^2 a_2 m_{k-2} \oplus \cdots \oplus 2^{q-1} a_{q-1} m_{k-q+1} \oplus \left(2^q m_{k-q} \oplus m_{k-q}\right) ,$$

where $\oplus$ is the bitwise exclusive-or operator, XOR. The *direction vectors*, v_k are then given by

$$v_k = \frac{m_k}{2^k}, \quad k = 1, 2, \ldots, N .$$

To generate x_n, the nth term of the sequence, n is expressed in binary as $n = b_w b_{w-1} \ldots b_2 b_1$, and x_n is given by

$$x_n = b_w v_w \oplus b_{w-1} v_{w-1} \oplus \ldots \oplus b_1 v_1 .$$

Sobol provides a recommended set of starting values which result in sequences with an additional uniformity property [46]. Primitive polynomials of lower degree lead to improved error bounds [45]. Joe and Kuo provide additional primitive polynomials and direction numbers for generation of Sobol sequences up to 1111 dimensions [50]. A complete account of generation of Sobol sequences is given by Bratley and Fox [51], including the more efficient Gray code implementation developed by Antonov and Saleev [52].

Quasi-Monte Carlo is often better suited than grid-based methods for numerical integration in high dimension for a number of reasons. First, it is difficult to lay a grid in high dimension; the simplest grid requires 2 points in each dimension, or 2^d points for a d-dimensional grid. (In the case of naphthalene, $d = 54$, this is already on the order of 10^{16} points.) Additionally, refining such a grid would require an additional 2^d points. The number of points comprising the grid must be predetermined, whereas

the accuracy of standard or quasi-Monte Carlo methods can be improved incrementally by adding any number of points to the pre-existing set. Finally, when using a grid only one component is varied between adjacent points, while pseudorandom and quasirandom sequences allow any number of components to be varied between any two points, leading to more efficient sampling over the domain of integration.

4.2   Random variate generation

As a particular application of inverse transform sampling, the inverse cumulative distribution function (CDF) for the standard normal distribution can be used to transform uniformly distributed Sobol points on $[0, 1]^d$ to sample the standard normal distribution. Given a random variate U uniformly distributed on $[0, 1]$, a random variate X with cumulative distribution function F can be generated from U using the inverse CDF of X:

$$X = F^{-1}(U) \, .$$

The brief proof can be found in [53]. Recall that the CDF for the standard normal distribution is given by

$$\Phi(x) = \frac{1}{\sqrt{2\pi}} \int_{-\infty}^{x} e^{-u^2/2} du = \frac{1}{2} \left[1 - \text{erf}\left(\frac{x}{\sqrt{2}} \right) \right] \, .$$

The inverse CDF for the standard normal distribution is then given by

$$\Phi^{-1}(u) = \sqrt{2} \, \text{erf}^{-1} \left(2u - 1 \right) \, .$$

The Beasley-Springer-Moro algorithm for approximating the inverse CDF for the standard normal distribution is used in the present work [54, 55]. This method pro-

vides a rational approximation for the inverse CDF on $[0.5, 0.92]$, and a Chebyshev approximation for the tails ($u > 0.92$). Note that the symmetry of the standard normal distribution allows an approximation for Φ^{-1} on $[0.5, 1)$ to be extended to $(0, 1)$:

$$\Phi^{-1}(u) = \Phi^{-1}(1 - u) \ .$$

This approximation has been found to have a maximum absolute error of 3×10^{-9} over seven standard deviations [55]. This approach is preferred over the Box-Muller transformation, which has the potential to upset the low-discrepancy structure of the sequence and lead to reduced efficiency [43, 56]. Figure 4.2 illustrates a two-dimensional standard normal distribution generated using pseudorandom and low-discrepancy sequences.

To sample from a multivariate normal distribution with mean $\boldsymbol{\mu}$ and covariance matrix $\boldsymbol{\Sigma}$, either a Cholesky decomposition or eigendecompostion of the covariance matrix can be used. Eigendecomposition of the covariance matrix yields a diagonal matrix $\mathbf{D}$ consisting of the non-negative eigenvalues of $\boldsymbol{\Sigma}$, and an orthogonal matrix $\mathbf{Q}$ whose columns are the unit eigenvectors of $\boldsymbol{\Sigma}$:

$$\boldsymbol{\Sigma} = \mathbf{Q}\mathbf{D}\mathbf{Q}^T \ .$$

The transformation from $\mathbf{Z} \sim \mathcal{N}(\mathbf{0}, \mathbf{1})$ to $\mathbf{X} \sim \mathcal{N}(\boldsymbol{\mu}, \boldsymbol{\Sigma})$ is then given by

$$\mathbf{X} = \boldsymbol{\mu} + \mathbf{Q}\mathbf{D}^{1/2}\mathbf{Z} \ .$$

The reader is referred to Niederreiter [41] for a comprehensive treatment of Monte Carlo and quasi-Monte Carlo methods, and to Devorye [53] for a complete treatise on random variate generation.
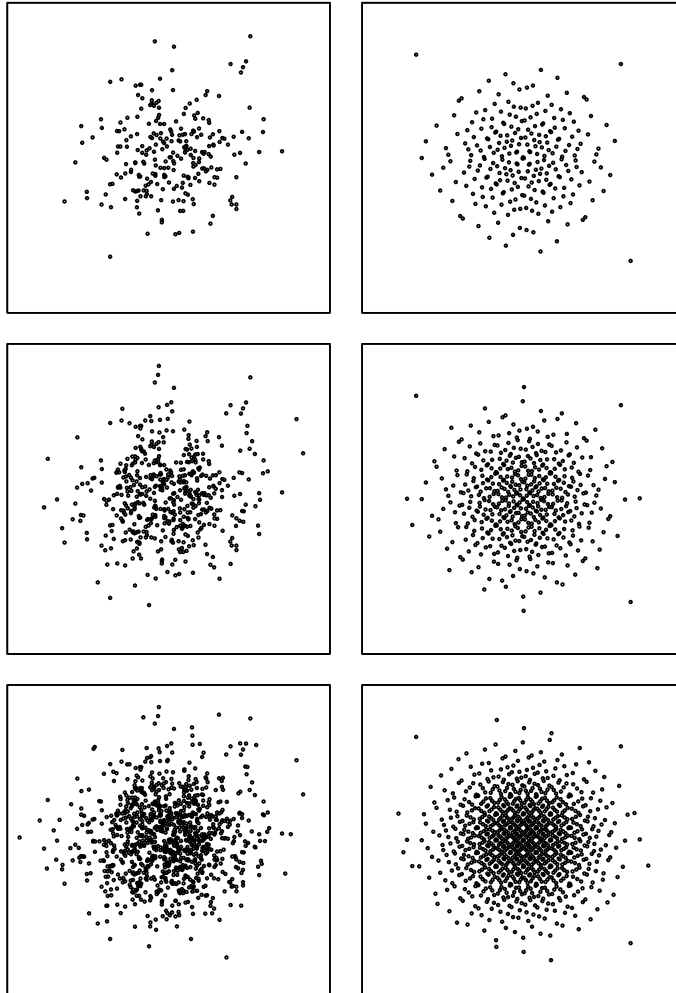
Figure 4.2: Two-dimensional standard normal distributions on $[-4, 4]^2$ generated using the pseudorandom (left) and Sobol (right) sequences of figure Fig. 4.1 transformed using the Beasley-Springer-Moro approximation for the inverse cumulative distribution function of the standard normal distribution.

Chapter 5

Improving the Efficiency of SCP

by Several Orders of Magnitude

The self-consistent phonons (SCP) method provides a consistent way to include anharmonic effects when treating a many-body quantum system at thermal equilibrium. The system is then described by an effective temperature-dependent harmonic Hamiltonian, which can be used to estimate the system's properties, such as its free energy or its vibrational spectrum. The numerical bottleneck in the solution of the SCP equations (Eqs. 3.17) is the evaluation of the expectation values of the potential energy and its derivatives over the multivariate normal distribution of the reference harmonic system. Supposing the physical potential energy surface (PES) includes only two-body terms, these integrals can be greatly simplified. Ref. 33 takes full advantage of this simplification to make the SCP method practical for very large systems, albeit considering only two limiting cases: the classical limit ($\hbar \to 0$) and zero-temperature limit ($T \to 0$). In Ref. 33 the method was applied to study the

competition between icosahedral and decahedral motifs in Lennard-Jones clusters consisting of thousands of atoms. Of course, the great improvements in the numerical efficiency of the SCP method that were possible for the Lennard-Jones systems cannot be extended easily to a general PES including many-body terms. Just one example of a many-body PES is the tight-binding semi-empirical PES used in Ref. 31, where in order to implement SCP the authors used a standard Monte Carlo (MC) method for evaluating the corresponding Gaussian integrals. Unfortunately, achieving sufficiently accurate values of the integrals required a large enough number of MC points to make the SCP approach look too expensive to be "practical", and even unfeasible were the PES to be computed by an *ab initio* method.

In this chapter and in Ref. 57, partly inspired by Ref. 31, we adapt the idea of evaluating the Gaussian integrals numerically, while introducing some ideas and numerical "tricks" which reduce the overall cost of the integration by several orders of magnitude, transforming SCP into a very efficient and general method, and even practical for the case of an *ab initio* PES. The most dramatic improvement comes form the use of quasi-Monte Carlo integration (see Chapter 4), whose integration error scales quasi-linearly with the number of quasirandom points used, in place of standard MC integration. In addition, we avoid direct calculation of the Hessian using some special relationships for Gaussian integrals, and discuss reducing the dimensionality of the integrals for potentials that can be decomposed as a sum of lower order, n-body (i.e., one-body, two-body, etc.) terms. We demonstrate the dramatically improved efficiency of the method by computing the vibrational frequencies of pyrene. Our results essentially reproduce those of Ref. 31, while demonstrating that the computational

cost is reduced by at least four orders of magnitude. Additional numerical examples demonstrating the versatility of the SCP method and feasibility of its application to molecules and clusters using *ab initio* PES's will be given in subsequent chapters.

5.1 Repertoire of numerical improvements

5.1.1 Quasi-Monte Carlo integration for expectation values

Should the Gaussian averages 3.14 be computed by the MC method, the following procedure can be utilized. Define a finite sequence $\mathbf{x}^{(s)} \in \mathbb{R}^{3N}, s = 1, ..., S$, distributed according to the multivariate standard normal distribution

$$P(\mathbf{x}) = (2\pi)^{-3N/2} e^{-\frac{1}{2}\mathbf{x}^{\mathrm{T}}\mathbf{x}} \ . \tag{5.1}$$

For a sufficiently smooth function $f(\mathbf{r})$, the Gaussian average 3.14 is then estimated by

$$\langle f(\mathbf{r}) \rangle_h \approx \frac{1}{S} \sum_{s=1}^{S} f(\mathbf{q} + \mathbf{M}^{-1/2}\tilde{\mathbf{D}}^{1/2}\mathbf{x}^{(s)}) \ . \tag{5.2}$$

In order to sample $P(\mathbf{X})$, the inverse cumulative distribution function (CDF) for the normal distribution can be used to transform any sequence uniformly distributed on $[0,1]^d$. As discussed in the previous chapter, the performance of standard MC integration using random (or pseudorandom) sequences is limited by the clustering of points and the presence of holes over the domain of integration. Quasi-MC, by contrast, uses deterministic low-discrepancy sequences whose points are correlated so as to prevent clustering and provide better uniformity over the domain of integration. Sobol sequences have shown superior performance in comparison studies of several

well-known low-discrepancy sequences [43,49], and as such, we have made use of Sobol

sequences in particular for all SCP calculations which rely on quasi-MC integration.

For a d-dimensional integral, quasi-MC integration achieves a convergence rate of

$O((\log S)^d S^{-1})$, although empirical results have found convergence rates of $O(S^{-1})$

for certain types of integrands [40]. The behavior of the two types of sequences is

illustrated in Fig. 4.1. Figure 4.2 compares two-dimensional standard normal distri-

butions generated using pseudorandom and Sobol sequences.

5.1.2 Avoiding direct calculation of the Hessian

When the PES is not given in a form suitable for analytic evaluation of the Gaussian

integrals defined in Eq. 3.14, they have to be evaluated numerically. Specifically, we

need to evaluate the average energy $\langle V \rangle_h$, gradient, $\langle \nabla V \rangle_h$, and Hessian $\langle \nabla \nabla^{\mathrm{T}} V \rangle_h$.

Considering the high-dimensionality of the integrals, and the desire to sample the

Gaussian distribution directly, MC integration is clearly preferable to other quadra-

ture schemes (e.g., Gauss-Hermite quadrature) which scale unfavorably with the di-

mensionality of the system. The specifics of the MC procedure will depend on whether

an analytic gradient and/or Hessian of the PES is/are available. If neither is avail-

able, evaluating them by finite differences for a system of N particles would increase

the computational cost by a factor of $3N$ for the gradient, and $(3N)^2$ for the Hessian.

In order to avoid this computational burden, the following relationships for Gaussian

integrals can be utilized, in which the Gaussian averaged derivatives are expressed in

terms of Gaussian averaged quantities involving lower-order derivatives:

$$\langle \nabla V(\mathbf{r}) \rangle_h = D^{-1} \left\langle (\mathbf{r} - \mathbf{q}) V(\mathbf{r}) \right\rangle_h \tag{5.3a}$$

$$\left\langle \nabla \nabla^{\mathrm{T}} V(\mathbf{r}) \right\rangle_h = \mathbf{D}^{-1} \left\langle (\mathbf{r} - \mathbf{q})^{\mathrm{T}} \nabla V(\mathbf{r}) \right\rangle_h \tag{5.3b}$$

$$= \mathbf{D}^{-1} \left\langle (\mathbf{r} - \mathbf{q})(\mathbf{r} - \mathbf{q})^{\mathrm{T}} V(\mathbf{r}) \right\rangle_h \mathbf{D}^{-1} - \langle V(\mathbf{r}) \rangle_h \mathbf{D}^{-1} . \tag{5.3c}$$

Note that in most electronic structure packages the gradient of the PES is computed directly for essentially the same cost as computing the potential energy itself, a reflection of the Hellman-Feynman theorem. However, even when the Hessian is computed directly, its evaluation is still costly, scaling usually as about N times a single energy evaluation. For this most common case we propose to avoid explicit evaluation of the Hessian with the help of Eq. 5.3b. That is, at each iteration, given $\mathbf{q}$ and $\mathbf{D}$, we want to construct the mass-scaled effective Hessian using

$$\tilde{\mathbf{K}} = \tilde{\mathbf{D}}^{-1} \mathbf{M}^{1/2} \left\langle (\mathbf{r} - \mathbf{q})^{\mathrm{T}} \nabla V(\mathbf{r}) \right\rangle_h \mathbf{M}^{-1/2} , \tag{5.4}$$

where for convenience we have also introduced the mass-scaled covariance matrix

$$\tilde{\mathbf{D}} := \mathbf{M}^{1/2} \mathbf{D} \mathbf{M}^{1/2} . \tag{5.5}$$

5.1.3   Gaussian averages in a small subspace

Consider the evaluation of the expectation value of a function $f(\mathbf{y}) : \mathbb{R}^L \to \mathbb{R}$ with respect to a $3N$-dimensional Gaussian distribution,

$$\langle f(\mathbf{y}) \rangle = \frac{\int f(\mathbf{y}) \exp\left(-\mathbf{r}^T \mathbf{C}\, \mathbf{r}\right) d^{3N} \mathbf{r}}{\int \exp\left(-\mathbf{r}^T \mathbf{C}\, \mathbf{r}\right) d^{3N} \mathbf{r}} , \tag{5.6}$$

where $\mathbf{r} = (\mathbf{y}^{\mathrm{T}}, \mathbf{x}^{\mathrm{T}})^{\mathrm{T}}$, $\mathbf{y} \in \mathbb{R}^L$, $\mathbf{x} \in \mathbb{R}^{3N-L}$, $\mathbf{C} \in \mathbb{R}^{3N \times 3N}$, and $L < 3N$. Let

$$\mathbf{C} = \begin{pmatrix} \mathbf{A} & \mathbf{E} \\ \mathbf{E}^T & \mathbf{B} \end{pmatrix} \tag{5.7}$$

where $\mathbf{A} \in \mathbb{R}^{L \times L}$, $\mathbf{B} \in \mathbb{R}^{(3N-L) \times (3N-L)}$, and $\mathbf{E} \in \mathbb{R}^{L \times (3N-L)}$. Then the $3N$-dimensional Gaussian average above is reduced to the L-dimensional Gaussian average:

$$\langle f(\mathbf{y}) \rangle = \frac{\int f(\mathbf{y}) \exp\left[-\mathbf{y}^T (\mathbf{A} - \mathbf{E}\mathbf{B}^{-1}\mathbf{E}^T) \, \mathbf{y}\right] d^L\mathbf{y}}{\int \exp\left[-\mathbf{y}^T (\mathbf{A} - \mathbf{E}\mathbf{B}^{-1}\mathbf{E}^T) \, \mathbf{y}\right] d^L\mathbf{y}} . \tag{5.8}$$

For potentials $V(\mathbf{r})$ that can be decomposed into low-order terms, the above formula would reduce the integration space from $3N$ to L, where $L = 6$ for two-body terms, $L = 9$ for three-body terms, etc. While we have not made use of this approach in any of the work presented in this thesis, instead opting to keep our implementation of SCP in its most general form, there are a number of potentials for which this approach could be expected to result in a significant reduction in the computational cost. As will be seen, our implementation of SCP is already quite numerically efficient, even without exploiting this particular "trick".

5.1.4 Using a reference potential to accelerate numerical integration

Consider a Gaussian average (Eq. 3.14), e.g., the average potential $\langle V(\mathbf{r}) \rangle$. Here we assume that a single potential energy evaluation is expensive, examples of which are not hard to find. Suppose a reference PES $V_{\mathrm{ref}}(\mathbf{r})$ is available, which is a relatively good approximation to $V(\mathbf{r})$ and which is cheap to evaluate. The approximation does

not actually have to be very accurate, but should at least approximate well the rapidly changing terms of $V(\mathbf{r})$, the very terms that determine the convergence rate of the numerical integration. By assumption, the average $\langle V_{\text{ref}}(\mathbf{r}) \rangle$ is cheap to evaluate and can be estimated separately and very accurately. Consequently, we write

$$\langle V(\mathbf{r}) \rangle = \langle V_{\text{ref}}(\mathbf{r}) \rangle + \langle \Delta V(\mathbf{r}) \rangle , \qquad (5.9)$$

where the difference potential $\Delta V(\mathbf{r}) = V(\mathbf{r}) - V_{\text{ref}}(\mathbf{r})$ is by assumption a small and/or slowly varying function of $\mathbf{r}$. Therefore, its average will converge much faster with respect to the size of the point set used for numerical integration. Although based on a trivial observation, this trick may lead to an enormous numerical saving.

In addition, for the special case where the PES is given by

$$V(\mathbf{r}) \approx \sum_{i>j} V_{ij}(|r_i - r_j|) + \text{higher-order terms}, \qquad (5.10)$$

the Gaussian averages of the two-body terms $V_{ij}(|r_i - r_j|)$ can be evaluated analytically once each such term is approximated by a sum of Gaussians (see, e.g., Ref. 33).

5.2   Numerical demonstrations

5.2.1   Fundamental frequencies of pyrene

In this section we demonstrate the improved efficiency of the SCP method by re-producing one of the results from Ref. 31, specifically, the central panel of Figure 5, which reports the SCP eigenfrequencies of the C-H stretch vibrational band of pyrene, $C_{16}H_{10}$, at $T = 0\,\text{K}$. The molecule is represented by the semiempirical tight-binding

PES of Van Oanh *et al.* [58]. Fortunately, the "Newton-Raphson" iterative scheme (Eq. 3.30) is stable for this system, requiring only about 10 iterations to converge all of the fundamental frequencies [31]. However, at each iteration Ref. 31 uses a standard Metropolis MC to evaluate the Gaussian averages of the potential, the force, and the Hessian. All three averages are computed explicitly. For this calculation, $(3N-6) \times 10^6 = 7.2 \times 10^7$ evaluations of the Hessian were performed at each iteration, which roughly translates (assuming a general case) to $3N(3N-6) \times 10^6 \approx 5.6 \times 10^9$ single gradient evaluations per iteration, thus making the implementation of even a single iteration quite costly. Our results are shown in Fig. 5.1. As in Ref. 31, the Newton-Raphson iteration in $\mathbf{q}$ starts from the classical energy minimum and $\mathbf{K}$ is initialized with the corresponding classical Hessian (iteration number 0). Ten iterations were performed utilizing the same sequence of $S = 5 \times 10^4$ Sobol points at each step. The resulting frequencies are converged with respect to the number of iterations, but they are not quite converged with respect to S. Even so, their pattern is strikingly similar to that in Figure 5 of Ref. 31. At iteration number 11, the calculation was continued using $S = 2 \times 10^5$ points per iteration. As seen in the figure, after a rough convergence using $S = 5 \times 10^4$ is achieved, a single iteration with $S = 2 \times 10^5$ is sufficient to refine the computed frequencies. The following portion of the calculation (iterations 16 through 20) used $S = 5 \times 10^5$, resulting in a slight further refinement of the frequencies. Once again, it appears that a single additional iteration using a longer Sobol sequence would have been sufficient to achieve this refinement. We also found that in order to achieve rough convergence, a Sobol sequence as short as $S = 10^4$ suffices. Following this with a single iteration with large enough S gives

converged frequencies. Note also that since in our case the explicit use of Hessians was avoided, the cost of a single iteration is S single gradient evaluations. This is to be compared with effectively 5.6×10^9 single gradient evaluations per iteration in Ref. 31. Although results are shown only for pyrene at $T = 0\,\text{K}$, very similar results were also produced for a wide range of finite temperatures ($0 < T < 1000\,\text{K}$), and for similar polycyclic aromatic hydrocarbon molecules (naphthalene, $C_{10}H_8$, and coronene, $C_{24}H_{12}$) using the same semi-empirical tight-binding PES.

5.2.2 Free energies and vibrational frequencies of water hexamer

In this section we present SCP results for the free energies and vibrational frequencies of water hexamer for the purpose of 1) demonstrating the newfound utility/practicality and versatility/generality of the method, and its potential to be used with more expensive/accurate PESs, 2) providing a more detailed account of the protocol for the method, and 3) providing a particular example in which the use of a reference potential could be used to further reduce the cost of the SCP calculation.

Water hexamer has received considerable attention in the past, both experimentally and theoretically [59–67], with the most recent publications indicating that this interest will not be subsiding anytime soon [68–75]. The primary reason is that six is the smallest number of water molecules that can arrange themselves in stable three-dimensional structures. One puzzling question has been: what is the equilibrium population ratio of these structures as a function of temperature? Most of the exper-
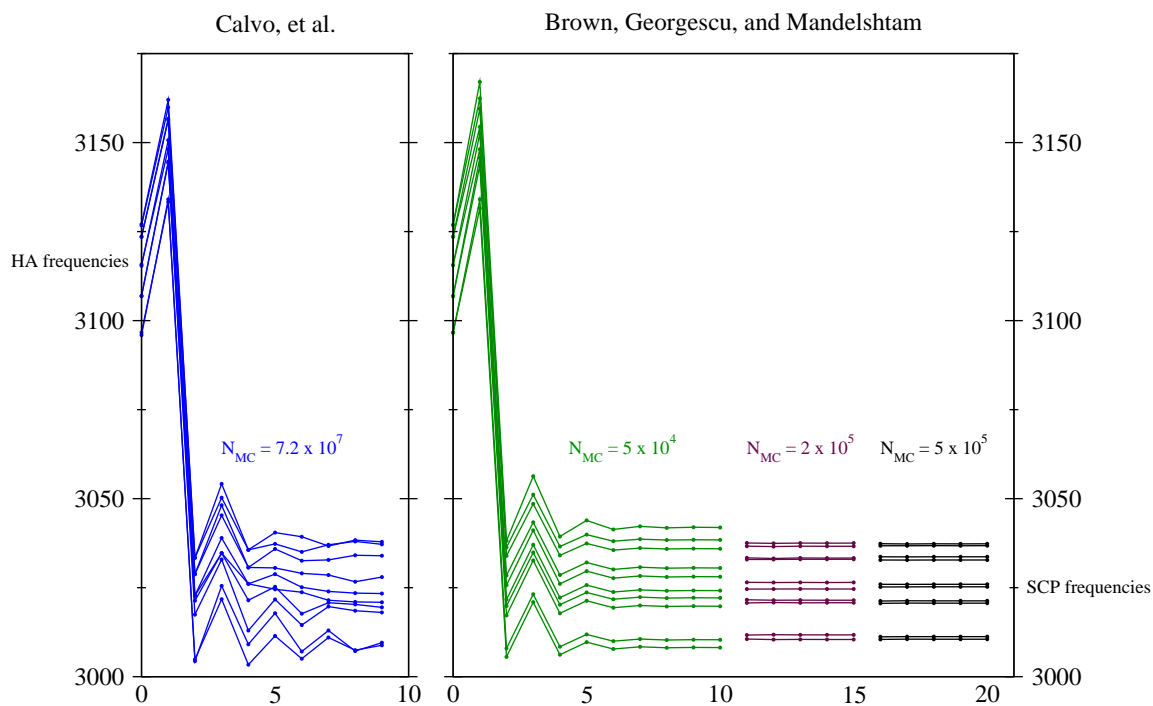
Figure 5.1: Convergence behavior of vibrational frequencies of pyrene at $T = 0\,\mathrm{K}$, computed using the SCP method, showing the C-H stretch vibrational band. Different colors correspond to different numbers (N_{MC}) of points in the Sobol sequence used to compute the Gaussian integrals. The frequencies in the left panel were digitally extracted from the central panel of Fig.5 from Ref. 31.

imental and theoretical evidence suggests that the "prism" isomer and "cage" isomer are likely candidates for being thermodynamically most stable; comparable populations of these two isomers are observed, even at very low temperatures, with perhaps a slight preference toward the prism isomer.

The experimental structural assignments depend on theory, while the theoretical analysis is complicated by the fact that the competition between different structures is sensitive to the fine features of the potential energy surface (PES), with many different PES's available, and, until very recently [76–78], no overwhelming evidence for any particular PES being the most accurate. Another well-recognized complication is that the thermodynamics, dynamics, and structural properties of water, and specifically water clusters, depend strongly on quantum effects. Correctly taking quantum effects into account can hardly be done using an empirical PES, while the use of a truly *ab initio* PES is very costly for most quantum dynamics approaches due to the need for a large number of energy evaluations. At the time during which this work was carried out, the WHBB water potential of Bowman and coworkers [68, 69], which is a high quality fit based on *ab initio* data appeared to provide the a reasonable compromise, and was consequently adapted for this particular application of SCP.

Previously reported results include diffusion Monte Carlo (DMC) and path integral Monte Carlo (PIMC) calculations treating water hexamer quantum mechanically using the WHBB PES [71]. Although the prism conformation is the classical global energy minimum of the WHBB PES, DMC predicts the ground state energy of the prism and the cage to be equal within the error bar of the DMC energy estimate. A rough extrapolation of the available PIMC data to low temperatures is in agreement

with the DMC prediction, although the convergence of the parallel tempering PIMC may be questioned, and it cannot provide data at very low temperatures. Additionally, a recent assessment [73] of the DMC method focusing on water clusters using the q-TIP4P/F PES [79] may cast doubt on the reliability of the DMC results.

Although WHBB is a parametrized PES, its evaluation is by orders of magnitude more costly than empirical water PES's, such as the q-TIP4P/F PES. This makes simulations of water clusters using the WHBB PES very expensive. For example, the above mentioned parallel tempering PIMC calculations of Ref. 71 required substantial supercomputer resources. As such, the WHBB water model provides a good challenge for this improved implementation of SCP.

Since the two mentioned water PES's are qualitatively not much different, it was possible to carry out all of the preliminary convergence tests using the much less expensive q-TIP4P/F PES. These tests showed that the unmodified "Newton-Raphson" iterative scheme (using Eq. 3.30c) for water is unstable, while Eq. 3.39c is stable for a sufficiently small value of τ, that is, water turned out to be a much more challenging system for the SCP method than the aromatic hydrocarbon molecules. We also tested the convergence with respect to the number of iterations and the number S of Sobol points. We found that a reasonably high accuracy, ~ 0.03 kcal mol^{-1}, for the free energy is achieved using $S = 1 \times 10^4$, while $S = 5 \times 10^4$ provides accuracy better than ~ 0.01 kcal mol^{-1}. We also found empirically that $\tau \approx 50$ corresponds to a nearly optimal choice.

A possible iteration schedule is as follows. The calculation starts at $T = 0\,\mathrm{K}$, initializing $\mathbf{q}$ with the configuration at the corresponding energy minimum and ini-

tializing **K** using the Hessian at the minimum. Some of the high frequencies converge with only a few iterations, but since the convergence of the free energy requires *all* frequencies to be well-converged, we found it necessary to perform between 20 to 50 iterations with Eq. 3.39c. Note that just as in the case of hydrocarbons, this preliminary run can be performed using much fewer Sobol numbers, e.g. $S = 5 \times 10^3$. Then not more than three iterations with $S = 5 \times 10^4$ give converged results for both the frequencies and the free energy. The temperature is then increased in small increments, $T \to T + \Delta T$, with the values of **q** and **K** obtained at the lower temperature carried over to initialize the iterative procedure at higher temperature. We found $\Delta T = 5\,\mathrm{K}$ to be a good choice, so that at each particular temperature only about three iterations with $S = 5 \times 10^4$ appeared sufficient.

The above iteration schedule was then used with the WHBB PES. Note, however, that the Gaussian averages of the WHBB PES could also be computed in a decomposed manner as shown in Eq. 5.9, with the q-TIP4P/F PES as a reference.

The free energy differences for five hexamer structures — prism, cage, book, prism-book, and double-tetramer — are shown in Fig. 5.2. The prism isomer has the lowest free energy at all temperatures in the range $T < 200\,\mathrm{K}$ and is used as a reference, with $F(\text{cage}) - F(\text{prism}) \sim 0.2\,\mathrm{kcal\,mol^{-1}}$. Fig. 5.2 also shows the free energies estimated by the harmonic approximation, which predicts $F(\text{cage}) - F(\text{prism}) \sim 0.1\,\mathrm{kcal\,mol^{-1}}$ at $T = 0\,\mathrm{K}$, with the cage isomer eventually becoming thermodynamically more stable at temperatures greater than $T \sim 120\,\mathrm{K}$. The $k_\mathrm{B}T$ scale shown in the figures indicates that regardless of which of the two structures has the lowest free energy, both isomers should have a detectable population at temperatures $T \sim 10\,\mathrm{K}$.
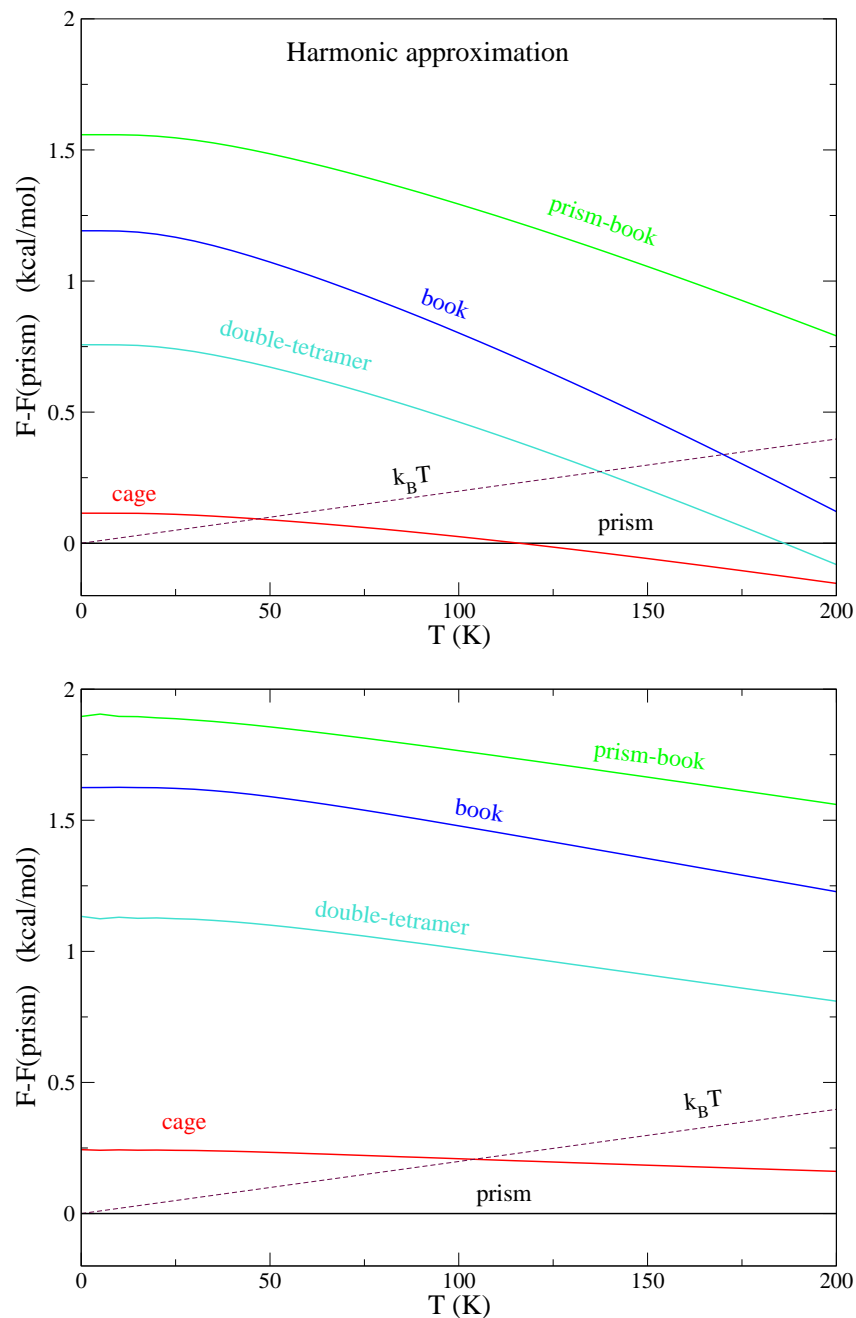
Figure 5.2: Free energies of several low-lying isomers of water hexamer relative to that of the prism isomer, estimated by the harmonic approximation (upper panel) and the self-consistent phonons (SCP) approximation (lower panel). The SCP method predicts the prism isomer always being slightly thermodynamically preferable to the cage isomer.

In Table 5.1 we list the 18 intramolecular frequencies for the water hexamer prism isomer estimated with the SCP method at two different temperatures ($T = 0\,\mathrm{K}$ and $T = 100\,\mathrm{K}$). Note that while the frequency shifts caused by the anharmonicities are substantial ($\sim 100\ \mathrm{cm}^{-1}$), the frequency shifts caused by thermal fluctuations are minuscule ($\sim 1\ \mathrm{cm}^{-1}$). Also shown are the results by Wang and Bowman [69] computed using the local monomer model (LMM). The latter is an approximation based on representing each water monomer, coupled to the remaining $3N - 3$ modes, with an effective three-dimensional Hamiltonian. The accuracy of LMM is assessed for the case of water dimer [80], which is very small for the bend frequencies, but is $\sim 50\ \mathrm{cm}^{-1}$ for one of the O-H stretch frequencies. In addition, less reliable error estimates for the water dimer can be found in Ref. 69. Unfortunately, at this point we cannot assess the accuracy of the SCP method using an independent test.

The data from Table 5.1 is also shown in Fig. 5.3. One can notice a qualitative agreement between SCP and LMM in that they predict the same trend in the behavior of the intramolecular frequencies caused by anharmonic effects. However, a more detailed inspection of this data shows that while for the six bend frequencies the disagreement between SCP and LMM is of the order of 20 cm^{-1}, for the O-H stretch frequencies the disagreement ranges from ~ 50 cm^{-1} to ~ 200 cm^{-1}. Interestingly, the LMM anharmonic shift is about the same for all O-H stretch modes (~ 200 cm^{-1}) except for one (OH-1), while the SCP anharmonic shift correlates with the value of the mode frequency. The nature of this disagreement is unclear, as the exact results are unknown, while the two approximations (SCP and LMM) rely on quite different assumptions.
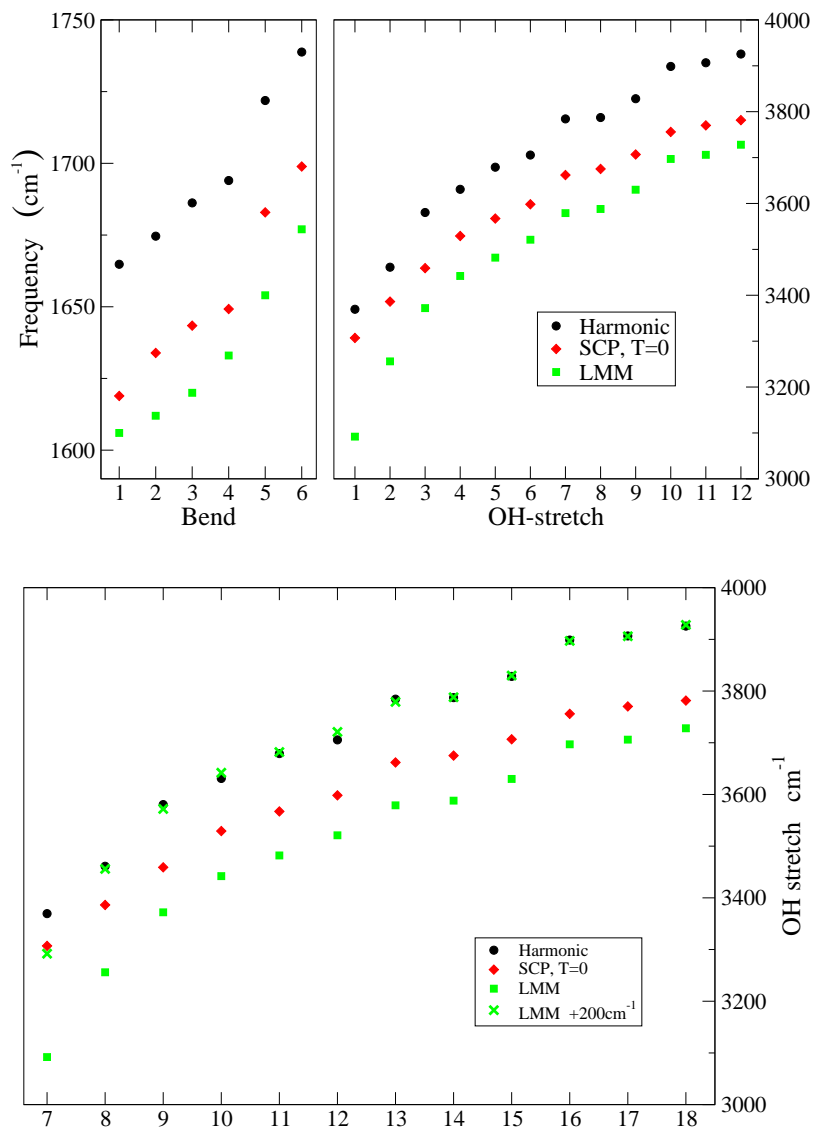
Figure 5.3: Stretching and bending frequencies for the prism isomer of water hex-amer for the WHBB potential energy surface, computed using the standard harmonic approximation, the self-consistent phonons (SCP) method, and the local monomer method (LMM) [69].

Table 5.1: Fundamental frequencies (cm^{-1}) of the intramolecular modes of the water hexamer prism isomer obtained by the harmonic approximation and the self-consistent phonons (SCP) method at two different temperatures.

Mode	Harmonic	SCP, $T = 0\,\text{K}$	SCP, $T = 100\,\text{K}$
1	1664.8	1618.9	1618.9
2	1674.6	1633.9	1633.7
3	1686.2	1643.4	1643.3
4	1694.0	1649.2	1648.0
5	1721.9	1682.9	1681.7
6	1738.8	1698.9	1697.4
7	3369.5	3307.0	3313.9
8	3461.1	3386.2	3393.3
9	3580.4	3459.1	3462.0
10	3630.9	3529.2	3530.4
11	3679.0	3567.2	3568.7
12	3705.5	3598.3	3599.2
13	3784.3	3661.9	3663.1
14	3787.3	3675.2	3676.7
15	3828.3	3706.7	3707.7
16	3898.6	3755.9	3756.0
17	3906.6	3770.2	3770.7
18	3925.6	3781.6	3781.5

To conclude this section, we note that in our preliminary numerical tests using the cheap q-TIP4P/F PES (not reported), we considered clusters containing as many as 200 water molecules and were able to produce converged results for most vibrational modes still using relatively short Sobol sequences (e.g. $S \sim 10^6$). However, due to the presence of a large number of low-frequency modes in such a system, implementation of the self-consistent iterative procedure requires special care. Moreover, even when self-consistency is maintained, the low-frequency portion of the computed spectrum, being harmonic by construction, should probably not be trusted. In Chapter 7 we consider the use of SCP for the purpose of computing free energy differences in greater detail, and in particular, the challenges posed by the low-frequency, large-amplitude modes.

5.3   Closing remarks

In this chapter we introduced several algorithmic improvements to the SCP method to make it practical for describing equilibrium properties of relatively large molecular or atomic quantum systems. This remarkably efficient numerical implementation is general enough that it can be used even with an *ab initio* PES (see Chapters 7 and 8), and as such, could replace the standard normal mode analysis routinely implemented in most electronic structure packages. It is important to note that even though anharmonic corrections are included, the method does not require explicit use of analytic Hessians or calculation of higher-order derivative tensors of the PES.

Chapter 6

Assessing the Accuracy of SCP:

Structural Properties of

Lennard-Jones Clusters

The inherently approximate nature of the self-consistent phonons (SCP) method makes an assessment of its accuracy a critically important issue, yet, an explicit and compelling assessment of its accuracy has been lacking in spite of the fact that SCP's inception took place decades ago. To this end, we undertook an assessment of the accuracy of the method and its advantages over the standard harmonic approximation (HA) for computing structural properties of classical Lennard-Jones (LJ) clusters. Here we apply SCP to classical LJ clusters and compare with numerically exact results. The close agreement between the two reveals that SCP accurately describes structural properties of the classical LJ clusters from zero-temperature (where the

method is exact) up to the temperatures at which the chosen cluster conformation becomes unstable. Given the similarities between thermal and quantum fluctuations, both physically and within the SCP ansatz, the accuracy of classical SCP over a range of temperatures suggests that quantum SCP is also accurate over a range of quantum de Boer parameter, $\Lambda = \hbar/(\sigma\sqrt{m\varepsilon})$, which describes the degree of quantum-character of the system. As one would expect, results obtained using HA show appreciable quantitative disagreement, and even qualitatively incorrect behavior.

In Chapter 5 and Ref. 57 we reported SCP fundamental frequencies for OH stretching and HOH bending modes in water hexamer, which did show the physically correct trends in terms of the anharmonic contributions. At the same time, the SCP results were in significant quantitative and qualitative disagreement with the results of Wang and Bowman using the local monomer model (LMM) [69]. Unfortunately, currently no method exists that could reliably predict such quantities for a system as complex as quantum water hexamer, making the assessment of the accuracy of a quantum dynamics method applied to a general many-body system a critical issue. As is the case with most other quantum many-body approaches, the SCP approximation is uncontrollable in the sense that there is generally no consistent procedure to systematically improve its accuracy by a gradual increase of the computational effort. That is, in order to go beyond the SCP approximation one needs to make a heroic effort. (See Refs. 28 and 81 for examples of such extensions.)

Incidentally, some evidence of the accuracy of the method has already been established. As discussed in Ref. 81, SCP is equivalent to the variational Gaussian wavepacket (VGW) method [21, 82] in the $T \to 0$ limit. Ref. 83 demonstrated very

good agreement between VGW ground state energies of several isomers of Ne_{38} with those obtained from low-temperature path integral Monte Carlo (PIMC) calculations. In addition, Ref. 82 demonstrated agreement between VGW and PIMC at very low temperature for the pair correlation function of Ne_{13}.

In this chapter we carry out an assessment of the accuracy of SCP for the calculation of equilibrium structural properties for a classical system at finite temperatures. In particular, we consider the radial distribution function and principal moments of inertia for LJ clusters. Computed equilibrium structures are clearly of great interest and utility in their own right. Additionally, the accurate determination of these structural properties makes possible the comparison between theoretical and experimental results. The link between the radial distribution function and the structure factor determined in scattering experiments, and between the principal moments of inertia and rotational spectra makes it possible to combine theoretical and experimental avenues of inquiry. Considering the analogous treatment of quantum fluctuations and thermal fluctuations in the SCP framework, the accuracy of the method for a classical system over a given range of temperatures suggests that it should also be accurate for systems which do not exhibit too much quantum character. As will be discussed, it should be considered one of the key advantages of the SCP method over other approaches that its implementation is virtually the same for both classical and quantum systems.

LJ clusters have long been a popular system for testing sampling and optimization algorithms/methods, and for studying fundamental physical phenomena. The LJ pair

potential is given by

$$V(\mathbf{r}) = 4\varepsilon \left[\left(\frac{\sigma}{r} \right)^{12} - \left(\frac{\sigma}{r} \right)^{6} \right] ,$$

where the energy scale and the length scale are defined by the LJ parameters, i.e., the well-depth, ε, and the interparticle distance at which the potential is zero, σ. As we have seen in Chapter 2, for systems governed by this potential, the degree of quantum delocalization can be conveniently described by the quantum de Boer parameter,

$$\Lambda := \hbar/(\sigma\sqrt{m\varepsilon}) .$$

Note that $\Lambda = 0$ corresponds to a classical system, and $\Lambda \approx 0.095$ to neon. Though governed by a simple potential, LJ clusters exhibit rich behavior and properties, which are by now very well understood. The comprehensive body of theoretical work for these clusters includes studies of their potential energy landscapes, and phase/structural transitions induced by changes in size, temperature, or quantum parameter. (See, e.g., Refs. 35, 84–92, and references therein.) Their use in the present work enables us to reliably demonstrate the accuracy of the SCP method, without risking the introduction of unnecessary complications arising from any poorly understood or pathological behavior of the potential or system used. Moreover, the de Boer parameter provides the desired well-defined and quantifiable degree of quantum character for this potential.

In contrast to methods such as replica-exchange Monte Carlo or molecular dynamics (or their path integral variations) in which many minima are sampled, both the standard HA and SCP break down once the simulation leaves the basin of attraction. For this reason, comparisons of equilibrium thermodynamic quantities obtained using

these two different types of methods are generally not meaningful at temperatures where multiple isomers or minima contribute. With this in mind, we have chosen for the sake of simplicity to consider the minimum energy isomers of the LJ_{13}, LJ_{38}, and LJ_{55} clusters, as all three exhibit "deep" global minima separated from other (local) minima by large barriers. Here we assess the accuracy of SCP for a classical system at finite temperature by comparing to Markov chain Monte Carlo (MC) using the well-known Metropolis-Hastings algorithm. This method is exact in the sense that the computed ensemble averages are guaranteed to converge to the true values for a long-enough simulation, and is also exceptionally simple to implement, even in the present case where we wish to sample only a particular minimum of the PES.

6.1   Methods

Recall from Chapter 5 that the Hessian, $\nabla\nabla^{\mathrm{T}}V$, does not need to be computed explicitly in the SCP ansatz, as a consequence of working with Gaussian integrals. Instead, we may consider the average product of the displacement and the gradient,

$$\langle\nabla\nabla^{T}V(\mathbf{r})\rangle_{h} = \mathbf{D}^{-1}\langle(\mathbf{r}-\mathbf{q})^{T}\nabla V(\mathbf{r})\rangle \ . \tag{6.1}$$

This property circumvents the enormous expense associated with computing an analytic Hessian, supposing it is even available, or a finite-difference Hessian when it is not. While this "trick" generally comes at the price of working with an integrand which is more oscillatory, and hence an integral which converges more slowly, the overall reduction in computational cost is still substantial, especially when using more complex or *ab initio* potentials.

The simple form of the LJ potential and its low computational cost afford us the freedom to choose any of the three variations mentioned, i.e., exploit Eq. 6.1 and avoid computing the Hessian altogether, compute a finite-difference Hessian, or compute the analytic Hessian. The results presented in this chapter were obtained from SCP simulations which made use of the analytic Hessian. (All three variations were implemented in preliminary simulations and produced identical results.) Earlier work [33] using SCP to study thermal and quantum transitions in large LJ clusters ($N \sim 10^4$) made use of the ability to fit the LJ pair-potential by a sum of Gaussians [93]. However, the improved efficiency of the SCP method with the incorporation of quasi-Monte Carlo integration [57] and comparatively modest cluster sizes examined here preclude the need for such fitting of the potential.

One of the distinct features of SCP is that its implementation is virtually the same for classical and quantum systems, with no additional overhead required for the quantum case. Ref. 33 considers two important limits of SCP: the zero-temperature ($T = 0$) limit, and the classical ($\Lambda = 0$) limit, and shows that the SCP equations in each limit can be formulated in terms of the solution of a system of ordinary differential equations along a fictitious time, with the two systems having remarkably similar structure. (For the quantum case in the zero-temperature limit, SCP turns out to be equivalent to the variational Gaussian wavepacket (VGW) approximation [21,82]; in both cases the quantum ground state constrained to a local potential energy minimum is approximated by the same variational Gaussian.) This resemblance of the classical ($\Lambda = 0$, $T > 0$) and quantum ($T = 0$, $\Lambda > 0$) limits seems to offer the possibility of establishing an almost quantitative relationship between the quantum

parameter Λ and temperature T. In the present context, this relationship will be used as an argument to justify the use of the SCP method for the quantum case over a range of quantum parameters Λ based on its favorable assessment in the classical limit over a range of temperatures.

6.2 Pair correlation functions and principal moments of inertia

HA, SCP, and MC calculations were carried out beginning from the minimum energy configurations obtained from the Cambridge Cluster Database [94]. SCP simulations for the classical LJ_{13}, LJ_{38}, and LJ_{55} clusters typically used 20 iterations at each temperature. Between 20 and 100 iterations were carried out at each value of Λ for the quantum LJ_{13}, LJ_{38}, and LJ_{55} clusters. For the Ne_{13}, Ne_{38}, and Ne_{55} clusters, 100 iterations were carried out at each temperature. At each iteration, $S = 2^{15}$ Sobol points were used to compute the average potential, gradient, and Hessian with respect to the reference harmonic system. Based on preliminary SCP calculations employing Sobol sequences of various lengths, this value of S was chosen to exclude any ambiguity associated with the numerical accuracy of computed integrals. On the final iteration for each temperature T or quantum parameter Λ, the 2^{15} Sobol points were used to average the radial distribution function and principal moments of inertia. In order to maintain a fair comparison of the methods, for the case of HA the structural properties were computed using the same protocol as that for SCP with

the only difference being the different harmonic Hamiltonians used to compute the averages.

MC simulations were carried out from low temperature ($0.001\ \varepsilon/k_{\mathrm{B}}$) up to roughly the temperatures at which the random walk would become unstable (i.e., would escape from the potential energy minimum in which it was initialized) with temperature increments of either $0.001\ \varepsilon/k_{\mathrm{B}}$ or $0.010\ \varepsilon/k_{\mathrm{B}}$, and 10^8 trial MC moves completed at each temperature. (Each trial MC move is an attempt to displace a single particle in the Metropolis algorithm.) Hard constraining radii of 2.0σ, 3.0σ, and 3.5σ (with respect to the center of mass) were used for LJ_{13}, LJ_{38}, and LJ_{55}, respectively.

The radial pair correlation functions $p(r/\sigma)$ for classical LJ_n clusters ($n = 13$, 38, 55) computed by three methods (HA, SCP, and MC) are shown in Figs. 6.1 through 6.3. At low temperature ($T = 0.056\,\varepsilon/k_{\mathrm{B}}$) HA, SCP, and MC all agree well with one another, as one would expect. However, close inspection of individual peaks and troughs in the pair correlation functions reveals that even at this low temperature, HA already deviates slightly from the exact MC result, while SCP very faithfully adheres to it. The deviations among the three results become more noticeable as the temperature increases, still, SCP consistently produces the correct r/σ values for the peak centroids (i.e., the mass centers) of the pair correlation functions for all three clusters considered.

Not only is HA quantitatively inaccurate, it is also intrinsically unable to produce much of the qualitatively correct physical behavior of the clusters. For example, due to the center of the harmonic potential being fixed at the minimum in HA, the peaks in the radial distribution function are unable to shift with increasing temperature or

de Boer parameter. By contrast, in the SCP approximation the center and width of the effective harmonic potential are temperature- and quantum parameter-dependent, so that the peaks in the distribution function expand outward with increasing temperature and/or quantum parameter, as they should. This striking difference between the two approximations is clearly illustrated in Fig. 6.4, which shows the evolution of the LJ_{13} radial distribution function with temperature. Similarly, Fig. 6.5 shows the evolution of the radial distribution function with Λ for the ground states $(T = 0)$ of LJ_{13}, LJ_{38}, and LJ_{55}. This result is another demonstration of the SCP approximation being able to correctly account for anharmonic effects corresponding to cluster expansion caused by quantum fluctuations.

As previously mentioned, Ref. 82 reports a comparison of presumably exact path integral Monte Carlo (PIMC) results [95] for the radial pair correlation functions of Ne_{13} with those computed by VGW. Fig. 6.6 here shows a similar comparison of PIMC with SCP at low temperature $(T = 2\,\mathrm{K}$, or $T = 0.056\,\varepsilon/k_{\mathrm{B}}$ in reduced units). Though SCP and VGW are algorithmically very different, at this temperature they yield nearly the same result, which also agrees well with PIMC. Again, the standard HA does not account for cluster expansion due to the quantum fluctuations, which is manifested in the peaks of $p(r)$ maintaining significantly lower values compared to the exact result.

Finally, Fig. 6.7 shows the dependence of the principal moments of inertia of the same three clusters on either temperature or de Boer parameter. Again, three special cases are considered, corresponding to the classical $(\Lambda = 0)$ LJ clusters (left column), quantum ground states $(T = 0)$ of the quantum LJ clusters (center column), and

70

neon ($\Lambda = 0.095$) (right column). Notably, the moments of inertia for the classical clusters computed by SCP not only display the physically correct behavior, but are also in a very good quantitative agreement with the numerically exact MC results up to relatively high temperatures. This is in contrast with the HA approximation, which shows physically incorrect behavior caused by the inability of HA to account for cluster expansion caused by either thermal or quantum fluctuations. Although numerically exact results are not available for the quantum LJ clusters, we believe that the SCP results are at least qualitatively correct. Again, this is supported by documented comparisons of SCP with numerically exact data that is available [21, 33, 81, 83], as well as the argument [33] that the SCP equations for the classical and quantum cases are virtually the same, with quantum fluctuations and thermal fluctuations playing the same role and leading to the same effects, so that SCP should perform similarly when applied to the same system in either case. That is, given a classical anharmonic system (LJ_n in the present case) for which SCP is accurate over a certain temperature range, there should also be a range of quantum parameter Λ for which SCP accurately describes the quantum analogue of the system.

6.3   Closing remarks

In this chapter we presented several numerical examples demonstrating the utility of SCP as a practical, numerically inexpensive, and often quantitatively accurate method to compute equilibrium properties of general quantum many-body systems. In this work we focused on the effects of temperature and quantum character on the

structural properties of LJ clusters, in particular the radial pair correlation function and moments of inertia. While most comparisons of SCP with exact methods have been made with respect to classical systems, we expect that SCP should also be able to provide accurate results for quantum systems as well, based on the well-known parallel between thermal and quantum fluctuations.
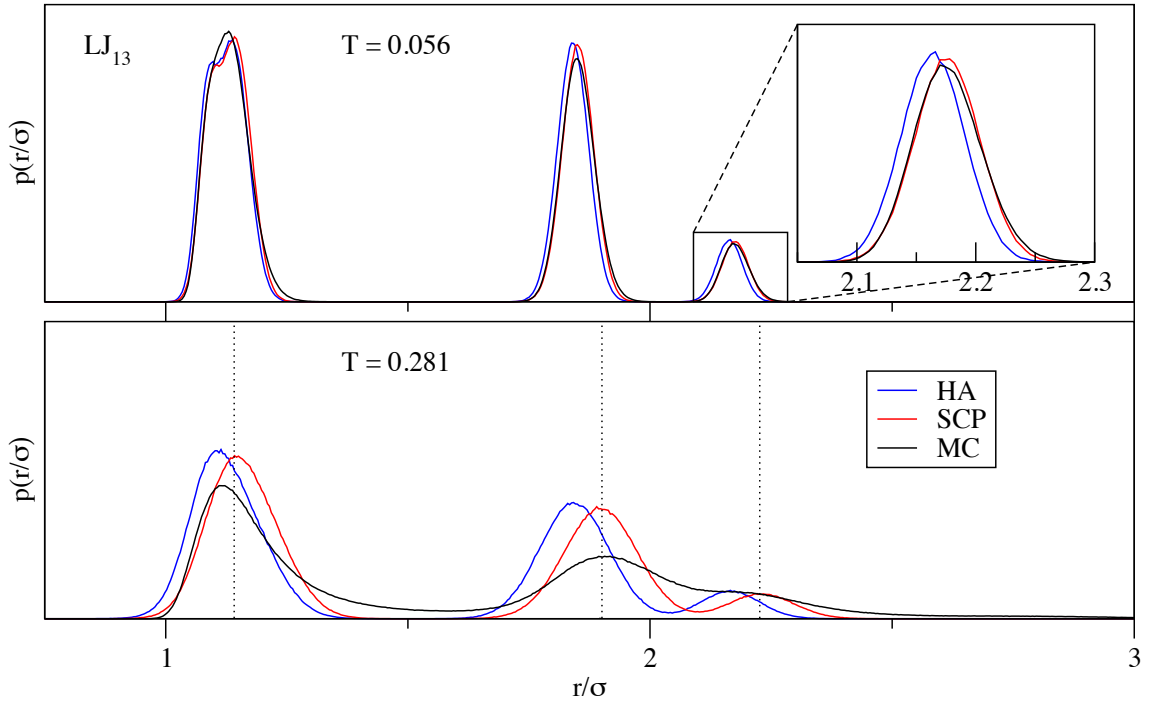
Figure 6.1: Pair correlation functions for the classical LJ$_{13}$ cluster at a low and high temperatures ($T = 0.056$, $0.281\,\varepsilon/k_{\rm B}$) computed by three different methods: the harmonic approximation (HA), the self-consistent phonons (SCP) method, and Monte Carlo (MC). The vertical dotted lines in the bottom plot indicate the positions of the peak centroids in the SCP approximation.
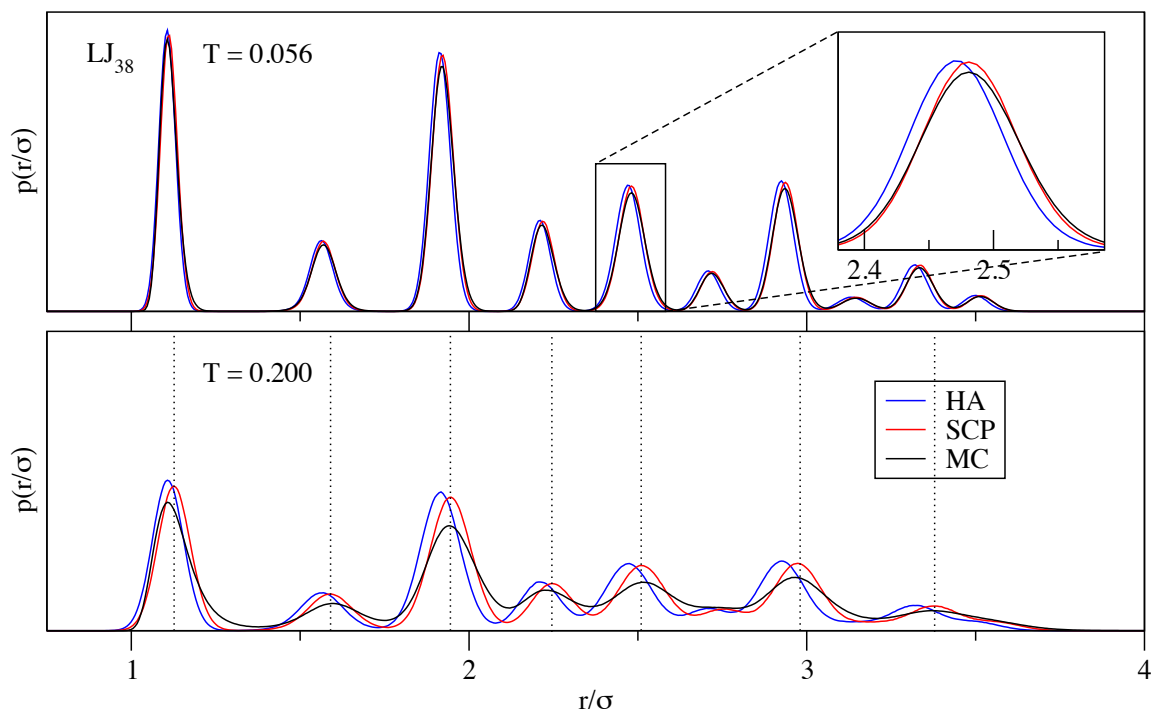
Figure 6.2: Same as Fig. 6.1, but for the octahedral LJ$_{38}$ cluster. The "high temperature" ($T = 0.200\,\varepsilon/k_{\mathrm{B}}$) in this case is the temperature above which the random walk in the Metropolis Monte Carlo simulation escapes from the octahedral potential energy minimum.
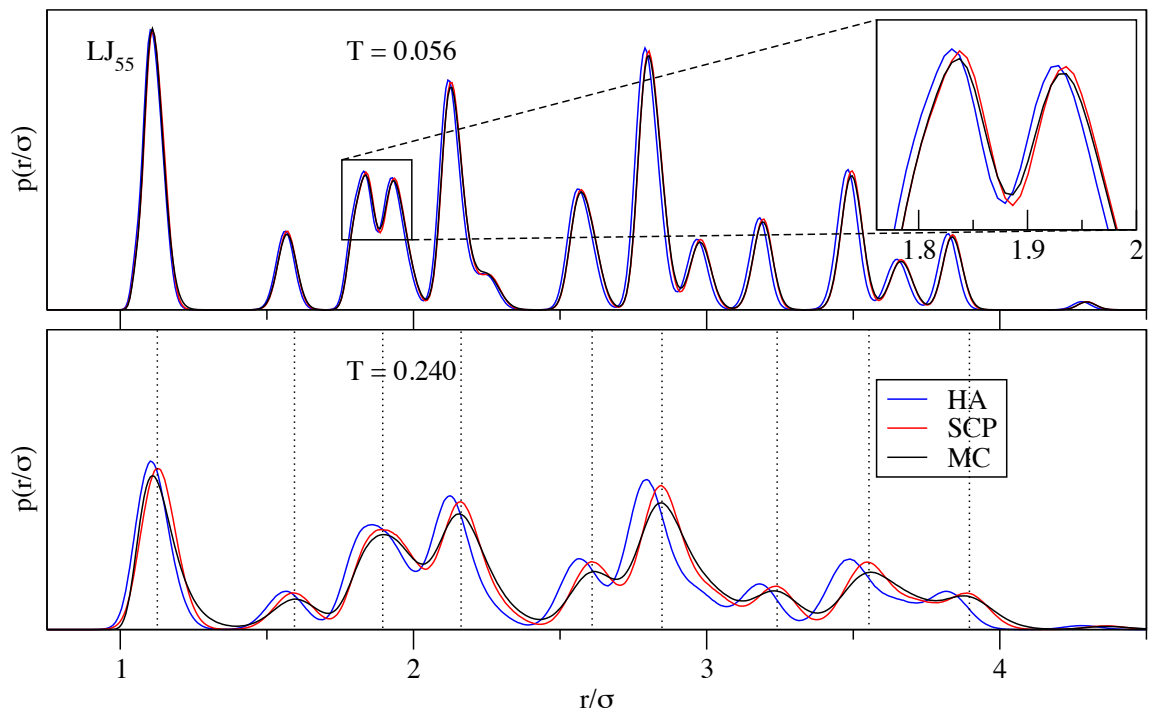
Figure 6.3: Same as Fig. 6.1, but for LJ_{55} and a "high temperature" of $T = 0.240\,\varepsilon/k_{\mathrm{B}}$.
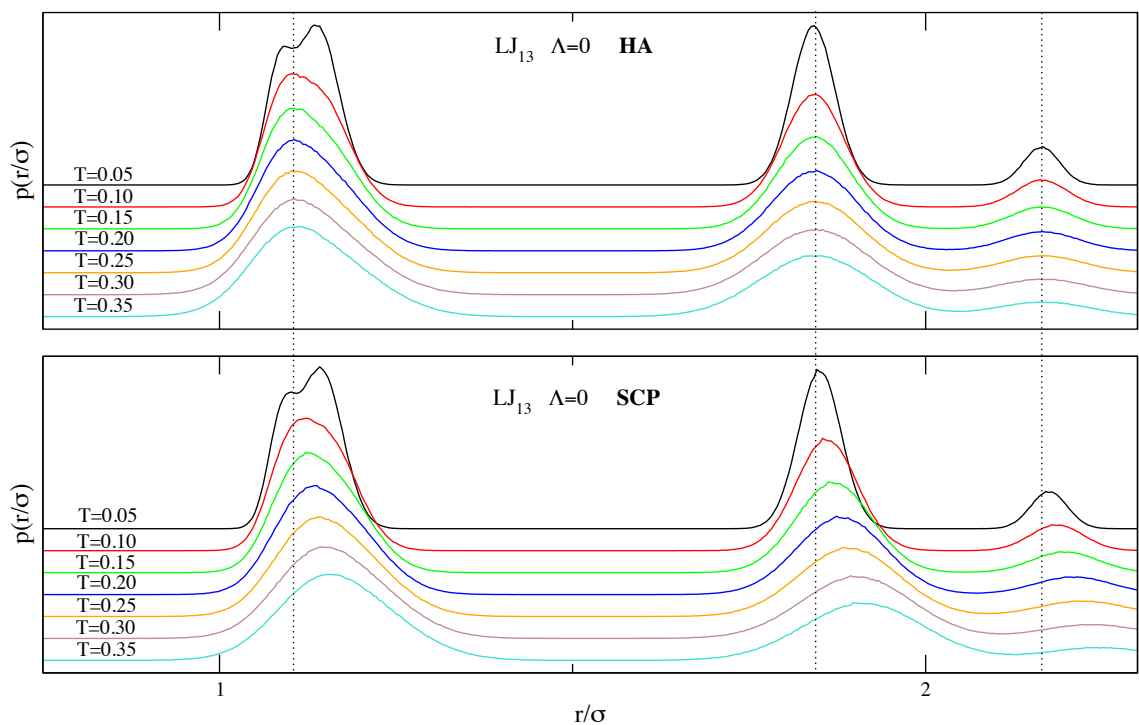
Figure 6.4: Evolution of the radial distribution function of classical LJ_{13} with temperature, computed using the standard harmonic approximation (HA) and self-consistent phonons (SCP) method. Note that the SCP method is able to produce both the broadening and drifting of the peaks with temperature, while in the HA the maxima do not shift with temperature. The vertical dotted lines are included to highlight the discrepancy between the locations of the peak centroids in the HA and SCP results.
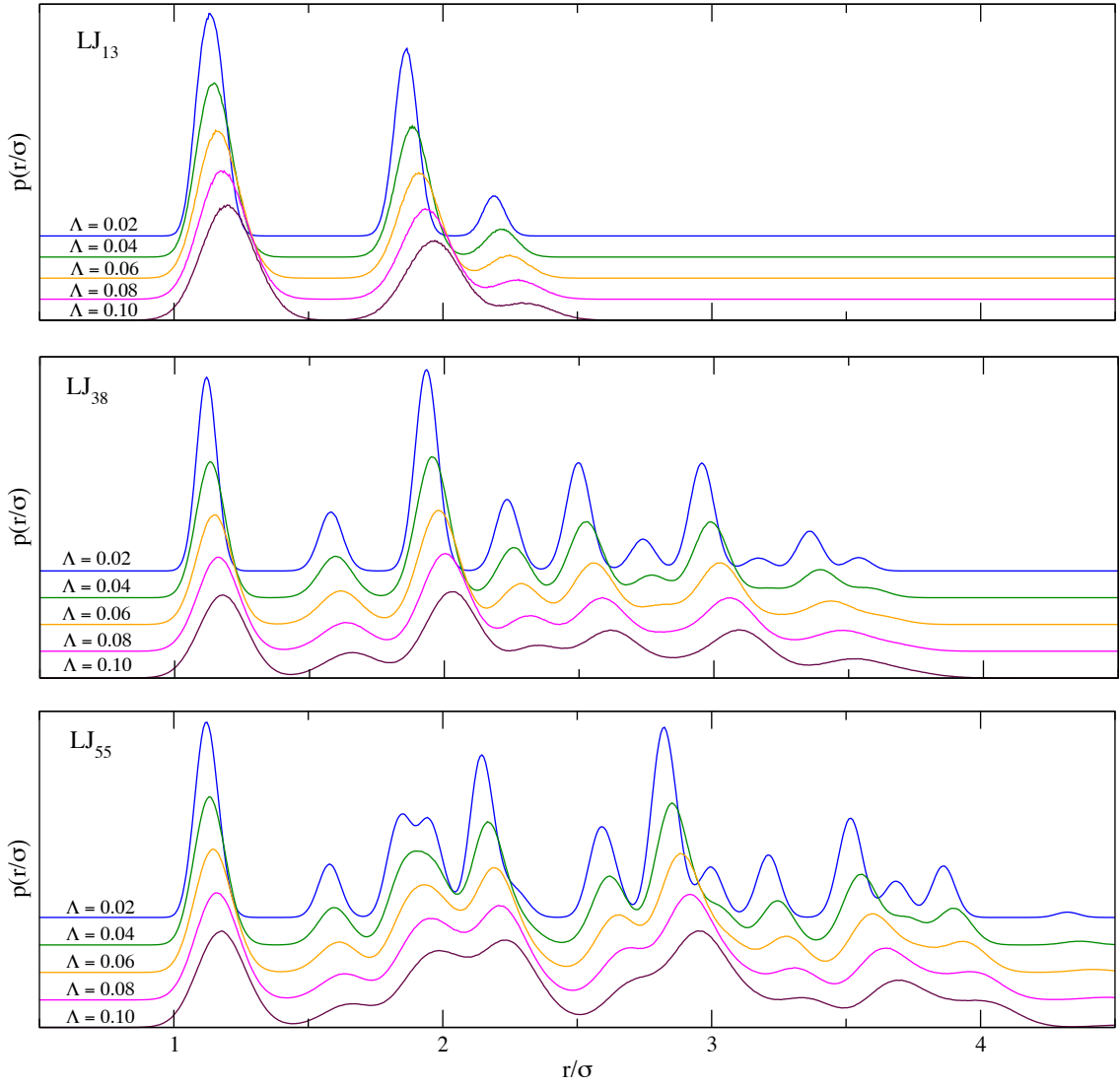
Figure 6.5: Evolution of the radial distribution function for the ground states ($T = 0$) of the quantum LJ_n ($n = 13, 38, 55$) clusters with quantum de Boer parameter $\Lambda = \hbar/(\sigma\sqrt{\varepsilon})$, computed using the self-consistent phonons method. The method is able to produce both the broadening and drifting of the peaks with increasing quantum character.
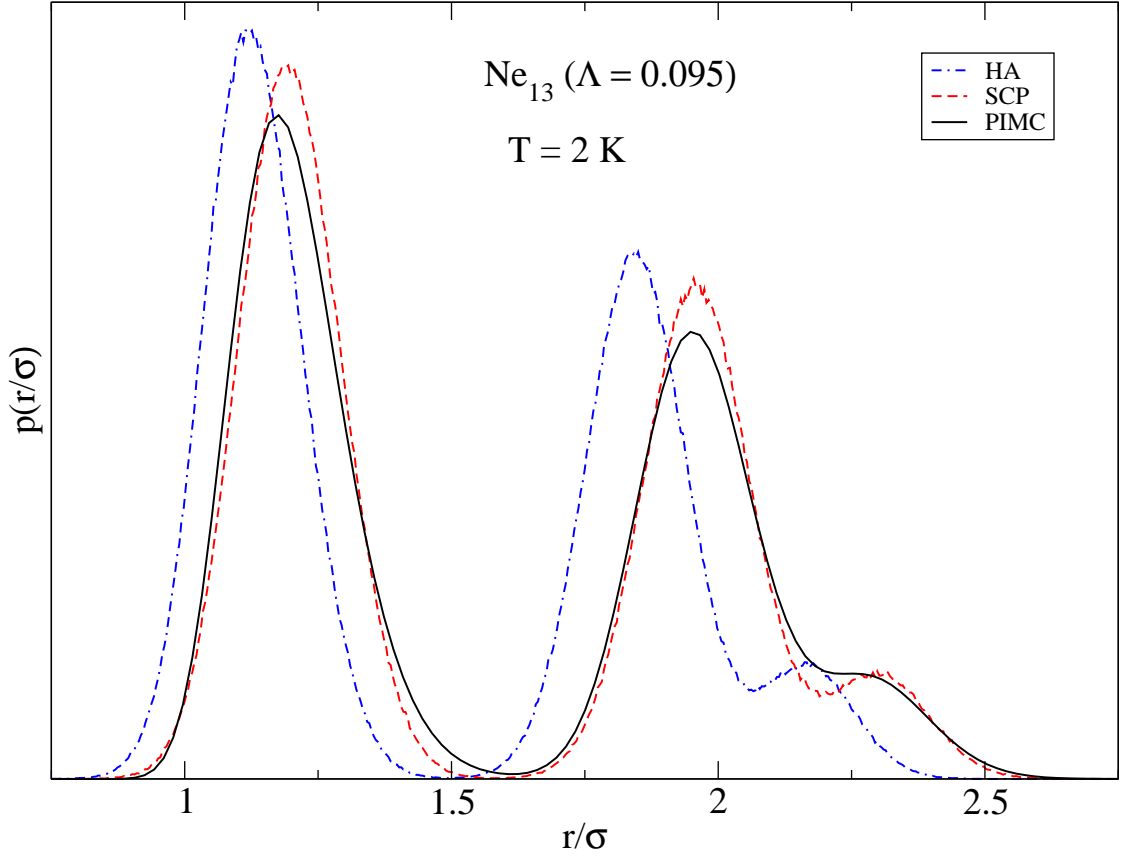
Figure 6.6: Radial distribution function for the quantum Ne_{13} cluster at temperature $T = 2\,K$ (or, more precisely, an LJ_{13} cluster with de Boer quantum parameter $\Lambda = 0.095$ at temperature $T = 0.056\,\varepsilon/k_B$) computed using the standard harmonic approximation (HA), self-consistent phonons (SCP) approximation, and path integral Monte Carlo (PIMC) [95].
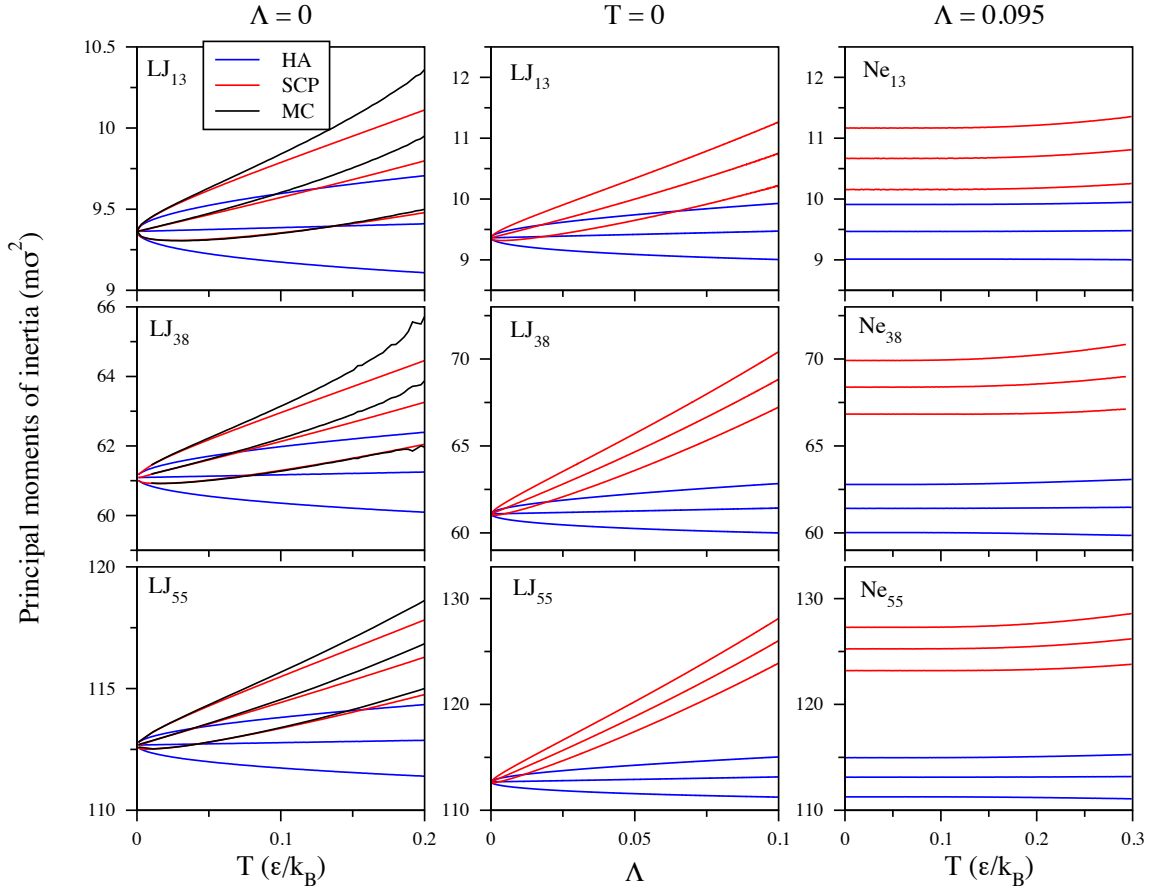
Figure 6.7: Principal moments of inertia for the LJ_{13}, LJ_{38}, and LJ_{55} clusters for three cases: as a function of temperature for the classical case ($\Lambda = 0$)(left column), as a function of de Boer delocalization length for the quantum ground state ($T = 0$) (center column), and as a function of temperature for the quantum neon clusters ($\Lambda = 0.095$). Results were obtained using the standard harmonic approximation (HA), the self-consistent phonons (SCP) method, and Markov chain Monte Carlo (MC). In the classical case, comparison with the exact MC method reveals SCP to be significantly more accurate than the standard harmonic approximation. In all cases, the SCP results show a much stronger dependence on temperature and de Boer parameter than the HA results.

Chapter 7

SCP for Free Energy Calculations

Considered by some to be one of the most important general concepts in physical chemistry, free energies are perhaps as challenging to compute as they are useful [96,97]. The difficulty in computing absolute free energies is primarily due to the direct relationship between the free energy and the canonical partition function. Even for simple systems, sampling the configuration space may prove prohibitively expensive and cannot be accomplished to any satisfactory degree in a reasonable amount of time, though this can in principle be done using Wang-Landau sampling, and has been carried out for, e.g., classical Lennard-Jones (LJ) clusters [98]. Fortunately, in many cases one is more interested in computing free energy *differences* rather than absolute free energies, as it is the free energy differences which indicate, for example, whether a process will occur spontaneously at a given temperature, or the relative stability and populations of different chemical species/isomers/isotopomers. For this purpose a number of approaches have been developed, the most general and well-known of which is thermodynamic integration (TI), whereby some reversible path

from one state to another is traversed in order to determine the difference in the free energy for the two states. In practice, traversing this path in finite time through a series of equilibrium simulations gives paths which are actually irreversible, resulting in both systematic and statistical errors. Still, the method is exact in the sense that the simulation is guaranteed to give the true free energy difference in the limit of infinite time, or infinitesimal discretization of the path.

Given that the construction of the self-consistent phonons (SCP) method is based on minimization of the Helmholtz free energy, one could reasonably expect that SCP should be ideally suited for free energy calculations. This tempting assumption resulted in a significant effort being invested in the application of SCP to free energy calculations of another notoriously challenging problem: water clusters, and in particular, water hexamer. Systems such as water, which exhibit a large "dynamical range", that is, a large difference between the intramolecular and intermolecular degrees of freedom, i.e. between the high-frequency (small-amplitude) and low-frequency (large-amplitude) motions, are particularly challenging for any method due to either conceptual or numerical difficulties or both. Like virtually all other methods for computing vibrational frequencies, SCP struggles to accurately describe large-amplitude/low-frequency vibrations, such as those corresponding to the intermolecular degrees of freedom of water and other hydrogen bonded systems. Simply, a highly anharmonic motion along a particular degree of freedom cannot be accurately described by a harmonic approximation. The vibrational contribution to the Helmholtz free energy for

an N-particle system is given by,

$$F_{\text{vib}}(T) = k_{\text{B}}T \sum_{k=1}^{3N-6} \log\left(\frac{\hbar\omega_k}{k_{\text{B}}T}\right) \qquad \text{(classical)} \qquad (7.1\text{a})$$

$$F_{\text{vib}}(T) = k_{\text{B}}T \sum_{k=1}^{3N-6} \log\left[2\sinh\left(\frac{\hbar\omega_k}{k_{\text{B}}T}\right) - \frac{\hbar\omega_k}{4}\coth\frac{\hbar\omega_k}{2k_{\text{B}}T}\right] \qquad \text{(quantum)} \qquad (7.1\text{b})$$

so that error in the low frequencies greatly distorts the resulting free energy, and is the main contribution to the overall error in these calculations. Moreover, for systems which exhibit a larger difference between the high and low frequencies, the Hessian is more ill-conditioned, and the SCP algorithm less stable (via Eqs. 3.30c and 3.32). Clearly, water clusters are one of the most challenging systems that one could consider in assessing the use of SCP for free energy calculations. In addition to the very ambitious water hexamer free energy calculations, the less formidable challenge of free energy calculations for LJ clusters was also undertaken. For both systems, results obtained using SCP were compared against the standard harmonic approximation (HA) and the "exact" TI results. As expected, the use of SCP for free energy calculations for LJ clusters, which exhibit a much narrower dynamical range, was much more accurate than for water clusters, and SCP outperformed the standard HA in this case. In the case of water clusters, HA was surprisingly found to give much better agreement with the TI results than SCP, which is likely due to a fortuitous cancellation of error. Although free energies computed using other "exact" methods have been reported, e.g., free energies for various isomers of water hexamer using replica-exchange molecular dynamics (REMD) [99], a direct comparison with these results is not meaningful for a variety of reasons which will be discussed.

7.1 Methods

7.1.1 Thermodynamic integration and reversible scaling

Consider an isomer of a classical ($\hbar = 0$) cluster corresponding to a relatively deep and stable potential energy minimum, i.e., assume that it is separated from the rest of configuration space by relatively large energy barriers. In the absence of an external field, the translations of the center of mass can be separated so that we may consider the subspace $\mathbb{R}^{(3N-3)}$ that includes only the vibrational degrees of freedom and rotations of the whole cluster. Because the potential energy $V(\mathbf{r})$ is invariant to rotations of the whole cluster, the energy minimum is a three-dimensional manifold. Consider the basin of attraction corresponding to the chosen isomer, which is a region $\mathcal{A} \in \mathbb{R}^{(3N-3)}$ in the rovibrational configuration subspace surrounding this rotationally invariant manifold. Since eventually we are interested in calculating the free energy difference between two different isomers, it suffices to consider the contribution given by the configuration integral only:

$$\beta F(T) = -\log \left[\int_{\mathcal{A}} e^{-\beta V(\mathbf{r})} \, d\mathbf{r} \right] , \tag{7.2}$$

with $\beta = 1/k_\mathrm{B} T$. Assuming that at some reference temperature $T_0 = 1/k_\mathrm{B} \beta_0$ the free energy is known, we can write

$$\begin{aligned} \beta F(T) &= \beta_0 F(T_0) + \int_{\beta_0}^{\beta} \frac{d}{d\beta'} [\beta' F(T')] \, d\beta' \\ &= \beta_0 F(T_0) + \int_{\beta_0}^{\beta} \langle V \rangle_{\beta'} \, d\beta' \end{aligned} \tag{7.3}$$

or

$$F(T) = \frac{\beta_0}{\beta} F(T_0) + W_{\text{qs}}(T) ,$$ (7.4a)

where the quasistatic work is

$$W_{\text{qs}}(T) = \frac{1}{\beta} \int_{\beta_0}^{\beta} \langle V \rangle_{\beta'} \, d\beta'$$ (7.4b)

with the average defined by

$$\langle V \rangle_{\beta'} := \frac{\int_{\mathcal{A}} V(\mathbf{r}) e^{-\beta' V(\mathbf{r})} \, d\mathbf{r}}{\int_{\mathcal{A}} e^{-\beta' V(\mathbf{r})} \, d\mathbf{r}} .$$ (7.4c)

Equation 7.4 is a variant of the thermodynamic integration relationship with β being a generalized displacement variable, and the integrand, the generalized force. The reversible scaling (RS) method [100, 101] computes the dynamical work done along a non-equilibrium process as an estimator for the quasistatic work, enabling instantaneous values of the driving force to be used rather than equilibrium ensemble averages:

$$W_{\text{qs}}(T) \approx W_{\text{dyn}}(T) = \frac{1}{\beta} \int_0^t \frac{d\beta(t')}{dt'} V_0[\mathbf{r}(t')] \, dt' ,$$ (7.5)

where we consider a function $\beta = \beta(t)$ with $\beta(0) = \beta_0$, which changes slowly with the simulation time t. At each time step, a new configuration is generated by Metropolis Monte Carlo (MC), and the generalized force $V_0[\mathbf{r}(t)]$ computed.

The key advantage of RS over equilibrium approaches (e.g, TI, adiabatic switching) is that the entire $F(T)$ curve can be obtained in a single simulation. In the limit of an infinitely slow process Eq. 7.5 becomes exact. However, for any finite-time realization of this approach $W_{\text{dyn}}(T)$ will suffer from both statistical and systematic errors. The statistical error can be reduced by considering the dynamical work aver-

aged over multiple finite simulations, which, by the second law of thermodynamics, always gives an upper bound for the quasistatic work:

$$W_{\mathrm{dyn}}(T) > W_{\mathrm{qs}}(T) \ . \tag{7.6}$$

Having implemented both TI and RS as described above, we found TI to be more robust. All reported results were obtained by estimating the quasistatic work using Eq. 7.4.

The prerequisite for RS and TI as implemented here is the existence of a reference state for which the free energy of the system is known. Here we have taken our reference to be the physical system at a sufficiently low temperature T_0 such that the free energy $F(T_0)$ can be estimated accurately using a harmonic (or quasiharmonic) approximation. The free energy as a function of temperature $F(T)$ is then computed by evaluating the quasistatic work by integrating over the temperature, which changes gradually from T_0 to T. The use of a low-temperature harmonic reference in RS calculations for LJ clusters was later found to have been carried out previously by the usual suspects [9]. Ref. 102 considers much more elaborate reference states for liquid and solid LJ clusters, and uses RS to estimate the melting temperature of LJ$_{55}$.

The standard normal mode/harmonic approximation was used to obtain low-temperature free energy references for both the LJ and water clusters. However, this required special care for the water clusters, as it can be problematic for the present case where the Hessian is not available analytically, and must instead be evaluated using finite differences. Evaluation of the Hessian by finite differences can result in difficult to control errors in the normal mode frequencies, to which the free energy

differences are extremely sensitive. This is because large cancellations result in a free energy difference which is generally much smaller in magnitude than the free energy values from which it is determined. Moreover, low-frequency modes account for the greatest contribution to the free energy differences for the case of water clusters. Inaccurate reference values would manifest as a change in the slope of $F(T)$, according to Eq. 7.4a. In an attempt to circumvent the problem, the low-temperature free energy references were also estimated by the SCP method, which does not require an explicit knowledge of the Hessian [57], and can in principle achieve any desired accuracy. In the $T_0 \to 0$ limit, HA and SCP coincide.

Consider a particular isomer of an N-atom cluster corresponding to a relatively deep and stable potential energy minimum, i.e., we assume that it is separated from the rest of the configuration space by relatively large energy barriers. In the absence of an external field, the translations of the center of mass can be separated so that we may consider the subspace $\mathbb{R}^{(3N-3)}$ that includes only the vibrational degrees of freedom and the rotations of the whole cluster. Because the potential energy $V(\mathbf{r})$ is invariant to these rotations, the energy minimum is a (3)-dimensional manifold. The TI and RS procedures described here can be used to estimate the free energy difference between cluster isomers in the Eckart subspace, i.e., the $(3N - 6)$-dimensional subspace orthogonal to the rotational and translational degrees of freedom (see, e.g., the discussion in Ref. 57). In this case we can set the value of $F(T_0)$ defined by the standard normal mode expression,

$$F(T_0) \approx E_{\min} + \frac{1}{\beta_0} \sum_{k=1}^{3N-6} \log(\beta_0 \hbar \omega_k) \ , \tag{7.7}$$

where we have dropped all terms that cancel when the free energy difference is taken. Here E_{min} denotes the energy at the minimum, and ω_k are the effective harmonic frequencies.

7.1.2 Rotational correction to the harmonic and SCP approximations

The rotational contribution to the free energy may be important for relatively small clusters and when the inertia tensors of the two isomers in question are very different. In this case we propose the use of a rigid asymmetric top correction [103], which with the omission of terms that cancel when the energy difference between isomers is considered, reduces to

$$F_{\text{rot}}(T) \approx -\frac{1}{2\beta} \log \frac{I_1 I_2 I_3}{\beta^3 \hbar^6} + \frac{1}{\beta} \log \sigma \;, \tag{7.8}$$

where I_1, I_2 and I_3 are the principal moments of inertia of the isomer evaluated at its minimum configuration, and σ is the order of the isomer point group, which is unity unless the isomer configuration has symmetries. For the reference free energy, this yields

$$F(T_0) \approx E_{\text{min}} + \frac{1}{\beta_0} \left[\sum_{k=1}^{3N-6} \log(\beta_0 \hbar \omega_k) + \log \sigma - \frac{1}{2} \log \frac{I_1 I_2 I_3}{\beta_0^3 \hbar^6} \right] \;. \tag{7.9}$$

Note that the same rotational term can be used to approximately include the rotational contribution in the SCP free energy. For water hexamer the rotational contribution to the free energy difference between the cage and prism isomers was found to be on the order of $0.1\ k_{\text{B}}T$.

To summarize this section, for two isomers A and B the free energy difference at

temperature T can be estimated using

$$F_A(T) - F_B(T) = E_{\min}^A - E_{\min}^B \tag{7.10}$$

$$+ \frac{1}{\beta} \left[\sum_{k=1}^{3N-6} \log \frac{\omega_k^A}{\omega_k^B} + \frac{1}{2} \log \frac{I_1^B I_2^B I_3^B}{I_1^A I_2^A I_3^A} + \log \frac{\sigma_A}{\sigma_B} \right]$$

$$+ \frac{1}{\beta} \left[\int_{\beta_0}^{\beta} d\beta' \left(\langle V \rangle_{\beta'}^{A} - \langle V \rangle_{\beta'}^{B} \right) \right] .$$

Note that for a harmonic system the free energy difference is linear in T, and that it

is the final term in the above expression that accounts for anharmonic contributions.

7.2   Results and discussion

All "exact" results presented in this chapter were calculated using TI, with the qua-

sistatic work computed by Eq. 7.4. Although RS calculations were also performed and

yielded similar results, we found the implementation of this non-equilibrium approach

more cumbersome due to the need to optimize the parameter dependence $\beta = \beta(t)$

to reduce the systematic error. Arguably, the most challenging aspect of performing

an RS or TI calculation is the choice of an appropriate reference for the system for

which the free energy is known. For a classical system in the limit of low-temperature,

SCP is exact and coincides with HA, and could be expected to serve as an accurate

reference at low enough temperature. A clear indication that the choice for initial

temperature T_0 in the TI procedure (Eq. 7.3) is too high, i.e., that $F(T_0)$ is not suf-

ficiently accurate, would be a sensitivity of $F = F(T)$ to the choice of T_0, that is,

if slightly modifying the reference temperature T_0 produces $F(T)$ results which are

not consistent with one another. The integration in Eq. 7.4b was performed over a uniform temperature grid of either 100 or 1000 points using the trapezoid rule. The rotational contribution to the free energy differences based on the asymmetric top is included in all calculations.

7.2.1 Classical free energies for Lennard-Jones clusters

Classical free energy differences for the icosahedral (C5v) and octahedral (Oh) isomers of the LJ_{38} cluster computed by HA, SCP, and TI are presented in Fig. 7.2. The structure of the isomers is shown in Fig. 7.1. While a large number of calculations were carried out to compute free energy differences between the icosahedral and octahedral LJ_{38} clusters, the decahedral (D5h) and icosahedral (C1) LJ_{75} clusters, and the tetrahedral (Td) and icosahedral (Cs) LJ_{98} clusters, we present here a single representative figure corresponding to LJ_{38}. A hard constraining radius of 3.0σ was used for the LJ_{38} clusters. Several different low-temperature free energy references determined from HA were used and found to give consistent results, shown in Fig. 7.2. Using SCP to generate low-temperature free energy references for TI was found to give nearly identical results, which are not shown. The agreement between the exact-in-principle TI results and inherently approximate SCP results suggests a fairly broad temperature range over which the SCP approximation can be expected to give accurate free energy differences (and likely accurate absolute free energies) for LJ clusters, and complements the assessment of SCP given in Chapter 6. At $\sim 0.13\ \varepsilon/k_{\mathrm{B}}$, the TI simulations appear to begin sampling beyond the desired region

of configuration space.

Special care is required in correctly identifying the configurations for each TI simulation as the isomer of interest, i.e., for ensuring that only the minima corresponding to the particular isomer of interest are being sampled. For example, unconstrained TI calculations result in simulations where the Metropolis MC sampled minima that did not correspond to the isomer of interest, e.g., a calculation intended to produce free energy as a function of temperature for icosahedral LJ$_{38}$ would eventually sample configurations corresponding to octahedral LJ$_{38}$. In order to prevent each TI simulation from sampling beyond the desired region of the PES, we found it necessary to introduce a constraint based on the Q_6 orientational bond order parameter [104], which was chosen over other Q_l parameters based on its ability to better distinguish between isomers in LJ clusters [91]. The Q_l order parameter is defined by

$$Q_l = \left(\frac{4\pi}{2l+1} \sum_{m=-l}^{m=l} |\overline{Q}_{lm}|^2 \right), \quad \overline{Q}_{lm} = \frac{1}{N_b} \sum_{r_{ij}<r_b} Y_{lm}(\theta_{ij}, \phi_{ij}) , \qquad (7.11)$$

where $Y_{lm}(\theta, \phi)$ denotes the spherical harmonics, $r_b = 1.392\sigma$, and $N_b = |r_{ij} < r_b|$. The order parameter Q_l is invariant to the coordinate frame, and therefore does not depend on the cluster orientation. Parameters Q_4 and Q_6 are often used to distinguish or identify structural motifs of LJ clusters. Figure 10 of Ref. 91 shows the Q_6 values corresponding to four different structural types for LJ$_{38}$ (octahedral, MacKay (icosahedral), anti-MacKay (icosahedral), and liquid) up to about $T = 0.4\ \varepsilon/k_{\mathrm{B}}$. Based on these results, TI calculations were repeated with the Q_6 order parameter constrained to $[0.1, 0.4]$ for the icosahedral isomer, and to $[0.4, 0.7]$ for the octahedral isomer.
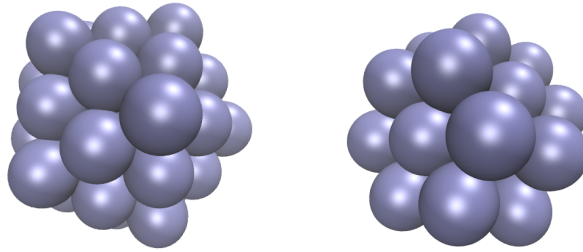
Figure 7.1: The minimum energy icosahedral (left) and octahedral (right) isomers of the classical LJ_{38} cluster.
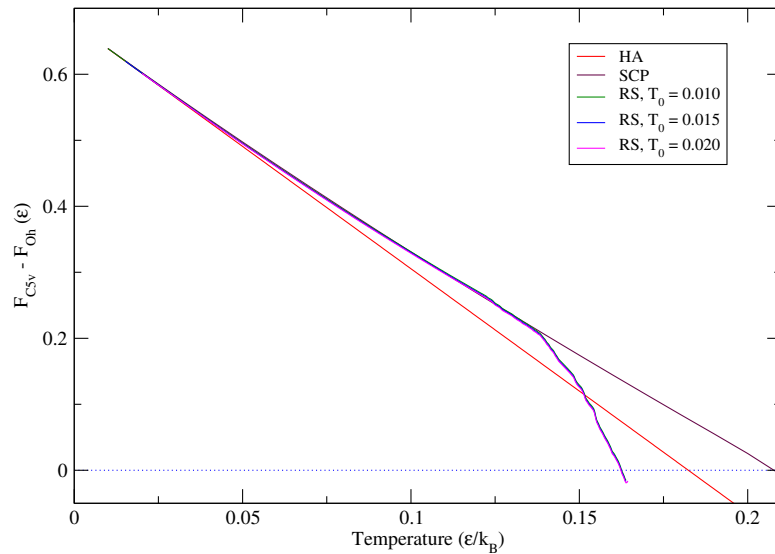
Figure 7.2: Classical free energy differences as a function of temperature for the icosahedral (C5v) and octahedral (Oh) isomers of the LJ_{38} cluster, computed using the standard harmonic approximation (HA), the self-consistent phonons (SCP) method, and thermodynamic integration (TI). TI results obtained using several different low-temperature free energy references determined from HA were found to be consistent with one another.

7.2.2 Classical free energies for water hexamer

Classical free energy differences for the cage and prism isomers of the water hexamer cluster computed by HA, SCP, and TI are presented in Fig. 7.4. As before, while a very large number of calculations were carried out for several different isomers of water hexamer and potentials, we present here only a single representative figure showing the free energy differences computed for the cage and prism isomers, shown in Fig. 7.3, using the q-TIP4P/F PES [79]. In full, five isomers of water hexamer – book, cage, prism, prism book, and strange book – were considered, using the empirical q-TIP4P/F potential, and the WHBB [68,69], and HBB2-pol [105] potentials, which have been constructed by parametrizing high-level *ab initio* data. SCP calculations were carried out following the protocol of Chapter 5 and Ref. 57. The TI and RS simulations are valid as long as the random walk stays in the basin of attraction corresponding to a particular isomer. At sufficiently high temperature, these simulations were found to leave the region of interest. The corresponding temperatures for each potential were $T \sim 50\,\mathrm{K}$ for q-TIP4P/F, and $T \sim 75\,\mathrm{K}$ for WHBB and HBB2-pol. No attempts were made to constrain the TI simulations, though this could be done by implementing a variety of geometric constraints, as done in Ref. 73.

Several different low-temperature free energy references determined from HA were used and found to give consistent results. Using SCP to generate low-temperature free energy references for TI was found to give inconsistent results, shown in the lower panel of Fig. 7.4. Moreover, regardless of the reference used, the TI results are found to agree much more closely with the HA results than with the SCP results. We con-

clude that SCP is not well-suited for free energy calculations for water clusters, while fortuitous error cancellations are the likely reason for the surprisingly good agreement between TI and HA. These findings are all the more disappointing considering the favorable assessment of SCP provided in Ref. 81 for the very case of water hexamer, albeit for the calculation of the isomer energy differences at zero-temperature (i.e., for the isomer ground states). While it is true that SCP is exact for a classical system in the limit $T \to 0$, the behavior of the method was unexpectedly found to change rapidly at low temperatures, so that finding an appropriate or "trustworthy" choice of T_0 is, at best, problematic. As previously mentioned, the inability of SCP to provide accurate free energies for water clusters, even at low temperature, is an indication that the method suffers from the well-known "curvature problem". The large difference between the high-frequency and low-frequency modes results in a large condition number for the Hessian, and a system characterized by stiff equations. In addition, it is very likely that the low-frequency modes are simply too anharmonic to be satisfactorily described by a Gaussian.

It may be possible to partially resolve the problem by revising the numerical approach used to solve the SCP equations (Eqs. 3.17). Neumaier [106] has proposed and detailed the use of a conjugate-gradient descent algorithm in place of the Newton-Raphson-type approach that we have been using to date. This is expected to yield a more stable iterative minimization scheme which is better equipped to deal with ill-conditioned Hessian matrices (e.g., as encountered when working with water clusters). This new implementation using conjugate-gradient descent would take $\mathbf{W}$, $\mathbf{\Lambda}$, and center $\mathbf{q}$ as variational parameters, where the matrices $\mathbf{W}$ and $\mathbf{\Lambda}$ are defined from
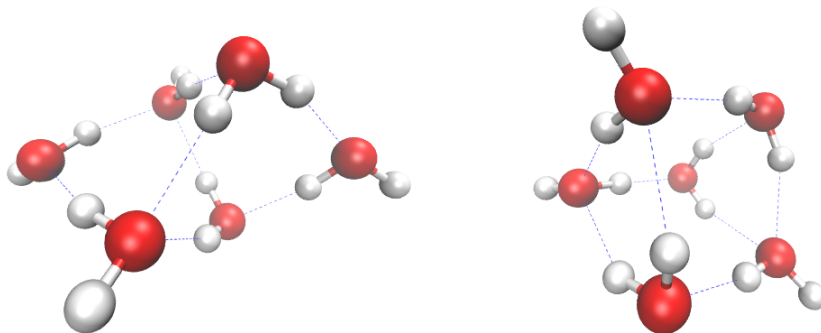
Figure 7.3: The minimum energy cage (left) and prism (right) isomers of water hexamer for the q-TIP4P/F potential energy surface.

the mass-scaled Hessian $\tilde{\mathbf{K}}$:

$$\frac{1}{2}\hbar\beta\tilde{\mathbf{K}}^{1/2} = \mathbf{W}\mathbf{\Lambda}\mathbf{W}^T \,, \quad \mathbf{W}\mathbf{W}^{\mathrm{T}} = \mathbf{I} \,. \tag{7.12}$$

However, even in the best-case scenario, these improvements would only be able to address the convergence and stability of the method, and would not be able to address the fundamental limitations of approximating highly anharmonic intermolecular modes by Gaussians.

7.2.3 Considerations regarding comparison with other methods, especially replica-exchange methods

Although RS or TI can be used as an efficient alternative to the replica-exchange (RE) method, it is important to note that the optimal conditions for RS/TI and RE are opposite of one another, so that comparing results obtained from the two types of
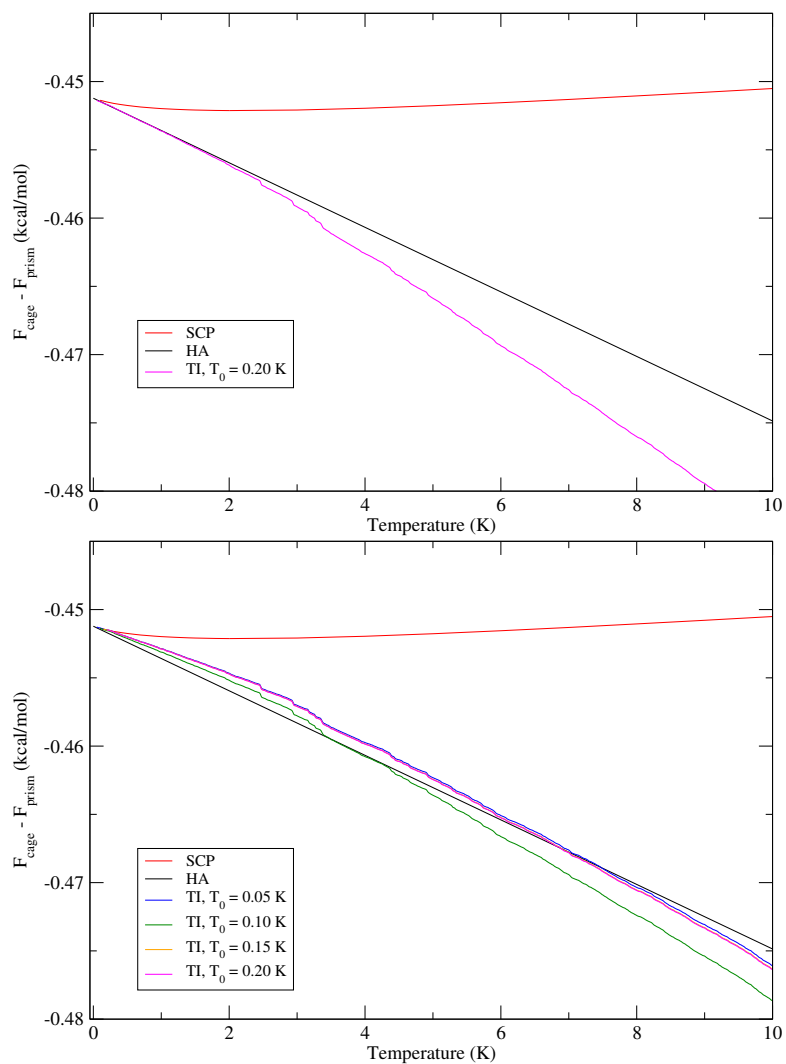
Figure 7.4: Classical free energy differences as a function of temperature for the cage and prism isomers of water hexamer computed using the standard harmonic approximation (HA), the self-consistent phonons (SCP) method, and thermodynamic integration (TI). Upper panel: Several different low-temperature reference free energies $F(T_0)$ determined from HA were used and found to produce consistent results; the result for $T_0 = 0.20\,\text{K}$ is shown. Lower panel: Several different low-temperature reference free energies $F(T_0)$ determined from SCP were attempted and compared, and found to produce inconsistent results.

methods is generally not very meaningful. In order for an RE simulation to be efficient (ergodic), the highest replica temperature must be high enough for the random walk to switch frequently between the relevant basins of attraction; an energy barrier which is too high leads to a rapid loss of ergodicity. In the RS method, the random walk eventually leaves the basin of attraction of interest at high enough temperature, leading to the breakdown of the method. Like RS, both SCP and HA are designed to explore configurations which are confined to a particular basin of attraction of the PES. Given that there may be multiple minima of the PES which correspond to the same isomer, e.g. prism, this difference complicates the issue of making a direct comparison between the two types of methods. (Note that for water clusters, isomers are classified on the basis of the location of the oxygen atoms, while the positions of the hydrogen atoms may vary.) Supposing that there are N_A equivalent minima corresponding to isomer A, and N_B equivalent minima corresponding to isomer B, (we assume that the minima corresponding to a given isomer are equivalent for the sake of simplicity), then the partition functions for the isomers A and B computed by SCP or RS should be multiplied by N_A and N_B, respectively. The correction to the free energy difference $F_A - F_B$ is then

$$-k_B T \log \frac{N_A}{N_B} \ .$$

Clearly, this quantity can only become significant if the ratio N_A/N_B is significantly different from unity. The related issue of assigning sampled configurations to a particular type of isomer when carrying out an REMC or REMD simulation is another possible source of discrepancy. Typical approaches include "quenching" or imple-

menting a geometric criterion based on, e.g., root mean squared distances. Finally, while an RE simulation should, in principle, be able to sample multiple minima corresponding to the same isomer, it can be difficult to determine if this is actually achieved. In spite of being exact methods, it can be difficult to ascertain whether an REMC or REMD simulation is truly converged. We refer the reader to Fig. 4 of Ref. 2, which illustrates a striking example of apparent convergence with the use of the RE method. The figure demonstrates that even an exceptionally long RE simulation, in which the results (heat capacities) exhibit a smooth temperature dependence, and change only slightly using variable simulation lengths, could in fact be very far from truly converged.

7.3   Closing remarks

The SCP method is built upon minimization of the Helmholtz free energy of the harmonic reference system, which gives an upper bound for the free energy of the physical system, and would seem to be a natural choice for free energy calculations for a variety of systems. For the case of LJ clusters, in which the distinction between high- and low-frequency modes is not too great, SCP was found to give free energy differences in very good agreement with the exact TI results over a temperature range approaching the "melting" temperature of each LJ cluster. In the very challenging case of water clusters, however, we have found that difficulties in accurately describing the highly anharmonic low-frequency modes in a system with a large dynamical range prevent SCP from giving reliable free energies, even at "very low" temperature

($\sim 0.1\,\mathrm{K}$). Surprisingly, the standard HA was found to give much better agreement with TI, which may simply be an indication of some very large and fortuitous error cancellation. While the problem may be ameliorated to some degree with algorithmic improvements, one cannot expect *any* quasiharmonic approximation to accurately describe the large-amplitude intermolecular modes of water clusters. A much more promising application of SCP, the calculation of vibrational spectra, is discussed in the following chapter.

Chapter 8

SCP for Computing Vibrational Spectra

In exploring the use of the self-consistent phonons (SCP) method for the calculation of vibrational or infrared (IR) spectra, we return our focus once more to water clusters. SCP's ability to incorporate anharmonic effects and quantum effects in a temperature-dependent manner make it a strong candidate for investigating fundamental phenomena, such as temperature-dependence of anharmonic spectra and quantum effects, particularly isotope effects. In this context, water clusters appear again as the perfect challenge, as they possess the features and qualities that SCP is expressly designed to describe. While it has been difficult to determine the accuracy of many "competing" quantum dynamics methods for computing IR spectra of aqueous systems, state-of-the-art experimental procedures [107, 108] offer the promise of a direct comparison between experiment and theory for water and ion-water clusters at a given temperature.

The ability of small water clusters, and water hexamer in particular, to serve as model systems for elucidating the complicated structure and dynamics of bulk, condensed-phase water has made them the subject of intense and on-going interest. Water hexamer is the smallest water cluster whose minimum energy configurations exhibit three-dimensional structures similar to those found in bulk water, in contrast to the ring structures favored by smaller clusters [70, 109–111]. Its deceptively diminutive title of "smallest drop of water" downplays the fact that water hexamer has proven to be a very challenging and even controversial system for experimentalists and theorists alike. On the experimental front, the problem has been attacked using a battery of spectroscopic techniques, but such spectroscopic data may be difficult to interpret reliably without the aid of complementary computational studies. Attempts to make structural assignments for experimental spectra with the help of simulations often resort to tactics such as uniformly shifting or scaling data, with little to no physical justification for doing so, e.g., uniformly shifting or scaling harmonic frequencies with the intention of correcting for anharmonicities in water so that a direct comparison with experiment can be made (see, for example, Ref. 112). Inconsistencies and work-arounds such as these demonstrate that the current state of affairs leaves much to be desired.

In principle, classical simulations can be a very cost-effective approach for gaining insight on the behavior of these systems, but evidence of the importance of quantum effects in water and other hydrogen-bonding networks continues to mount. Nuclear quantum effects (e.g. zero-point vibrations) have generally been thought to destabilize the hydrogen bond network, "softening" the structure of liquid water [113, 114].

However, with the advent of improved water models, it has become increasingly clear that the situation is more complicated than may have been expected. Over the last several years, the problem has become confounded by evidence that there is a competition between quantum effects at play in hydrogen-bonded systems [115], and in water in particular [79, 116], which depends sensitively upon temperature [115, 116]. Quantum fluctuations of the intramolecular bond stretching tend to strengthen hydrogen bonds as a result of larger monomer dipole moments, while intermolecular quantum fluctuations tend to weaken them [79, 115]. Of special relevance to the work described in this chapter, quantum effects have been found to have a significant impact on the IR spectrum of DOH in H_2O even at high temperature (600 K) [117].

As mentioned in Chapter 1, no exact method exists for computing quantum dynamics of condensed phases for anything but the simplest of systems. Among these approximate methods are the popular centroid molecular dynamics (CMD) and ring-polymer molecular dynamics (RPMD), both *ad hoc* approaches whose use in computing vibrational spectra requires some justification and evaluation [118]. While CMD has been used with varying degrees of success to study the vibrational spectra of various water systems, it cannot be expected to give accurate results in many cases, due to the so-called "curvature problem" [119]. Of note is the work of Ref. [120], investigating the temperature-dependence of the IR spectrum for HOD solvated in bulk H_2O. Here the authors utilized CMD to compute 2D IR spectra and other spectroscopic details for HOD in H_2O, yielding "fairly good agreement" with experiment [120]. However, HOD in H_2O presents a special case where CMD was able to perform well. More generally, CMD is known to produce unphysical artifacts, and is exact only for

harmonic systems and in the limit of high temperature. Similarly, RPMD is known to produce unphysical frequencies corresponding to the internal vibrational modes between adjacent ring-polymer beads, which have been known to appear in the region of interest (e.g., the O−H stretching region for water) and couple with the physical modes of the system [121]. Moreover, attempts to mitigate the RPMD's spurious frequency problem, e.g., by adjusting the mass of the ring-polymer beads, can inadvertently give rise to other problems. For clusters which are small enough, it is possible to treat all degrees of freedom quantum mechanically. For larger systems a mixed quantum-classical approach must be used, whereby only degrees of freedom of special interest are treated quantum mechanically, and the remaining degrees of freedom are treated classically.

In addition to the challenge of finding a suitable method for the determination of temperature-dependent anharmonic spectra is the challenge associated with obtaining an accurate description of the potential energy surface of water clusters over a range of temperatures. Empirical water models, fit to match experimental data under certain conditions, cannot be expected to produce reliable results beyond the range of conditions under which they were parameterized. Thus, any empirical water model would be a poor choice for the work presented here. The MB-pol water potential has been developed using a first-principles–based construction with the express goal of accurately describing water from gas-phase clusters to condensed phases. The accuracy of this potential and its individual components (e.g., two-body term, three-body term) has been demonstrated in a variety of ways, including comparison with experimental second and third virial coefficients; vibrational-rotational tunneling spectra;

and various thermodynamic, structural, and dynamical data for liquid water at ambient conditions [76–78]. MB-pol has recently been expanded upon to describe halide ion-water interactions in the i-TTM potential [122] and clearly stands apart from its predecessors in terms of its construction, accuracy, and speed, making it the natural choice for this work.

In this chapter we reveal vibrational spectra for various low-lying isomers of water hexamer at zero-temperature, as well as temperature-dependent infrared spectra. Vibrational frequencies for the water 20-mer are also reported. In this work, we have used the SCP method [29] in conjunction with the recently developed MB-pol water potential and MB-μ dipole moment surface of Paesani and coworkers [76–78, 123]. In addition, generation of the temperature-dependent spectra relied on relative isomer populations determined from RE-PIMD simulations [124].

8.1   Methods

8.1.1   Computing intensities of spectral lines in SCP

We consider again an N-atom cluster at thermal equilibrium in a particular minimum of a given PES. In the SCP approximation (or more generally, in a quasiharmonic approximation) the intensity $\mathcal{I}_j$ of the spectral line for the jth mode is approximated by

$$\mathcal{I}_j \approx \left| \left\langle \frac{\partial \boldsymbol{\mu}}{\partial q_j} \right\rangle \right|^2 , \tag{8.1}$$

where $\boldsymbol{\mu}$ is the dipole moment of the cluster and q_j is the jth component of the "normal mode" coordinates $\mathbf{q} \in \mathbb{R}^{3N}$. The gradient of the dipole moment with respect to the normal mode coordinates is given by

$$\frac{\partial \boldsymbol{\mu}}{\partial q_j} = \sum_{i=1}^{3N} \frac{1}{\sqrt{m_i}} \tilde{\mathbf{U}}_{ij} \frac{\partial \boldsymbol{\mu}}{\partial r_i} \ , \tag{8.2}$$

where $\mathbf{r} \in \mathbb{R}^{3N}$ are the cartesian coordinates, and $\tilde{\mathbf{U}} \in \mathbb{R}^{3N \times 3N}$ is the orthogonal matrix which diagonalizes the mass-scaled Hessian in the Eckart subspace:

$$\mathbf{P}\tilde{\mathbf{K}}\mathbf{P} = \tilde{\mathbf{U}} \operatorname{diag}(\omega^2) \tilde{\mathbf{U}}^{\mathrm{T}} \ . \tag{8.3}$$

By extension, the ij^{th} element of $\frac{\partial \boldsymbol{\mu}}{\partial \mathbf{q}} \in \mathbb{R}^{3 \times 3N}$ is given by

$$\left(\frac{\partial \boldsymbol{\mu}}{\partial \mathbf{q}}\right)_{ij} = \sum_{k=1}^{3N} \frac{1}{\sqrt{m_k}} \tilde{\mathbf{U}}_{kj} \left(\frac{\partial \boldsymbol{\mu}}{\partial \mathbf{r}}\right)_{ik} = \sum_{k=1}^{3N} \left(\frac{\partial \boldsymbol{\mu}}{\partial \mathbf{r}}\right)_{ik} \frac{1}{\sqrt{m_k}} \tilde{\mathbf{U}}_{kj} \ , \tag{8.4}$$

or we can simply write

$$\left(\frac{\partial \boldsymbol{\mu}}{\partial \mathbf{q}}\right) = \left(\frac{\partial \boldsymbol{\mu}}{\partial \mathbf{r}}\right) \mathbf{M}^{-1/2} \tilde{\mathbf{U}} \ . \tag{8.5}$$

In the same manner that we can avoid explicit evaluation of the Hessian when computing its expectation value (Eq. 5.3b), we can use a variant of Eq. 5.3a to avoid explicit evaluation of the dipole moment gradient when computing its expectation value:

$$\begin{aligned}
\left\langle \frac{\partial \boldsymbol{\mu}}{\partial \mathbf{q}} \right\rangle &= \left\langle \left(\frac{\partial \boldsymbol{\mu}}{\partial \mathbf{r}}\right) \mathbf{M}^{-1/2} \tilde{\mathbf{U}} \right\rangle \\
&= ||2\pi \mathbf{D}||^{-1/2} \int \left(\frac{\partial \boldsymbol{\mu}}{\partial \mathbf{r}} (\boldsymbol{\gamma} + \mathbf{r})\right) \mathbf{M}^{-1/2} \tilde{\mathbf{U}} \exp\left\{-\frac{1}{2}\mathbf{r}^{\mathrm{T}}\mathbf{D}^{-1}\mathbf{r}\right\} d^{3N}\mathbf{r} \\
&= ||2\pi \mathbf{D}||^{-1/2} \int \boldsymbol{\mu}(\boldsymbol{\gamma} + \mathbf{r}) \mathbf{r}^{\mathrm{T}}\mathbf{D}^{-1}\mathbf{M}^{-1/2} \tilde{\mathbf{U}} \exp\left\{-\frac{1}{2}\mathbf{r}^{\mathrm{T}}\mathbf{D}^{-1}\mathbf{r}\right\} d^{3N}\mathbf{r} \\
&= \left\langle \boldsymbol{\mu}\mathbf{r}^{\mathrm{T}} \right\rangle \mathbf{D}^{-1}\mathbf{M}^{-1/2} \tilde{\mathbf{U}} \ .
\end{aligned} \tag{8.6}$$

Note the contrast to approaches which compute the dipole moment autocorrelation function, and produce a line spectrum from its Fourier transform. Note also that SCP does not provide any information on the broadenings of the peaks.

8.1.2 Replica-exchange path integral molecular dynamics

The replica-exchange (RE) method [125–127] can be combined with either path integral (PI) Monte Carlo (MC) or molecular dynamics (MD) simulations in order to overcome the problem of "broken ergodicity", i.e., the effective inability of a simulation to sample minima of the PES which are separated by large barriers. Multiple "replicas" of the system are initialized and maintained over a ladder of fixed temperatures $T_1 < \ldots < T_N$. PIMC or PIMD is carried out for each replica simultaneously, and replicas at two adjacent inverse temperatures β_i, β_{i+1} on the ladder are allowed to periodically swap coordinates with acceptance probability

$$P_{\mathrm{swap}} = \min[1, \exp\left\{(\beta_{i+1} - \beta_i)(U(\mathbf{r}_{i+1}) - U(\mathbf{r}_i))\right\}] \,, \qquad (8.7)$$

thereby coupling all replicas over the ladder while ensuring that detailed balance is satisfied. In this manner, the ergodicity of the high-temperature replicas in an RE-PIMD simulation makes all of the molecular dynamics trajectories ergodic. Given the equilibrium populations of two isomers, P_A and P_B, at some temperature T obtained from an RE-PIMD simulation, the free energy difference at this temperature can be determined using

$$\Delta F = F_A - F_B = -k_{\mathrm{B}} T \log \frac{P_A}{P_B} \,, \qquad (8.8)$$

although in this work we are concerned primarily with the relative populations of the various isomers.

8.2 Zero-temperature and temperature-dependent vibrational spectra for water hexamer

Vibrational spectra for several low-lying isomers of water hexamer at $T = 0\,\text{K}$ using the MB-pol potential and corresponding MB-μ dipole moment surface are presented in Fig. 8.1. From the individual water hexamer spectra, several "composite" or "weighted" spectra were generated at finite-temperature using the relative populations of each isomer/isotopomer determined by Goetz and Paesani [124] from RE-PIMD simulations. All SCP spectra were computed at zero-temperature, with the temperature-dependence arising from the changing RE-PIMD conditions/populations, with the understanding that the SCP bending and stretching frequencies do not change too dramatically with temperature compared to the changes in the relative populations of the isomers considered. Similar protocol can be found in, e.g., Ref. 112. SCP spectra for $T > 0\,\text{K}$ can be computed in the future and combined in the same way, with additional computer time being the only additional requirement. Again, all spectra have been artificially broadened, as SCP provides no information regarding broadening of the peaks. Experimental IR spectra for the hexamer can be found in Ref. 128.

Figure 8.1: Vibrational spectra computed using SCP combined with the MB-pol potential and corresponding MB-μ dipole moment surface for several low-lying isomers of water hexamer at zero-temperature.

(H₂O)₆ book

(D₂O)₆ book

Wavenumber (cm⁻¹)

(H₂O)₆ double tetramer

(D₂O)₆ double tetramer

Wavenumber (cm⁻¹)

(H$_2$O)$_6$ prism-book

(D$_2$O)$_6$ prism-book

Wavenumber (cm^{-1})

(H$_2$O)$_6$ cyclic chair

(D$_2$O)$_6$ cyclic chair

Wavenumber (cm^{-1})

$(H_2O)_6$ bag

$(D_2O)_6$ bag

Wavenumber (cm^{-1})

$(H_2O)_6$ pentamer down-plus-one

$(D_2O)_6$ pentamer down-plus-one

Wavenumber (cm^{-1})
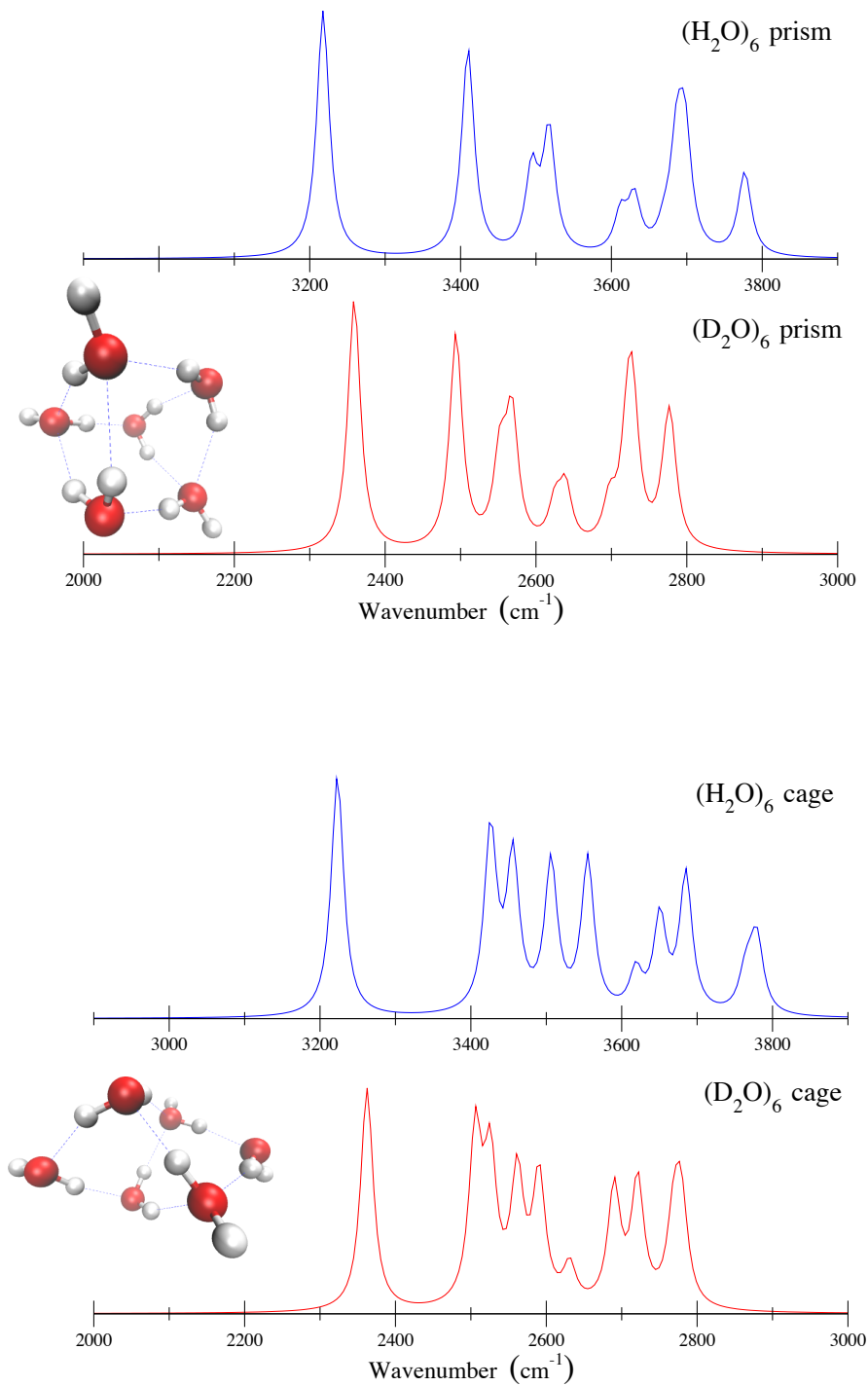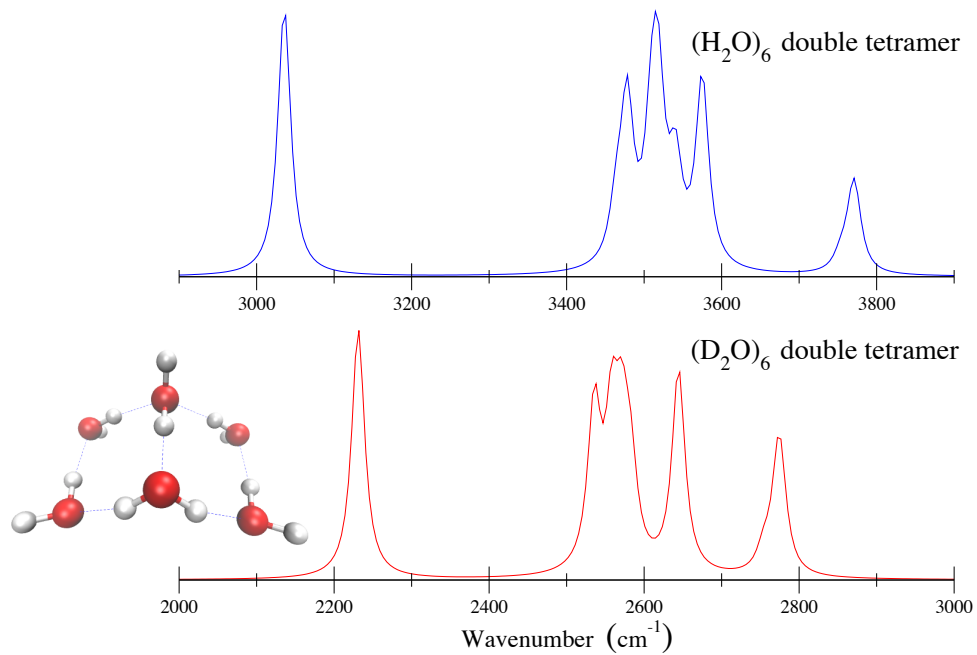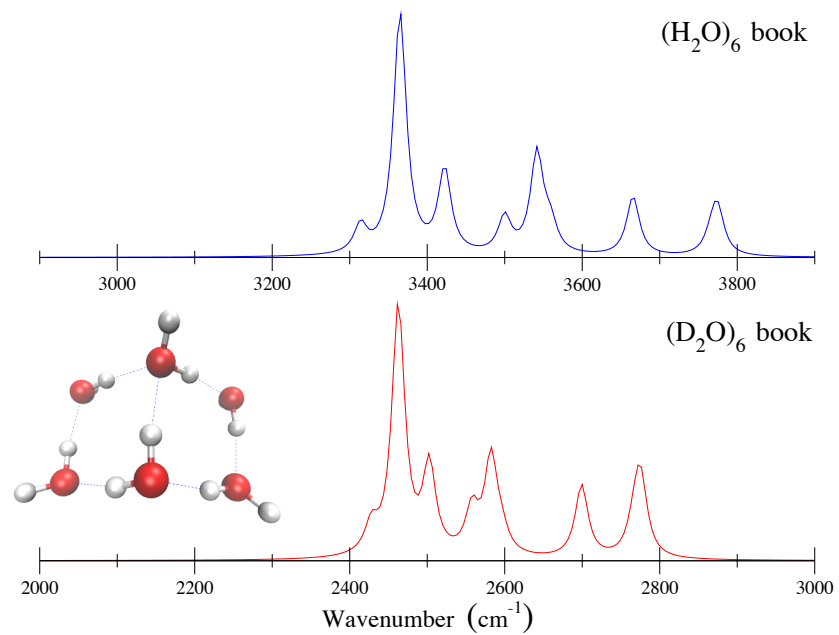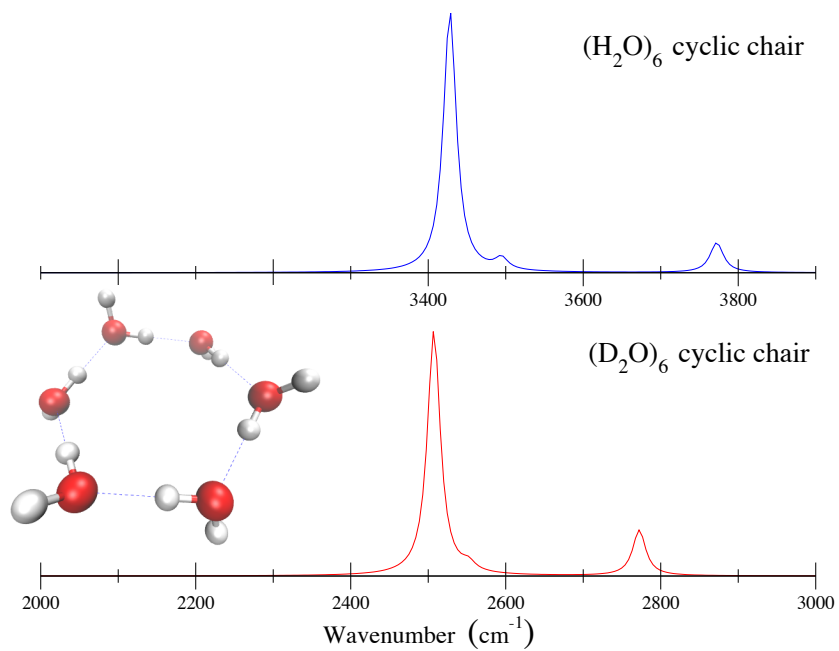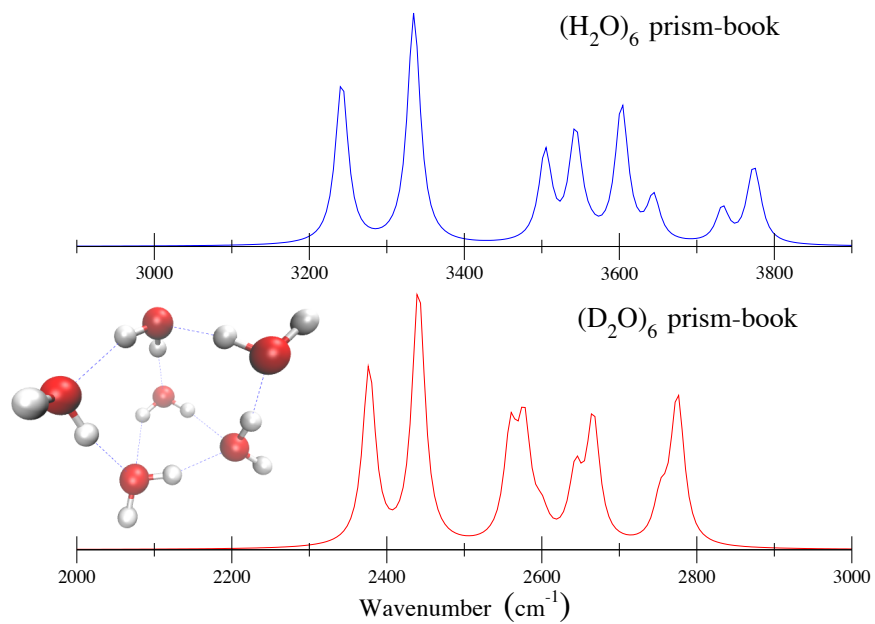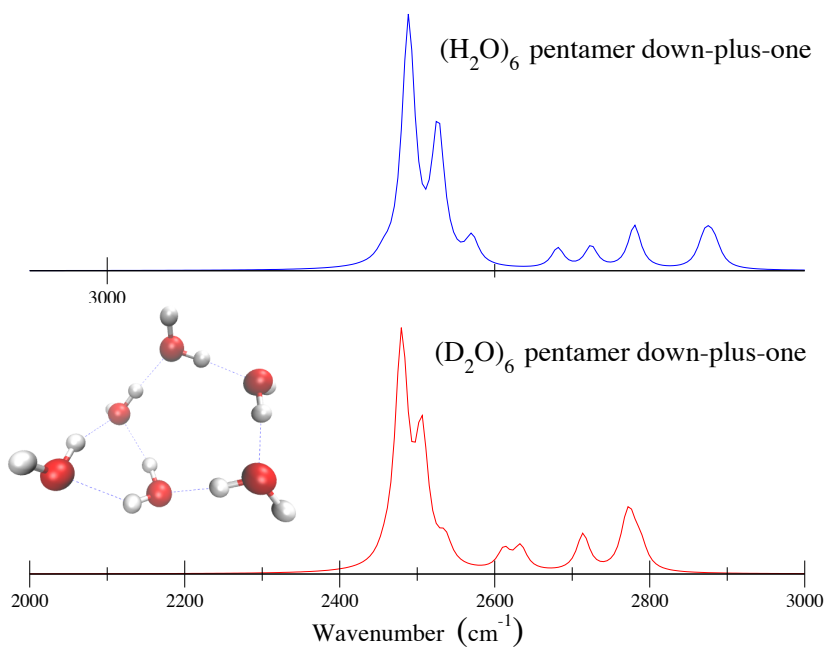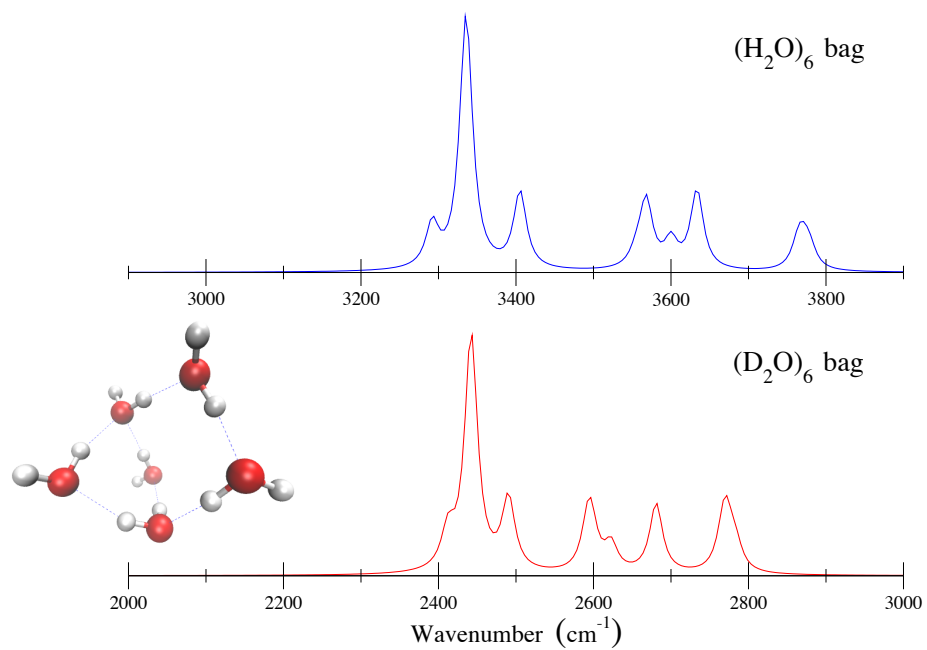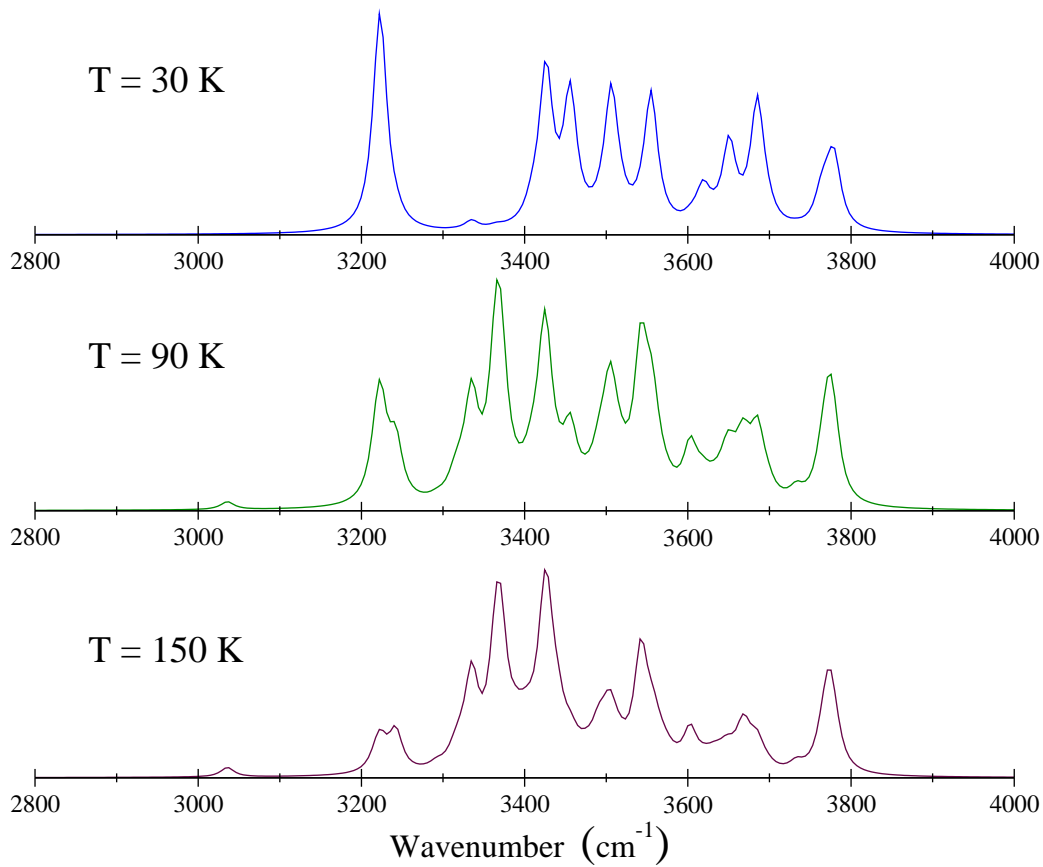
Figure 8.2: Temperature-dependent vibrational spectra for $(H_2O)_6$ composed of SCP spectra for individual low-lying isomers at zero-temperature, weighted according to the relative populations determined from replica-exchange path integral molecular dynamics at each temperature [124].

8.3 Zero-temperature vibrational frequencies for water 20-mer

Vibrational frequencies computed using the standard harmonic approximation (HA) and SCP for several low-lying isomers of $(H_2O)_{20}$ and their deuterated isotopomers, $(D_2O)_{20}$, at zero-temperature using the MB-pol PES are shown in Fig. 8.4. The corresponding structures are shown in Fig. 8.3. Note that scaling the HA frequencies by the commonly used *ad hoc* scaling factor of 0.95 (not shown) gives general agreement with the SCP frequencies. However, disagreement between the scaled HA frequencies and SCP frequencies grows as we move toward the lower frequency stretching modes, and especially the bending modes, suggesting, as one should expect, that the use of such scaling factors is inadequate for accounting for anharmonic effects in the spectra of water clusters.

8.4 Closing remarks

The SCP method's unique ability to efficiently compute temperature-dependent, anharmonic frequencies while avoiding *ad hoc* procedures such as scaling harmonic frequencies or freezing out any degrees of freedom (as done, for example, in Ref. 108), and without producing unphysical artifacts, makes it a natural choice for treating relatively large quantum systems. Through the calculation of vibrational/IR spectra, SCP could be used to study, e.g., how solvation properties (which, unsurprisingly,
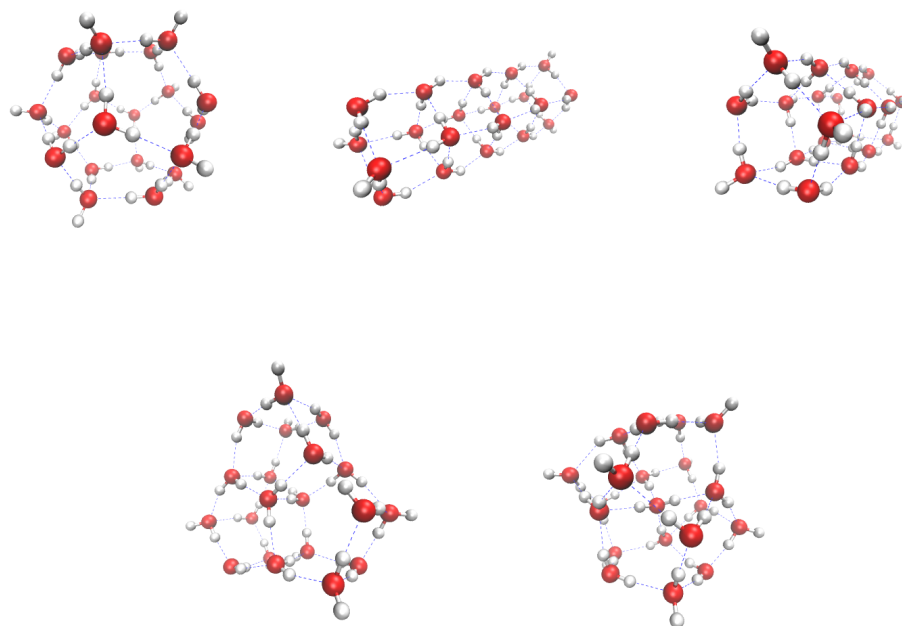
Figure 8.3: Several low-lying isomers of $(H_2O)_{20}$ for the MB-pol potential. Top row, from left to right: "dodecahedron", "fused cubes", and "face-sharing pentagonal prism". Bottom row, left to right: "edge-sharing pentagonal prism 1" and "edge-sharing pentagonal prism 2"
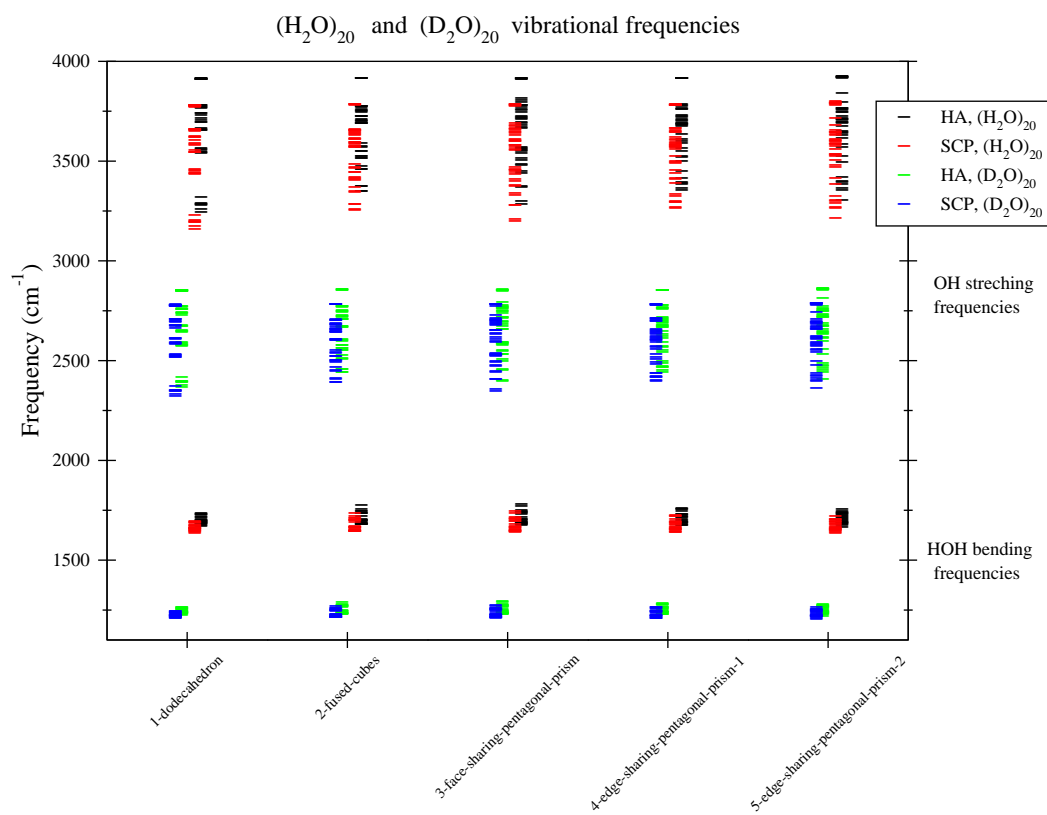
Figure 8.4: Vibrational frequencies computed using the standard harmonic approximation (HA) and self-consistent phonons (SCP) method for several low-lying isomers of $(H_2O)_{20}$ and their deuterated isotopomers, $(D_2O)_{20}$, at zero-temperature using the MB-pol potential.

are also strongly subject to nuclear quantum effects [129, 130]) evolve as a function of temperature and cluster size from small complexes to bulk solutions. SCP's comparatively low computational cost makes it possible to investigate larger systems with highly accurate potentials, such as the *ab initio*-based MB-pol and i-TTM potentials. Even for the case of water clusters, for which we have seen in Chapter 7 that SCP is not able to adequately capture the anharmonicity of the low-frequency intermolecular modes, higher frequencies corresponding to stretch and bend do appear to be sufficiently accurate for generating reliable spectra in this region, as evidenced by their general agreement with scaled or shifted harmonic spectra in this range.

Appendix A

Jensen's and Gibbs' Inequalities

Let X be a discrete random variable with probability mass function p_X. Jensen's inequality states that for any real, continuous, convex function $g(x)$,

$$g\left(\sum_k x_k p_k\right) \leq \sum_k g(x_k) p_k . \tag{A.1}$$

Additionally, since $h(x) := -g(x)$ must be concave, we have that

$$h\left(\sum_k x_k p_k\right) \geq \sum_k h(x_k) p_k \tag{A.2}$$

for any real, continuous, concave function $h(x)$. This can be extended naturally to the continuous case, where X is a continuous random variable having probability density function f_X:

$$g\left(\int x f(x)\, dx\right) \leq \int g(x) f(x)\, dx . \tag{A.3}$$

In any case, for a random variable X and convex function $g(x)$, Jensen's inequality amounts to

$$g\left(\mathbb{E}[X]\right) \leq \mathbb{E}\left[g(X)\right] . \tag{A.4}$$

Several general proofs of Jensen's inequality exist, but for simplicity, we consider the special case most relevant to this work, $g(x) := e^x$. Expressing the expectation value as a product

$$\mathbb{E}\left[e^X\right] = \mathbb{E}\left[e^X e^{\mathbb{E}(X)} e^{-\mathbb{E}(X)}\right] = e^{\mathbb{E}(X)} \mathbb{E}\left[e^{X-\mathbb{E}(X)}\right] \ ,$$

and applying the elementary inequality

$$e^x \geq 1 + x \ , \quad x \in \mathbb{R}$$

to the second factor, we have that

$$\mathbb{E}\left[e^X\right] = e^{\mathbb{E}(X)} \mathbb{E}\left[e^{X-\mathbb{E}(X)}\right] \geq e^{\mathbb{E}(X)} \mathbb{E}\left[1 + X - \mathbb{E}(X)\right] = e^{\mathbb{E}(X)} \ .$$

By definition, the Kullback-Leibler divergence from $\mathcal{P}$ to $\mathcal{P}_0$ is

$$D(\mathcal{P}_0 || \mathcal{P}) = \mathbb{E}_0\left[\log \frac{\mathcal{P}_0}{\mathcal{P}}\right] \ .$$

Noting that the logarithm function is concave and applying Jensen's inequality, we obtain Gibbs' inequality:

$$D(\mathcal{P}_0 || \mathcal{P}) = \mathbb{E}_0\left[\log \frac{\mathcal{P}_0}{\mathcal{P}}\right] \geq \log\left(\mathbb{E}_0\left[\frac{\mathcal{P}_0}{\mathcal{P}}\right]\right) = 0 \ .$$

Bibliography

[1] Berhane Temelso and George C. Shields. The Role of Anharmonicity in Hydrogen-Bonded Systems: The Case of Water Clusters. *Journal of Chemical Theory and Computation*, 7(9):2804–2817, 2011.

[2] Vladimir A. Sharapov and Vladimir A. Mandelshtam. Solid-Solid Structural Transformations in Lennard-Jones Clusters: Accurate Simulations versus the Harmonic Superposition Approximation. *The Journal of Physical Chemistry A*, 111(41):10284–10291, 2007.

[3] James B. Anderson. A random-walk simulation of the Schrödinger equation: $H_+{}^3$. *The Journal of Chemical Physics*, 63(4):1499–1503, 1975.

[4] James B. Anderson. Quantum chemistry by random walk. H ^2P, H_3^+ D_{3h} $^1A_1'$, H_2 $^3\Sigma_u^+$, H_4 $^1\Sigma_g^+$, Be ^1S. *The Journal of Chemical Physics*, 65(10):4121–4127, 1976.

[5] A. Sarsa, K. E. Schmidt, and W. R. Magro. A path integral ground state method. *The Journal of Chemical Physics*, 113(4):1366–1371, 2000.

[6] Jianshu Cao and Gregory A. Voth. A new perspective on quantum time correlation functions. *The Journal of Chemical Physics*, 99(12):10070–10073, 1993.

[7] Ian R. Craig and David E. Manolopoulos. Quantum statistics and classical mechanics: Real time correlation functions from ring polymer molecular dynamics. *The Journal of Chemical Physics*, 121(8):3368–3373, 2004.

[8] Bastiaan J. Braams and David E. Manolopoulos. On the short-time limit of ring polymer molecular dynamics. *The Journal of Chemical Physics*, 125(12):124105, 2006.

[9] F. Calvo, J. P. K. Doye, and D. J. Wales. Characterization of anharmonicities on complex potential energy surfaces: Perturbation theory and simulation. *The Journal of Chemical Physics*, 115(21):9627–9636, 2001.

[10] R. A. Buckingham. The classical equation of state of gaseous helium, neon and argon. *Proceedings of the Royal Society of London A: Mathematical, Physical and Engineering Sciences*, 168(933):264–283, 1938.

[11] B. Pietrass. Equation of state and interatomic potential of liquid argon and neon. *Physica*, 42:147–155, April 1969.

[12] R. Ramírez, C. P. Herrero, A. Antonelli, and E. R. Hernández. Path integral calculation of free energies: Quantum effects on the melting temperature of neon. *The Journal of Chemical Physics*, 129(6):11, 2008.

[13] E. A. Guggenheim. The Principle of Corresponding States. *The Journal of Chemical Physics*, 13(7):253–261, 1945.

[14] J. de Boer. Quantum theory of condensed permanent gases I: The law of corresponding states. *Physica*, 14:139–148, April 1948.

[15] Qinyu Wang and J Karl Johnson. Phase equilibrium of quantum fluids from simulation: Hydrogen and neon. *Fluid Phase Equilibria*, 132(1):93 – 116, 1997.

[16] Ionuţ Georgescu, Sandra E. Brown, and Vladimir A. Mandelshtam. Mapping the phase diagram for neon to a quantum Lennard-Jones fluid using Gibbs ensemble simulations. *The Journal of Chemical Physics*, 138(13):134502, 2013.

[17] Daan Frenkel and Berend Smit. *Understanding Molecular Simulation*, volume 1 of *Computational Science Series*. Academic Press, second edition, 2002.

[18] Athanassios Z. Panagiotopoulos. Direct determination of phase coexistence properties of fluids by Monte Carlo simulation in a new ensemble. *Molecular Physics*, 61(4):813–826, 1987.

[19] A. Z. Panagiotopoulos, N. Quirke, M. Stapleton, and D. J. Tildesley. Phase equilibria by simulation in the Gibbs ensemble. *Molecular Physics*, 63(4):527–545, 1988.

[20] B. Smit, Ph. De Smedt, and D. Frenkel. Computer simulations in the Gibbs ensemble. *Molecular Physics*, 68(4):931–950, 1989.

[21] Pavel A. Frantsuzov and Vladimir A. Mandelshtam. Quantum statistical mechanics with Gaussians: Equilibrium properties of van der Waals clusters. *The Journal of Chemical Physics*, 121(19):9247–9256, 2004.

[22] John P. Valleau. Number-dependence concerns in Gibbs-ensemble Monte Carlo. *The Journal of Chemical Physics*, 108(7):2962–2966, 1998.

[23] John P. Valleau. A Thermodynamic-scaling Study of Gibbs-ensemble Monte Carlo. *Molecular Simulation*, 29(10-11):627–642, 2003.

[24] E. W. Lemmon, M. O. McLinden, and D. G. Friend. Thermophysical properties of fluid systems. *NIST chemistry webbook, NIST standard reference database*, 69, 2005.

[25] A. Z. Panagiotopoulos. Molecular simulation of phase coexistence: Finite-size effects and determination of critical parameters for two- and three-dimensional Lennard-Jones fluids. *International Journal of Thermophysics*, 15(6):1057–1072, 1994.

[26] K. Binder and E. Luijten. Monte Carlo tests of renormalization group predictions for critical phenomena in Ising models. *Phys. Rept.*, 344:179–253, 2001.

[27] J. S. Rowlinson and F. L. Swinton. *Liquids and Liquid Mixtures*. Butterworths Monographs in Chemistry. Butterworth-Heinemann, third edition, 1982.

[28] Jianshu Cao and Gregory A. Voth. Modeling physical systems by effective harmonic oscillators: The optimized quadratic approximation. *The Journal of Chemical Physics*, 102(8):3337–3348, 1995.

[29] Thomas R. Koehler. Theory of the Self-Consistent Harmonic Approximation with Application to Solid Neon. *Phys. Rev. Lett.*, 17:89–91, Jul 1966.

[30] N. S. Gillis, N. R. Werthamer, and T. R. Koehler. Properties of Crystalline Argon and Neon in the Self-Consistent Phonon Approximation. *Phys. Rev.*, 165:951–959, Jan 1968.

[31] F. Calvo, P. Parneix, and N.-T. Van-Oanh. Finite-temperature infrared spectroscopy of polycyclic aromatic hydrocarbon molecules. II. Principal mode analysis and self-consistent phonons. *The Journal of Chemical Physics*, 133(7):074303, 2010.

[32] Ionuţ Georgescu and Vladimir A. Mandelshtam. A fast variational gaussian wavepacket method: Size-induced structural transitions in large neon clusters. *The Journal of Chemical Physics*, 135(15):154106, 2011.

[33] Ionuţ Georgescu and Vladimir A. Mandelshtam. Self-consistent phonons revisited. I. The role of thermal versus quantum fluctuations on structural transitions in large Lennard-Jones clusters. *The Journal of Chemical Physics*, 137(14):144106, 2012.

[34] Sandra E. Brown and Vladimir A. Mandelshtam. Self-consistent phonons: An accurate and practical method to account for anharmonic effects in equilibrium properties of general classical or quantum many-body systems. *Chemical Physics*, 2016. Available online: http://dx.doi.org/10.1016/j.chemphys.2016.06.008.

[35] F. Calvo, J. P. K. Doye, and D. J. Wales. Quantum partition functions from classical distributions: Application to rare-gas clusters. *The Journal of Chemical Physics*, 114(17):7312–7329, 2001.

[36] Pieter-Tjerk de Boer, Dirk P. Kroese, Shie Mannor, and Reuven Y. Rubinstein. A Tutorial on the Cross-Entropy Method. *Annals of Operations Research*, 134(1):19–67, 2005.

[37] Aviel Chaimovich and M. Scott Shell. Anomalous waterlike behavior in spherically-symmetric water models optimized with the relative entropy. *Phys. Chem. Chem. Phys.*, 11:1901–1915, 2009.

[38] Scott P. Carmichael and M. Scott Shell. A New Multiscale Algorithm and Its Application to Coarse-Grained Peptide Models for Self-Assembly. *The Journal of Physical Chemistry B*, 116(29):8383–8393, 2012.

[39] David J. Wales. *Energy Landscapes*. Cambridge University Press, 2003.

[40] Rudolf Schürer. A comparison between (quasi-)Monte Carlo and cubature rule based methods for solving high-dimensional integration problems. *Math. Comput. Simul.*, 62(3-6):509–517, March 2003.

[41] Harald Niederreiter. *Random Number Generation and Quasi-Monte Carlo Methods*. Society for Industrial and Applied Mathematics, Philadelphia, PA, USA, 1992.

[42] Harald Niederreiter. Quasi-Monte Carlo methods and pseudo-random numbers. *Bulletin of the American Mathematical Society*, 84(6):957–1041, 1978.

[43] William J. Morokoff and Russel E. Caflisch. Quasi-Monte Carlo Integration. *Journal of Computational Physics*, 122(2):218 – 230, 1995.

[44] John H. Halton. On the efficiency of certian quasi-random sequences of points in evaluating multi-dimensional integrals. *Numerische Mathematik*, 2:84–90, 1960.

[45] I. M. Sobol. On the distribution of points in a cube and the approximate evaluation of integrals. *USSR Computational Mathematics and Mathematical Physics*, 7(4):86 – 112, 1967.

[46] I. M. Sobol. Uniformly distributed sequences with an additional uniform property. *USSR Computational Mathematics and Mathematical Physics*, 16(5):236 – 242, 1976.

[47] Henri Faure. Discrépance de suites associées à un système de numération (en dimension s). *Acta Arithmetica*, 41:337–351, 1982.

[48] Harald Niederreiter. Point Sets and Sequences with Small Discrepancy. *Monatshefte für Mathematik*, 104:273–337, 1987.

[49] W. Morokoff and R. Caflisch. Quasi-Random Sequences and Their Discrepancies. *SIAM Journal on Scientific Computing*, 15(6):1251–1279, 1994.

[50] Stephen Joe and Frances Y. Kuo. Remark on Algorithm 659: Implementing Sobol's Quasirandom Sequence Generator. *ACM Trans. Math. Softw.*, 29(1):49–57, March 2003.

[51] Paul Bratley and Bennett L. Fox. Algorithm 659: Implementing Sobol's Quasirandom Sequence Generator. *ACM Trans. Math. Softw.*, 14(1):88–100, March 1988.

[52] I. A. Antonov and V. M. Saleev. An economic method of computing LP_τ-sequences. *USSR Computational Mathematics and Mathematical Physics*, 19(1):252 – 256, 1979.

[53] Luc Devroye. *Non-Uniform Random Variate Generation.* Springer-Verlag, 1986.

[54] J. D. Beasley and S. G. Springer. Algorithm AS 111: The Percentage Points of the Normal Distribution. *Journal of the Royal Statistical Society. Series C (Applied Statistics)*, 26(1):pp. 118–121, 1977.

[55] Boris Moro. The Full Monte. *Risk Magazine*, 8(2):57–58, 1995.

[56] Tim Pillards and Ronald Cools. Using Box-Muller with Low Discrepancy Points. In Marina Gavrilova, Osvaldo Gervasi, Vipin Kumar, C. Tan, David Taniar, Antonio Laganá, Youngsong Mun, and Hyunseung Choo, editors, *Computational Science and Its Applications - ICCSA 2006*, volume 3984 of *Lecture Notes in Computer Science*, pages 780–788. Springer Berlin / Heidelberg, 2006.

[57] Sandra E. Brown, Ionuţ Georgescu, and Vladimir A. Mandelshtam. Self-consistent phonons revisited. II. A general and efficient method for computing free energies and vibrational spectra of molecules and clusters. *The Journal of Chemical Physics*, 138(4):044317, 2013.

[58] Nguyen-Thi Van-Oanh, Pascal Parneix, and Philippe Bréchignac. Vibrational Dynamics of the Neutral Naphthalene Molecule from a Tight-Binding Approach. *The Journal of Physical Chemistry A*, 106(43):10144–10151, 2002.

[59] R. Nathaniel Pribble and Timothy S. Zwier. Size-Specific Infrared Spectra of Benzene-$(H_2O)_n$ Clusters ($n = 1$ through 7): Evidence for Noncyclic $(H_2O)_n$ Structures. *Science*, 265(5168):75–79, 07 1994.

[60] K. Liu, M. G. Brown, C. Carter, R. J. Saykally, J. K. Gregory, and D. C. Clary. Characterization of a cage form of the water hexamer. *Nature*, 381:501–503, 06 1996.

[61] Eugene S. Kryachko. Ab initio studies of the conformations of water hexamer: modelling the penta-coordinated hydrogen-bonded pattern in liquid water. *Chemical Physics Letters*, 314(3–4):353 – 363, 1999.

[62] K. Nauta and R. E. Miller. Formation of Cyclic Water Hexamer in Liquid Helium: The Smallest Piece of Ice. *Science*, 287(5451):293–295, 2000.

[63] Martin Losada and Samuel Leutwyler. Water hexamer clusters: Structures, energies, and predicted mid-infrared spectra. *The Journal of Chemical Physics*, 117(5):2003–2016, 2002.

[64] C. Steinbach, P. Andersson, M. Melzer, J. K. Kazimirski, U. Buck, and V. Buch. Detection of the book isomer from the OH-stretch spectroscopy of size selected water hexamers. *Phys. Chem. Chem. Phys.*, 6:3320–3324, 2004.

[65] Meghan E. Dunn, Emma K. Pokon, and George C. Shields. Thermodynamics of Forming Water Clusters at Various Temperatures and Pressures by Gaussian-2, Gaussian-3, Complete Basis Set-QB3, and Complete Basis Set-APNO Model

Chemistries; Implications for Atmospheric Chemistry. *Journal of the American Chemical Society*, 126(8):2647–2653, 2004.

[66] Erin E. Dahlke, Ryan M. Olson, Hannah R. Leverentz, and Donald G. Truhlar. Assessment of the Accuracy of Density Functionals for Prediction of Relative Energies and Geometries of Low-Lying Isomers of Water Hexamers. *The Journal of Physical Chemistry A*, 112(17):3976–3984, 2008.

[67] Desiree M. Bates and Gregory S. Tschumper. CCSD(T) Complete Basis Set Limit Relative Energies for Low-Lying Water Hexamer Structures. *The Journal of Physical Chemistry A*, 113(15):3555–3559, 2009.

[68] Yimin Wang, Xinchuan Huang, Benjamin C. Shepler, Bastiaan J. Braams, and Joel M. Bowman. Flexible, *ab initio* potential, and dipole moment surfaces for water. I. Tests and applications for clusters up to the 22-mer. *The Journal of Chemical Physics*, 134(9):094509, 2011.

[69] Yimin Wang and Joel M. Bowman. *Ab initio* potential and dipole moment surfaces for water. II. Local-monomer calculations of the infrared spectra of water clusters. *The Journal of Chemical Physics*, 134(15), 2011.

[70] Cristóbal Pérez, Matt T. Muckle, Daniel P. Zaleski, Nathan A. Seifert, Berhane Temelso, George C. Shields, Zbigniew Kisiel, and Brooks H. Pate. Structures of Cage, Prism, and Book Isomers of Water Hexamer from Broadband Rotational Spectroscopy. *Science*, 336(6083):897–901, 2012.

[71] Yimin Wang, Volodymyr Babin, Joel M. Bowman, and Francesco Paesani. The Water Hexamer: Cage, Prism, or Both. Full Dimensional Quantum Simulations Say Both. *Journal of the American Chemical Society*, 134(27):11116–11119, 2012.

[72] Richard J. Saykally and David J. Wales. Pinning Down the Water Hexamer. *Science*, 336(6083):814–815, 2012.

[73] Joel D. Mallory, Sandra E. Brown, and Vladimir A. Mandelshtam. Assessing the Performance of the Diffusion Monte Carlo Method As Applied to the Water Monomer, Dimer, and Hexamer. *The Journal of Physical Chemistry A*, 119(24):6504–6515, 2015.

[74] Jeremy O. Richardson, Cristóbal Pérez, Simon Lobsiger, Adam A. Reid, Berhane Temelso, George C. Shields, Zbigniew Kisiel, David J. Wales, Brooks H. Pate, and Stuart C. Althorpe. Concerted hydrogen-bond breaking by quantum tunneling in the water hexamer prism. *Science*, 351(6279):1310–1313, 2016.

[75] Joel D. Mallory and Vladimir A. Mandelshtam. Diffusion Monte Carlo studies of MB-pol $(H_2O)_{2-6}$ and $(D_2O)_{2-6}$ clusters: Structures and binding energies. *The Journal of Chemical Physics*, 145(6):10, 2016.

[76] Volodymyr Babin, Claude Leforestier, and Francesco Paesani. Development of a "First Principles" Water Potential with Flexible Monomers: Dimer Potential Energy Surface, VRT Spectrum, and Second Virial Coefficient. *Journal of Chemical Theory and Computation*, 9(12):5395–5403, 2013.

[77] Volodymyr Babin, Gregory R. Medders, and Francesco Paesani. Development of a "First Principles" Water Potential with Flexible Monomers. II: Trimer Potential Energy Surface, Third Virial Coefficient, and Small Clusters. *Journal of Chemical Theory and Computation*, 10(4):1599–1607, 2014.

[78] Gregory R. Medders, Volodymyr Babin, and Francesco Paesani. Development of a "First-Principles" Water Potential with Flexible Monomers. III. Liquid Phase Properties. *Journal of Chemical Theory and Computation*, 10(8):2906–2910, 2014.

[79] Scott Habershon, Thomas E. Markland, and David E. Manolopoulos. Competing quantum effects in the dynamics of a flexible water model. *The Journal of Chemical Physics*, 131(2):024501, 2009.

[80] Joel M. Bowman. Private communication.

[81] Ionuţ Georgescu, Svetlana Jitomirskaya, and Vladimir A. Mandelshtam. On the ground state calculation of a many-body system using a self-consistent basis and quasi-Monte Carlo: An application to water hexamer. *The Journal of Chemical Physics*, 139(20):204104, 2013.

[82] Pavel Frantsuzov, Arnold Neumaier, and Vladimir A. Mandelshtam. Gaussian resolutions for equilibrium density matrices. *Chemical Physics Letters*, 381(1–2):117 – 122, 2003.

[83] Cristian Predescu, Pavel A. Frantsuzov, and Vladimir A. Mandelshtam. Thermodynamics and equilibrium structure of Ne_{38} cluster: Quantum mechanics versus classical. *The Journal of Chemical Physics*, 122(15), 2005.

[84] J. A. Northby. Structure and binding of Lennard-Jones clusters: $13 \leq N \leq 147$. *The Journal of Chemical Physics*, 87(10):6166–6177, 1987.

[85] Jonathan P. K. Doye and David J. Wales. Calculation of thermodynamic properties of small Lennard-Jones clusters incorporating anharmonicity. *The Journal of Chemical Physics*, 102(24):9659–9672, 1995.

[86] Charusita Chakravarty. Quantum delocalization and cluster melting. *The Journal of Chemical Physics*, 103(24):10663–10668, 1995.

[87] Robert H. Leary. Global Optima of Lennard-Jones Clusters. *Journal of Global Optimization*, 11(1):35–53, 1997.

[88] J. P. Neirotti, F. Calvo, David L. Freeman, and J. D. Doll. Phase changes in 38-atom Lennard-Jones clusters. I. A parallel tempering study in the canonical ensemble. *The Journal of Chemical Physics*, 112(23):10340–10349, 2000.

[89] F. Calvo, J. P. Neirotti, David L. Freeman, and J. D. Doll. Phase changes in 38-atom Lennard-Jones clusters. II. A parallel tempering study of equilibrium and dynamic properties in the molecular dynamics and microcanonical ensembles. *The Journal of Chemical Physics*, 112(23):10350–10357, 2000.

[90] Jonathan P. K. Doye and Florent Calvo. Entropic effects on the structure of Lennard-Jones clusters. *The Journal of Chemical Physics*, 116(19):8307–8317, 2002.

[91] Vladimir A. Mandelshtam and Pavel A. Frantsuzov. Multiple structural transformations in Lennard-Jones clusters: Generic versus size-specific behavior. *The Journal of Chemical Physics*, 124(20), 2006.

[92] Jason Deckman and Vladimir A. Mandelshtam. Effects of Quantum Delocalization on Structural Changes in Lennard-Jones Clusters. *The Journal of Physical Chemistry A*, 113(26):7394–7402, 2009.

[93] N. Corbin and K. Singer. Semiclassical molecular dynamics of wave packets. *Molecular Physics*, 46(3):671–677, 1982.

[94] D. J. Wales, J. P. K. Doye, A. Dullweber, M. P. Hodges, F. Y. Naumkin, F. Calvo, J. Hernández-Rojas, and T. F. Middleton. The Cambridge Cluster Database. http://www-wales.ch.cam.ac.uk/CCD.html.

[95] Victoria Buch. Exploration of multidimensional variational Gaussian wave packets as a simulation tool. *The Journal of Chemical Physics*, 117(10):4738–4750, 2002.

[96] Peter Kollman. Free Energy Calculations: Applications to Chemical and Biochemical Phenomena. *Chemical Reviews*, 93(7):2395–2417, 1993.

[97] William P. Reinhardt, Mark A. Miller, and Lynn M. Amon. Why Is It so Difficult To Simulate Entropies, Free Energies, and Their Differences? *Accounts of Chemical Research*, 34(7):607–614, 2001.

[98] Tetyana V. Bogdan, David J. Wales, and Florent Calvo. Equilibrium thermodynamics from basin-sampling. *The Journal of Chemical Physics*, 124(4):13, 2006.

[99] Volodymyr Babin and Francesco Paesani. The curious case of the water hexamer: Cage vs. Prism. *Chemical Physics Letters*, 580:1 – 8, 2013.

[100] Maurice de Koning, A. Antonelli, and Sidney Yip. Optimized Free-Energy Evaluation Using a Single Reversible-Scaling Simulation. *Phys. Rev. Lett.*, 83:3973–3977, Nov 1999.

[101] Maurice de Koning, Wei Cai, Alex Antonelli, and Sidney Yip. Efficient Free-Energy Calculations by the Simulation of Nonequilibrium Processes. *Computing in Science and Engineering*, 2(3):88–96, May 2000.

[102] L. M. Amon and W. P. Reinhardt. Development of reference states for use in absolute free energy calculations of atomic clusters with application to 55-atom Lennard-Jones clusters in the solid and liquid states. *The Journal of Chemical Physics*, 113(9):3573–3590, 2000.

[103] Donald A. McQuarrie. *Statistical Mechanics.* University Science Books, 2000.

[104] Paul J. Steinhardt, David R. Nelson, and Marco Ronchetti. Bond-orientational order in liquids and glasses. *Phys. Rev. B*, 28:784–805, Jul 1983.

[105] Gregory R. Medders, Volodymyr Babin, and Francesco Paesani. A Critical Assessment of Two-Body and Three-Body Interactions in Water. *Journal of Chemical Theory and Computation*, 9(2):1103–1114, 2013.

[106] Arnold Neumaier and Vladimir A. Mandelshtam. Private communication.

[107] Christoph C. Pradzynski, Christoph W. Dierking, Florian Zurheide, Richard M. Forck, Udo Buck, Thomas Zeuch, and Sotiris S. Xantheas. Infrared detection of $(h_2o)_{20}$ isomers of exceptional stability: a drop-like and a face-sharing pentagonal prism cluster. *Phys. Chem. Chem. Phys.*, 16:26691–26696, 2014.

[108] Conrad T. Wolke, Fabian S. Menges, Niklas Tötsch, Olga Gorlova, Joseph A. Fournier, Gary H. Weddle, Mark A. Johnson, Nadja Heine, Tim K. Esser, Harald Knorke, Knut R. Asmis, Anne B. McCoy, Daniel J. Arismendi-Arrieta, Rita Prosmiti, and Francesco Paesani. Thermodynamics of Water Dimer Dissociation in the Primary Hydration Shell of the Iodide Ion with Temperature-Dependent Vibrational Predissociation Spectroscopy. *The Journal of Physical Chemistry A*, 119(10):1859–1866, 2015.

[109] Jonathon K. Gregory and David C. Clary. Structure of Water Clusters. The Contribution of Many-Body Forces, Monomer Relaxation, and Vibrational Zero-Point Energy. *The Journal of Physical Chemistry*, 100(46):18014–18022, 1996.

[110] Sotiris S. Xantheas, Christian J. Burnham, and Robert J. Harrison. Development of transferable interaction models for water. II. Accurate energetics of the first few water clusters from first principles. *The Journal of Chemical Physics*, 116(4):1493–1499, 2002.

[111] Richard J. Saykally and David J. Wales. Pinning Down the Water Hexamer. *Science*, 336(6083):814–815, 2012.

[112] C. J. Tainter and J. L. Skinner. The water hexamer: Three-body interactions, structures, energetics, and OH-stretch spectroscopy at finite temperature. *The Journal of Chemical Physics*, 137(10), 2012.

[113] Thomas F. Miller and David E. Manolopoulos. Quantum diffusion in liquid water from ring polymer molecular dynamics. *The Journal of Chemical Physics*, 123(15):154504, 2005.

[114] Joseph A. Morrone and Roberto Car. Nuclear Quantum Effects in Water. *Phys. Rev. Lett.*, 101:017801, Jul 2008.

[115] Xin-Zheng Li, Brent Walker, and Angelos Michaelides. Quantum nature of the hydrogen bond. *Proceedings of the National Academy of Sciences*, 108(16):6369–6373, 2011.

[116] Thomas E. Markland and B. J. Berne. Unraveling quantum mechanical effects in water using isotopic fractionation. *Proceedings of the National Academy of Sciences*, 109(21):7988 – 7991, 2012.

[117] Mariana Rossi, Hanchao Liu, Francesco Paesani, Joel Bowman, and Michele Ceriotti. Communication: On the consistency of approximate quantum dynamics simulation methods for vibrational spectra in the condensed phase. *The Journal of Chemical Physics*, 141(18), 2014.

[118] Alexander Witt, Sergei D. Ivanov, Motoyuki Shiga, Harald Forbert, and Dominik Marx. On the applicability of centroid and ring polymer path integral molecular dynamics for vibrational spectroscopy. *The Journal of Chemical Physics*, 130(19), 2009.

[119] Francesco Paesani and Gregory A. Voth. A quantitative assessment of the accuracy of centroid molecular dynamics for the calculation of the infrared spectrum of liquid water. *The Journal of Chemical Physics*, 132(1), 2010.

[120] Francesco Paesani. Temperature-Dependent Infrared Spectroscopy of Water from a First-Principles Approach. *The Journal of Physical Chemistry A*, 115(25):6861–6871, 2011.

[121] Scott Habershon, George S. Fanourgakis, and David E. Manolopoulos. Comparison of path integral molecular dynamics methods for the infrared absorption spectrum of liquid water. *The Journal of Chemical Physics*, 129(7), 2008.

[122] Daniel J. Arismendi-Arrieta, Marc Riera, Pushp Bajaj, Rita Prosmiti, and Francesco Paesani. i-TTM Model for Ab Initio-Based Ion-Water Interaction Potentials. 1. Halide-Water Potential Energy Functions. *The Journal of Physical Chemistry B*, 120(8):1822–1832, 2016.

[123] Gregory R. Medders and Francesco Paesani. Infrared and Raman Spectroscopy of Liquid Water through "First-Principles" Many-Body Molecular Dynamics. *Journal of Chemical Theory and Computation*, 11(3):1145–1154, 2015.

[124] Andreas Goetz and Francesco Paesani. Private communication.

[125] Robert H. Swendsen and Jian-Sheng Wang. Replica Monte Carlo Simulation of Spin-Glasses. *Physical Review Letters*, 57(21):2607–2609, 1986.

[126] Charles J. Geyer. Markov Chain Monte Carlo Maximum Likelihood. *Computing Science and Statistics, Proceedings of the 23rd Symposium on the Interface*, pages 156–163, 1991.

[127] Koji Hukushima and Koji Nemoto. Exchange Monte Carlo Method and Application to Spin Glass Simulations. *Journal of the Physical Society of Japan*, 65(6):1604–1608, 1996.

[128] Eric G. Diken, William H. Robertson, and Mark A. Johnson. The Vibrational Spectrum of the Neutral $(H_2O)_6$ Precursor to the "Magic" $(H_2O)_6^-$ Cluster Anion by Argon-Mediated, Population-Modulated Electron Attachment Spectroscopy. *The Journal of Physical Chemistry A*, 108(1):64–68, 2004.

[129] Scott Habershon. Zero-point energy effects in anion solvation shells. *Phys. Chem. Chem. Phys.*, 16:9154–9160, 2014.

[130] Jake L. Stinson, Shawn M. Kathmann, and Ian J. Ford. Investigating the significance of zero-point motion in small molecular clusters of sulphuric acid and water. *The Journal of Chemical Physics*, 140(2):024306, 2014.